2024

Emergence of Preferential Flow Paths and Intermittent Dynamics in Emulsion Transport in Porous Media

Michael Izaguirre
mi6737@rit.edu

Emergence of Preferential Flow Paths and Intermittent Dynamics in Emulsion Transport in Porous Media

by

Michael Izaguirre

A dissertation submitted in partial fulfillment of the
requirements for the degree of
Doctor of Philosophy
in Imaging Science

Chester F. Carlson Center for Imaging Science
College of Science

Rochester Institute of Technology
Rochester, New York

Emergence of Preferential Flow Paths and Intermittent Dynamics in Emulsion Transport in Porous Media

by

Michael Izaguirre

Committee Approval:
We, the undersigned committee members, certify that we have advised and/or supervised the candidate on the work described in this dissertation. We further certify that we have reviewed the dissertation manuscript and approve it in partial fulfillment of the requirements of the degree of Doctor of Philosophy in Imaging Science.

Shima Parsa Dissertation Advisor/Committee Member	Date
Jairo Diaz Dissertation Committee Member	Date
Joseph Hornak Dissertation Committee Member	Date
Vinay Abhyankar Dissertation Defense Chairperson	Date

Certified by:

Jan van Aardt Ph.D. Program Director, Imaging Science	Date

Emergence of Preferential Flow Paths and Intermittent Dynamics in Emulsion Transport in Porous Media

by

Michael Izaguirre

Submitted to the
Chester F. Carlson Center for Imaging Science Ph.D. Program in Imaging Science
in partial fulfillment of the requirements for the
Doctor of Philosophy Degree
at the Rochester Institute of Technology

Abstract

This dissertation aims to study the underlying physics of anomalous transport of emulsions in porous media and quantify the role of droplet-pore and droplet-droplet interactions in transport in porous media experimentally. The complexities of this problem arise from the network heterogeneity, correlations between the pores across the medium, interfacial properties of the fluids, and the correlations between the pore scale dynamics and system-level transport.

This dissertation presents significant advancements in the study of emulsion dynamics within two-dimensional porous media through the development of innovative image analysis and tracking methods. These advancements include precise detection and tracking of deformable objects, which is particularly challenging in experiments involving large datasets with thousands of objects and millions of positional updates.

Utilizing cutting-edge microfluidic techniques, we developed an integrated experimental setup combining an on-demand drop maker and advanced imaging methods. By precisely controlling emulsion size, concentration, and injection rates, we uncovered critical insights into pore-level dynamics and bulk transport properties.

Through the application of variational mode decomposition (VMD), we effectively distinguished between uniform and irregular droplet formations, enhancing the accuracy of our measurements. Our findings demonstrate that emulsions predominantly flow through higher velocity pores, often becoming trapped in smaller pores, which reduces porosity and creates preferential pathways. Introducing slight polydispersity in emulsion sizes further improved transport efficiency by revealing additional pathways.

We also explored the effects of device scaling, dye contrast adjustments, and interfacial tension

on emulsion behavior, leading to refined detection and tracking algorithms. These advancements provide a robust framework for future studies and have significant implications for applications in soil remediation, drug delivery, and enhanced oil recovery.

Additionally, the creation of high-quality datasets from our experiments lays the groundwork for leveraging machine learning techniques to further understand and predict the complex nature of emulsion transport in porous media. This interdisciplinary approach offers the potential to bridge experimental observations and theoretical models, enhancing our ability to manage and optimize fluid dynamics in various applications.

This research represents a substantial contribution to the field of microfluidics and multiphase flow, offering new methodologies and insights that will propel future innovations and applications.

The results of this research provide the necessary research platform to advance the research on transport of deformable particles in porous media. In addition to the research questions, these understandings will impact industrial processes such as filtration in food industry, sorting in pharmaceutical, drug delivery in medical, enhanced oil recovery, and soil remediation in environmental industries.

Acknowledgments

First and foremost, I would like to express my deepest gratitude to my advisor, Dr. Shima Parsa, for being a supportive and excellent advisor and mentor. Her invaluable guidance and support at every stage of this research project have been instrumental to its completion. Dr. Parsa's commitment to excellence and her encouragement have greatly inspired me throughout this journey.

I am also profoundly grateful to my committee members: Dr. Joseph Hornak, Dr. Jairo A. Diaz, and Dr. Vinay Abhyankar. Their insightful comments and suggestions have been crucial in refining this work and pushing the boundaries of my research.

I extend my thanks to the funding sources that made this research possible. I am grateful for the financial support provided by the National Science Foundation under grant CBET-2301243, and the donors of the ACS Petroleum Research Fund Grant PRF 62556-DNI9.

Additionally, I would like to acknowledge the support and companionship of my lab mates. Your eagerness to explore and discover, along with the ideas exchanged during our lab meetings, has been both motivating and enriching for my own work.

Lastly, I would like to extend my heartfelt thanks to my friends and family for their unwavering support and love throughout this journey. Your encouragement and understanding have been invaluable, providing me with the strength and determination to persevere.

Thank you all for contributing to this significant milestone in my life.

To my parents, whose sacrifices and hard work have laid the foundation for my educational journey. Your support and love have granted me the opportunity to pursue my dreams and build a brighter future. Without your sacrifices, I would not be the person I am today. To my siblings, whose constant support and encouragement have motives us to pursue our dreams. I know we will always stand by each other, no matter the distance and continue to provide the love and support to one another that has brought us here. To my grandparents, who faced countless challenges and made immense sacrifices so their descendants could prosper. This degree is a testament to your enduring legacy, and I am deeply grateful for your support. To my close friends, who have expanded my horizons and enriched my life with diverse perspectives.

A mis abuelos, quienes enfrentaron innumerables desafíos y realizaron inmensos sacrificios para que sus descendientes pudieran prosperar. Este título es un testimonio de su legado perdurable, y estoy profundamente agradecido por su apoyo constante. Su amor y esfuerzo han sido la base de todas mis oportunidades, y siempre llevaré sus recuerdos en mi corazón.

Quiero dedicar y conmemorar este logro a los seres queridos que he perdido durante este tiempo: a mi abuelo Tomás Izaguirre y a mi tío Antonio Rodríguez. Su historia y legado vivirán e inspirarán a las generaciones futuras mientras compartimos sus recuerdos, amor y sacrificios. Que Dios los tenga en su gloria y que sus espíritus continúen guiándonos y bendiciéndonos. Sus vidas y recuerdos han sido una luz en nuestras vidas, y seguirán siendo una fuente de inspiración y fortaleza para nuestra familia.

Contents

List of Figures

List of Tables

Chapter 1

Introduction

Understanding the behavior of emulsions within porous media is critical for advancing applications in fields such as material science, environmental engineering, and biomedical technology. This research investigates microscale fluid dynamics through a combination of rigorous experimental studies, advanced computational analyses, and innovative technical explorations. The initial focus is on microfluidic droplet generation, utilizing precise control mechanisms to elucidate droplet behaviors within engineered systems. This foundational study not only establishes benchmarks for experimental precision but also sets the stage for exploring more complex fluid interactions.

The next phase explores the transport phenomena of emulsions within porous structures, emphasizing the characterization of flow anomalies and the emergence of preferential flow paths. These intermittent dynamics challenge existing models, necessitating a more refined experimental and theoretical approach. By integrating experimental data with simulation outcomes, this work constructs a comprehensive framework to describe the complex behaviors of fluids in porous environments.

The overarching goal of this dissertation is to bridge the control achieved in microfluidic systems with the macroscopic fluid behavior in porous media, providing a thorough understanding of the underlying physical processes. This research is pertinent to material science and engineering disciplines, enhancing the understanding of soft matter physics and refining methodologies for studying fluid dynamics in porous systems. By combining empirical research with detailed analysis, this work offers insights that extend to broader scientific and engineering fields.

Fluid dynamics within porous media is crucial across various scientific and engineering disciplines, necessitating a multifaceted approach that combines experimental investigations with theoretical

modeling. Traditional bulk analysis provides a macroscopic view of flow behavior through aggregate statistics. However, this dissertation emphasizes the dynamics at the microscale using microfluidic systems, which allow for precise manipulation and observation of fluid interactions. This focus is critical for understanding the fundamental mechanisms of multiphase flow, common in both natural and engineered porous media.

The intermittent nature of these flows presents significant challenges to conventional models, which often fail to capture the stochastic behaviors of emulsions moving through heterogeneous pathways. To address these complexities, this research integrates state-of-the-art experimental methods with advanced computational modeling, employing sophisticated tracking and detection methods. These methods enhance the accuracy of predictive models and offer granular insights that bulk analysis typically overlooks. This synergy between empirical research and theoretical analysis lays the groundwork for a comprehensive exploration of porous media dynamics, underscoring the pivotal role of microfluidic technologies in bridging microscale phenomena and macroscopic applications.

Advanced image processing methods can significantly improve imaging outcomes. Enhanced image contrast and modern tracking algorithms make it feasible to discern and characterize individual emulsion behaviors at the pore level, providing deeper insights into their dynamics. The field of microfluidic device fabrication is also making significant strides. Rapid prototyping, particularly through high-resolution 3D printing, can circumvent the traditional reliance on time-consuming lithography methods. Ensuring compatibility of 3D printing materials with PDMS, the prevalent polymer in microfluidics, allows for rapid production of new designs.

The challenge of consistently forming uniform droplets can be addressed through an informed design approach. Understanding the physics of droplet formation, such as the LaPlace snap-off phenomenon, can inform the generation of uniform droplets from circular nozzles. Rectangular channels, a limitation of 3D printing, can be optimized to leverage this physical behavior. Proper channel coating and a pressure pulse device can facilitate the desired flow for consistent droplet formation.

This study also employs computational simulations to design a precise and controllable droplet generator, essential for initiating consistent microscale experiments focused on individual droplet behaviors. Micromodels simulate real-world porous structures, facilitating direct observation of phenomena such as droplet behavior and phase transitions within engineered porous matrices. Advanced manufacturing techniques, such as 3D printing, create accurate micromodels of porous structures, enabling detailed observations of droplet behaviors and flow characteristics.

Characterizing transport phenomena within porous structures further explores how multiphase fluids navigate these environments, focusing on the identification and exploitation of preferential paths. This aspect is crucial for understanding the stochastic nature of fluid distribution and movement, influenced by pore size variability and distribution. By coupling advanced tracking and detection techniques, this research not only predicts flow behaviors more accurately but also informs the design and optimization of processes involving fluid dynamics in porous media. This approach significantly advances both scientific inquiry and practical applications, offering insights into individual fluid dynamics that extend beyond the capabilities of traditional bulk analysis.

In summary, while the challenges of studying emulsion dynamics in porous media are multifaceted, the integration of advanced imaging, rapid prototyping, and informed design approaches holds promise in addressing these issues, paving the way for more accurate and insightful experiments. This dissertation aims to enhance our understanding of emulsion transport through porous media, with implications for various applications such as oil recovery, groundwater remediation, and drug delivery systems. By bridging the gap between microscale control and macroscopic fluid behavior, this research contributes to the broader field of fluid dynamics and porous media, offering refined methodologies and comprehensive insights that can be applied across multiple disciplines.

1.1 Research Problem

Multi-phase flows through porous materials play a crucial role in various applications, presenting distinct challenges rooted in fundamental physics. While fluid dynamics at scales larger than individual pores are relatively well-understood through mean field approximation, this methodology often falls short in capturing the intricate dynamics of multi-phase flows, particularly emulsions. The behavior of emulsions within porous media reveals inherent complexities, such as non-linear dynamics, challenging imaging conditions, and the proximity of deformable objects. These factors complicate tasks such as image segmentation, object detection, and tracking. This complexity underscores the need for advanced imaging methods and cutting-edge microfluidic techniques to enhance our understanding of emulsion transport through porous media.

Characterizing emulsion dynamics within porous structures presents several significant challenges, primarily in imaging and droplet generation. High-resolution, high-contrast, and rapid image acquisition are necessary to accurately capture emulsion droplets' behavior. However, the intrinsic properties of porous materials, such as light scattering and similar refractive indices between the droplets, continuous fluid, and the porous medium, often result in poor-quality images. Current

imaging techniques, including confocal microscopy, struggle to provide the clarity and refresh rates required for precise analysis.

Advanced imaging methods, such as X-ray tomography and magnetic resonance imaging (MRI), have the potential to address these limitations but require further development for this specific application. X-ray tomography offers detailed structural insights but often lacks sufficient temporal resolution for dynamic studies. Similarly, MRI, particularly echo planar imaging (EPI), can achieve echo spacings as short as 1.2 ms [86], allowing for rapid imaging with sub-millimeter resolution. However, π EPI's application in porous media is complex due to the need for compensating magnetic field distortions and precise gradient control, making it more challenging than optical imaging methods. Despite these challenges, PEPI can generate high-quality, proton density-weighted images, useful in fluid saturation studies in rock core plugs.

In pioneering work, Seymour and Callaghan [70] introduced pulsed-gradient spin echo (PGSE) NMR methods to study flow and diffusion in porous media. This approach allows probing fluid dynamics over well-defined temporal and spatial domains. PGSE NMR techniques, like flow imaging and velocity exchange spectroscopy, provide insights into the dispersion coefficient, mean local velocity, and spatial-temporal correlations. These techniques have been applied to study flow and dispersion of water in porous media, demonstrating the interplay between hydrodynamic and structural characteristics.

Further advancements have been made with dynamic NMR relaxometry, as demonstrated by Maillet et al. [**?**], offering a novel approach for characterizing liquid transfers and surface evolution in porous media. This technique analyzes proton spin relaxation to provide quantitative insights into liquid distribution and its temporal changes within porous structures. Unlike conventional imaging, NMR relaxometry identifies liquid interactions with various pore sizes, offering insights into the internal dynamics and specific surface area interactions within the media. It has been applied to materials such as nanoporous silica, polymers, and cement, providing valuable data on fluid saturation, drying, and phase transitions. This method is noninvasive and cost-effective, but it requires careful data interpretation due to noise and resolution constraints.

Pak et al. [56] used X-ray computed microtomography to visualize complex pore-scale processes during multiphase flow in carbonate rocks. Their research revealed the intricate dynamics of fluid behavior at the pore level, emphasizing that even seemingly small-scale processes can significantly impact overall fluid displacement efficiency. The study highlights the complexity of multiphase flow in heterogeneous porous media, illustrating how minor variations in pore geometry and fluid properties can lead to diverse flow patterns and behaviors.

Parsa et al. [58] explored the complex dynamics of immiscible fluid displacement in porous media with large viscosity mismatches using confocal microscopy. Their study revealed that polymer retention leads to heterogeneous local flow changes, enhancing displacement even with significant viscosity differences. The findings contradict traditional beliefs that improved displacement results solely from increased viscosity suppressing viscous fingering. Instead, Parsa et al. found that polymer flow induced local velocity fluctuations, which enhanced oil recovery, providing new insights into pore-level fluid dynamics and challenging existing theories of polymer-enhanced oil recovery.

These advancements underscore the ongoing need for research and development in imaging and tracking technologies to thoroughly understand and characterize emulsion dynamics within porous structures. Despite significant progress, current methods still face limitations, such as inadequate spatial resolution, restricted macroscopic views, and slow temporal resolution, which highlight the necessity of exploring alternative techniques. Emerging technologies like advanced microfluidics offer precise and controlled observations at the pore level, proving to be powerful tools in overcoming these challenges. These innovations promise to provide deeper insights into the complex behaviors within porous media and drive further advancements in the field.

Uniform droplet generation poses another major challenge. Ensuring that droplets remain uniform throughout the experiment is difficult due to interactions such as coalescence, divergence, and unpredictable behavior when droplets are in close proximity. Factors such as interfacial tension, fluid properties, and flow dynamics contribute to these interactions, resulting in nonuniform droplet formation that creates additional complexities in analysis. The added complexity of generating droplets on demand, rather than continuously, requires precise control over droplet size and frequency.

Microvalve systems, such as the one developed by Churski et al. [17], utilize a computer-controlled microvalve integrated into a stiff polymeric microfluidic device. This method allows for the formation of droplets and bubbles of arbitrary volumes and at arbitrary times of emission. However, the complex, multilevel fabrication process and the requirement for external control equipment pose significant drawbacks to its widespread application.

Negative-pressure controlled systems, like those introduced by Teo et al. [78], rely on toggling fluid states using periodic negative pressure pulses to induce droplet generation. This method can produce droplets on demand with volumes proportional to the pulse width. Despite its effectiveness, it demands high synchronization and precision in toggling fluid states, which can be challenging to maintain consistently especially when integrating additional features in the microfluidic device.

Off-chip controlled systems, as presented by Hamidović et al. [30], utilize externally pre-programmed positive pressure pulses applied to the dispersed phase input while maintaining constant pressure in the continuous phase channel. This method allows for high reproducibility and simplicity in chip design, facilitating rapid and cost-efficient prototyping. However, it faces precision issues at extreme pressures and depends heavily on the response systems of controllers, which can affect reproducibility.

In summary, the challenges of uniform droplet generation in microfluidic systems are multifaceted, involving intricate interactions between various physical properties and control mechanisms. Continued advancements in microvalve systems, negative-pressure controlled systems, off-chip controlled systems, and emerging technologies are essential to overcoming these challenges and achieving consistent and reproducible droplet formation.

Microfluidic device fabrication introduces its own set of complications. Maintaining consistent microfluidic channels across devices is crucial, yet reproducing intricate real-world pore structures at microscopic scales remains an ongoing challenge. Techniques such as soft lithography and photolithography enable precise replication of microfluidic devices, but achieving rapid prototyping in these devices is difficult and time consuming. Additionally, the material properties of the mold and polydimethylsiloxane (PDMS), such as surface energy and chemical compatibility, need to be carefully controlled to prevent unwanted interactions that could affect result in failed microfluidic devices. Controlling and maintaining stable experimental conditions is integral but difficult, especially when attempting to replicate real-world scenarios. Variations in these conditions such as flow rate and pressure can alter emulsion stability, droplet size, and flow dynamics.

In essence, while studying emulsion dynamics in porous media holds great promise, it is fraught with multifaceted challenges ranging from imaging and droplet consistency to device fabrication and the control of experimental conditions. This research aims to address these challenges by integrating advanced microfluidic technologies and sophisticated imaging techniques. By experimentally discerning the elusive behavior of emulsions in porous structures and ensuring comprehensive characterization throughout the experimental phases, we aim to enhance our understanding of emulsion transport through porous media. This knowledge is crucial for applications in industries such as oil recovery, groundwater remediation, and drug delivery systems, where improved emulsion dynamics can lead to significant advancements and efficiencies.

1.2 Research Questions and Hypotheses

1.2.1 Research Questions

The big picture question is to study the underlying physics of anomalous transport of emulsions in porous media and quantify the role of droplet-pore and droplet-droplet interactions in transport in porous media experimentally. The complexities of this problem arise from the network heterogeneity, correlations between the pores across the medium, interfacial properties of the fluids, and the issues correlating pore scale dynamics and system-level transport. To address this challenging research objective, we address the following questions:

1. How can advanced image processing methods, including fluorescent imaging, modern optical microscopy, high-resolution cameras and modern tracking algorithms, be optimized to improve the characterization of emulsion behaviors at the pore level in porous media?
2. What are the effects of using high-resolution 3D printing techniques on the precision and reproducibility of microfluidic device fabrication, particularly in creating structures compatible with PDMS?
3. How can the understanding of the LaPlace snap-off phenomenon and other droplet formation physics inform the design of microfluidic channels to consistently generate uniform droplets?
4. What are the impacts of various channel coatings and pressure pulse devices on the consistency and stability of droplet formation in microfluidic experiments?
5. How do variations in interfacial tension and pressure within the microfluidic setup affect the stability and dynamics of emulsions, and how can these variations be effectively controlled?
6. How do surface tension and the physical properties of emulsions affect the ability to track, detect, and characterize emulsion transport behavior?

1.2.2 Hypotheses

1. Advanced image processing methods, when integrated with fluorescent microscopy, significantly enhance image contrast and accuracy in object detection and tracking, leading to more precise characterization of emulsion behaviors at the pore level.

2. High-resolution 3D printing can produce microfluidic devices with greater precision, speed, and reproducibility than traditional lithography, particularly when using materials compatible with PDMS.

3. By leveraging the LaPlace snap-off phenomenon and other droplet formation principles, microfluidic channels can be designed to consistently produce uniform droplets, even in rectangular channels typical of 3D printed devices.

4. Appropriate channel coatings and the use of pressure pulse devices improve the consistency and stability of droplet formation in microfluidic experiments.

5. Controlled environmental conditions within the microfluidic setup can stabilize emulsion dynamics, leading to more reliable experimental results.

6. Deformation of droplets lead to more difficult instances of detection requiring advanced detection methods.

1.3 Research Objectives

The overarching goal of this research is to quantify the pore-level dynamics of low concentration emulsions in porous media and determine the role of pore-droplet interactions in transport across the medium. I stride to enhance the understanding and characterization of emulsion dynamics within porous media through the integration of advanced imaging techniques, innovative microfluidic device fabrication, and informed design approaches. Specifically, the research aims to:

1. Develop and optimize advanced image processing methods, incorporating fluorescent imaging, dyes and modern tracking algorithms, to improve the resolution, contrast, and accuracy of characterization of emulsion behaviors at the pore level.

2. Utilize high-resolution 3D printing to fabricate precise and reproducible microfluidic devices, ensuring material compatibility with PDMS and validating the performance of these devices in experimental setups.

3. Investigate the physics of droplet formation, such as the LaPlace snap-off phenomenon, to inform the design of microfluidic channels that can consistently generate uniform droplets. Explore the optimization of rectangular channels typical of 3D printed devices to enhance droplet formation consistency.

4. Test and implement various channel coatings and pressure pulse parameters to improve the consistency and stability of droplet formation in microfluidic experiments, evaluating their effectiveness under different experimental conditions.

5. Examine the effects of pressure and pore network variations on emulsion stability and dynamics within the microfluidic device. Develop and implement control mechanisms to maintain stable experimental conditions, ensuring reliable and reproducible results.

6. Apply the insights gained from improved emulsion characterization to practical applications, such as oil recovery, groundwater remediation, and drug delivery systems, demonstrating the broader impact of this research on industry and technology.

By addressing these objectives, this research seeks to overcome the current limitations in studying emulsion dynamics in porous media, paving the way for more accurate and insightful experiments and contributing to advancements in various applications that rely on multi-phase flow through porous materials.

Chapter 2

Applications and Challenges

2.1 Emulsion Transport

Transport of emulsions in porous media is of significant interest in industrial, medical, and environmental applications, including food products, drug delivery, and immiscible displacement [6, 39, 44, 45, 60, 67]. The heterogeneity of natural and synthetic porous materials leads to diverse flow patterns, significantly impacting droplet transport [1]. Transport properties can undergo dynamic alterations due to flow and retention of materials inside the pores [21, 58, 59]. Biofilm growth in filters [39, 53], transport of water-based emulsions in personal care products [4, 9], and oil recovery [44, 46, 58, 59] exemplify how medium properties change in response to droplet flow. Although bulk transport properties such as medium permeability may exhibit minor changes, local and pore-scale flows can dramatically shift, leading to anomalous behavior [14, 58, 59, 88].

The dynamics of a single emulsion droplet in porous media are governed by droplet size and network properties such as pore size distribution and medium wettability [14,29,60,67,87]. Viscous, interfacial, and drag forces balance to describe these dynamics. The Capillary and Weber numbers, representing the ratio of viscous to interfacial forces and drag to interfacial forces, respectively, are used for droplets with minimal deformations [7, 11, 50, 60, 74]. However, the collective dynamics of emulsions in a complex pore network are influenced by local flow fluctuations due to droplet-droplet and droplet-pore interactions [29]. High-concentration emulsion transport in media with random pinning sites shows a transition from creeping flow to flow along smectic rivers and groups [40]. Experiments indicate negligible droplet deformation, with the majority of droplets never squeezing through small pores, primarily pinning on surfaces. Bulk transport measurements of polydisperse

droplets stabilized by surfactants injected into a three-dimensional porous medium reveal that small droplets appear in the effluent, while large droplets remain trapped due to high deformation pressure requirements [14, 29, 87, 92]. Pore-level and collective droplet dynamics, and the impact of trapping and re-mobilization on transport properties, require further examination. Accurate experimental investigations necessitate advanced tracking and object detection techniques, particularly when droplets are in proximity and deform based on pore sizes.

In this study, we quantify pore-level dynamics of monodisperse emulsions in a two-dimensional porous medium using microfluidics. By integrating a microfluidics drop-maker on the same chip, we precisely control the concentration and size of injected emulsions. Individual droplets are tracked using optical microscopy and long-range recording while monitoring the bulk pressure gradient. Advanced image analysis and object tracking are employed to monitor droplet flow through the medium. At low concentrations, emulsions flow through pores with higher local velocities without size selectivity, leading to potential trapping. As more pores fill with droplets, newly injected emulsions flow through remaining open paths. The average velocity of droplets correlates inversely with their residence time and is proportional to path lengths, independent of emulsion size distribution. Understanding the dynamics of emulsions in porous media is pivotal for advancements across various sectors. In enhanced oil recovery and environmental remediation, the behavior of emulsions in porous structures provides essential insights for developing more efficient methodologies. The food and pharmaceutical sectors also benefit, as emulsions serve as stabilizers and carriers. Furthermore, in material sciences, these dynamics are crucial for fabricating materials with tunable properties, such as ceramics, composites, and catalysts [39, 44, 45, 60, 67].

These advancements can revolutionize industries by reducing costs and increasing productivity. The ability to rapidly image, fabricate, and replicate experimental setups enables the accumulation of extensive datasets. Properly interpreted, these data can reveal theories and models that elucidate the intricate behavior of emulsions in porous media.

The heterogeneous nature of most natural and synthetic porous materials leads to diverse flow patterns, which critically influence the transport of emulsion droplets [1]. Dynamic changes in transport properties can result from biofilm growth in filters [39, 53], water-based emulsion transportation in personal care products, and the use of emulsions in enhanced oil recovery [4, 9, 44, 46]. While bulk transport properties might exhibit minor shifts, pore-scale flow can experience significant changes, leading to anomalous flow behaviors [58, 59].

The dynamics of individual emulsion droplets in porous media can be explained through the balance of various forces, primarily viscous, interfacial, and drag forces. Two non-dimensional parameters,

the Capillary and Weber numbers, describe these dynamics for droplets exhibiting minimal deformations [7, 11, 50, 60, 74]. However, when considering multiple emulsions within complex pore networks, their behavior is influenced by local flows resulting from interactions between droplets and between droplets and the pore structure [29].

The complexity of emulsion dynamics within porous media poses significant experimental challenges. Prior experiments indicated minimal droplet deformation, suggesting droplets did not navigate smaller pores. Measurements of bulk transport, particularly with polydisperse droplets stabilized by surfactants in a three-dimensional porous medium, showed that smaller droplets passed through the medium, while larger droplets were primarily retained within it. This retention is attributed to the substantial pressure required to deform these larger emulsion droplets [14,29,87,92]. Experimentally probing these dynamics is particularly challenging when droplets are in proximity and alter their shape based on pore dimensions, highlighting the need for advanced tracking and precise object detection.

Several factors influence emulsion transport in porous media, including droplet properties, porous medium characteristics, and flow conditions. As droplets traverse the porous medium, their size and shape may alter, affecting emulsion viscosity and, consequently, flow resistance. These intricacies underscore the need for a deeper understanding of emulsion behavior in porous landscapes, which is crucial for practical applications like designing efficient oil recovery processes and innovating contamination remediation techniques.

Predicting emulsion stability in porous media, given the variable conditions such as pressure, temperature, and flow, is challenging. In real-world scenarios, regulating these variables is difficult, making an understanding of force interplays essential.

In summary, while the dynamics of emulsions within porous media are complex and challenging to study, advancements in experimental and computational techniques promise to unlock significant potential across various applications. By integrating sophisticated imaging, rapid prototyping, and informed design approaches, researchers can develop more accurate models and innovative solutions for real-world challenges in fluid dynamics and material science.

2.2 Droplet Microfluidics

Droplet microfluidics is a powerful technique enabling the precise control of droplet size, cargo loading, sorting, and merging at volumes as small as picolitres. These capabilities have led to

its extensive use across industries such as pharmaceuticals, material production, and research and development [15, 65, 72]. Moreover, droplet microfluidics shows promise in signal processing [31, 76]. Droplet sizes are determined by the interfacial tension between fluids, the geometry of the microfluidics chip, and fluid phase flow rates [75, 80]. Optimally operated microfluidic chips are stable and reliable for producing monodisperse droplets [23, 49, 52, 61, 63]. However, small errors, such as satellite droplets or unexpected mergers, may still occur due to instabilities in external units or local flow [16, 90]. Generally, these errors are monitored visually and sorted out using methods like deflecting fluids with external forces or filtering droplets by size [12, 31, 54]. Given the high-speed operation of microfluidic chips, it is crucial to detect and correct errors at comparable speeds. Flow fluctuations driven by high flow rates can grow quickly and disrupt downstream flow due to the nonlinear nature of fluid flows. Although not all fluctuations are significant, identifying them theoretically or in real time is challenging. Nevertheless, flow velocities and pressure fluctuations in a device are accessible in real time [1, 13].

Standard signal processing methods, such as Fourier transform and wavelet analysis, can quantify or predict anomalies in microfluidics, though they are less efficient in nonlinear and non-stationary systems and can be computationally intense. Dynamic mode decomposition, developed from continuous flow snapshots, closely describes flow motion even in turbulent regimes [68]. The empirical mode decomposition (EMD) method, developed to better analyze nonlinear and non-stationary signals, aims to separate events using instantaneous frequency [33, 43, 85]. EMD has been applied in various fields, including identifying dominant frequencies in atmospheric data [38], separating unsteady spatiotemporal scales in wind tunnel data [2], analyzing turbulent velocity fields in unsteady flows [66], and extracting health-related hemodynamics features [84]. A successful use of EMD is identifying physically significant modes or frequencies in noisy signals, as seen in characterizing turbulence from grid-generated flows [27]. Variational mode decomposition (VMD), a method based on EMD, has lower noise sensitivity and extracts modes concurrently, identifying central frequencies and oscillatory modes [25]. VMD has been applied in various fluid mechanics and hydrodynamics areas, showing promise in isolating physical signals and providing predictive metrics for improved performances [24, 26, 37, 69].

2.3 Concluding Remarks

While the study of emulsion dynamics in porous media is complex and challenging, advances in experimental and computational techniques offer significant potential across diverse applications. By integrating sophisticated imaging, rapid prototyping, and informed design approaches, researchers

can develop more accurate models and innovative solutions for real-world challenges in fluid dynamics and material science.

Chapter 3

Uniform Droplet Formation in Microfluidics

The exploration of microfluidic droplet generation in this work underscores the meticulous design and analytical precision required to enhance our understanding of fluid dynamics within microscale systems. Through the application of variational mode decomposition, this research offers a detailed analysis of velocity signals from drop-makers, revealing how subtle design variations can significantly impact droplet uniformity and stability. Particularly, by adjusting the length of the water inlet in the microfluidic devices, we observe a direct influence on droplet formation in flow driven droplet makers. This design sensitivity highlights the critical role of engineering precision in optimizing droplet uniformity, a key factor for applications ranging from pharmaceuticals to material science. The analytical technique employed here—breaking down the velocity signal into five intrinsic modes—allows for a clear distinction between oscillatory and stable flow components, demonstrating how even minor fluctuations can be pivotal. The findings are particularly notable in the detection of the fifth intrinsic mode's behavior, which serves as a reliable indicator of droplet uniformity. The presence of a stable fifth mode correlates strongly with the production of uniform, mono-disperse droplets, whereas deviations in this mode signal potential inconsistencies. This mode's sensitivity to upstream conditions—far before the droplets are formed—provides invaluable foresight, enabling preemptive adjustments to the process. This study not only deepens our understanding of the intricacies of microfluidic droplet dynamics but also enhances the methodological framework for future research in this field. By demonstrating the effective use of sophisticated signal analysis techniques, it offers a model for how detailed experimental data can be leveraged to improve the design and functionality of microfluidic systems, ensuring more reliable and pre-

dictable outcomes in various scientific and industrial applications. This chapter has been adapted from Izaguirre's 2022 paper. [35]

3.1 Introduction

Droplet microfluidics is a powerful technique enabling the precise control of the size of the droplets, loading of cargo, sorting, and merging droplets at small volumes of the order of picolitres. These capabilities have led to the extensive use of droplet microfluidics in a wide range of applications in industries such as in pharmaceutical, material production, and in research and development [15,65, 72]. Moreover, droplet microfluidics is a promising tool in signal processing. [31, 76]. The sizes of the droplets are determined by the interfacial tension between the two fluids, the geometry of the microfluidics chip, and the flow rates of each fluid phase [75, 80]. Microfluidics chips operated in their optimum regime prove to be stable and reliable for the production of monodisperse droplets [23, 49, 52, 61, 63]. On-chip processes can be optimized to minimize errors in performance since a microfluidic chip interacts with a few external control units, pumps, and valves [47]. However, small errors, such as satellite droplets, missed mergers, or unexpected merging of droplets may still occur due to instabilities in external units or in local flow [16, 90]. In general, these errors are monitored visually and anomalies can be sorted out with different methods, either by deflecting some fluids to a separate channel using external electric or acoustic forces or by passing the droplets through filters to sort by size [12,31,54]. Since most microfluidics chips run at high speeds, 100 s of μL/hr, it is crucial to detect and correct errors at comparable speeds [16]. Flow fluctuations in a microfluidic channel driven at a high flow rate can grow quickly and disrupt the flow downstream due to the nonlinear nature of fluid flows. Although not all fluctuations are significant, it is not possible to identify them theoretically or in real time once a microfluidic device is running. Nevertheless, flow velocities and pressure fluctuations in a device are accessible in real time [1, 13].

In principle, standard methods of signal processing can be implemented to quantify or predict anomalies in microfluidics, although they are not commonly used. Fourier transform and wavelet analysis perform well in simplifying complex and noisy time series. However, this powerful signal analysis method is less efficient in nonlinear and non-stationary systems such as fluid flows and can be computationally intense. Moreover, dynamic mode decomposition is developed based on continuous snapshots of flow and is shown to closely describe the motion of the flow even in the turbulence regime [68]. In recent decades, the empirical mode decomposition (EMD) method has been developed to better analyze signals from nonlinear and non-stationary data sets [33, 43, 85]. EMD is data driven, a posteriori, and adaptive, which aims to separate events by utilizing the

notion of instantaneous frequency, in contrast with fundamental frequencies as in Fourier analysis. EMD has been used in a variety of applications, including identification of dominant frequencies in atmospheric data [38], separating unsteady spatiotemporal scales in the mixing layer in wind tunnel data [2], analyzing instantaneous turbulent velocity field in unsteady flows [66], and extracting health-related hemodynamics features [84]. One of the successful uses of EMD is to identify modes or frequencies with physical significance in a noisy signal, as in characterizing the properties of turbulence from stationary and non-stationary grid-generated flows [27]. For example, in a systematic study, a periodic perturbation was introduced to the flow, and EMD was used to separate the high-frequency part of the signal from the low-frequency parts, and the artificial perturbation was retrieved. Variational mode decomposition (VMD) has been developed based on EMD with a lower sensitivity to noise [25]. This method stepped away from recursive decomposition and extracts modes concurrently. It finds central frequencies and oscillatory modes within various basebands [25], and is even proven to extract central data from geophysical data where isolated spikes appear often [48, 73]. The applications of VMD in different areas of fluid mechanics and hydrodynamics has been extremely promising in isolating physical signals and providing predictive metrics for improved performances [24, 26, 37, 69].

In this paper, we use a novel method of signal decomposition, variational mode decomposition, to determine the formation of uniform droplets in a microfluidic drop-maker. We simulate the formation of water in oil droplets in a microfluidic device with two independent drop-makers. To compare the signal from different geometries, we choose the sizes of the water inlets of the drop-makers to be slightly different. We map the velocities calculated in the simulation onto a uniform grid to mimic the velocity field commonly measured in experiments using particle image velocimetry. Using variational mode decomposition, we decompose the velocities measured at the center of the channel to its intrinsic mode functions (IMF). For the velocity signal in our simulations, only five modes are sufficient to fully separate noise and high oscillations from the underlying average velocity. The first mode in the decomposition, IMF 1, usually has the highest oscillations and noises among all modes. The second to fourth modes have considerable oscillations with magnitudes similar to each other and similar to the first mode or at least within the same order of magnitude. However, the fifth mode, IMF 5, appears to only show the underlying average velocities at the center of the channel with values much larger than the other IMFs. We find that uniform droplets form when IMF 5 is a plateau with small variations around its local average. Interestingly, this signature plateau coincides with uniform droplet formation even when we use the velocities inside the water inlet and long before the fluid is broken into droplets. We show that variational mode decomposition is able to quantify anomalies in the signal that trigger fluctuations in flow and droplet sizes downstream.

3.2 Materials and Methods

3.2.1 Droplet Simulation

To study the flow fluctuations during droplet formation in a microfluidic T-junction with high spatial resolution, we use COMSOL multiphysics (3.2.10), a laminar two phase flow module, and the level set method [77]. The geometry of the microfluidic device consists of two T-junction dropmakers located on opposite sides of a long channel. Droplets are generated on two sides of this channel and meet in the middle of the device where they can either merge or bypass each other and exit through a single outlet as shown in Figure. The widths of the inlets channels are 50 μm. Droplets are formed when the inner fluid, water, in the middle inlet is sheared with the outer fluid, an oil which has an interfacial tension of $\gamma = 3$ mN/m with water [77], which flows in the two adjacent inlets as shown in Figure reffig1 (Supplementary Materials). Here, we choose to generate water in oil emulsion droplets. The density of the inner fluid, ρ, is 1 kg/L and the outer fluid is 1.6 kg/L and their respective viscosities are $\mu_{in} = 1$ mPas and $\mu_{out} = 1.2$ mPas. To keep the simulations stable and resolve the interfaces, COMSOL used an adaptive mesh with nonuniform grid sizes. The lengths of the channels on either side are 425 μm, measured from the beginning of the inlet. These lengths are optimized so the two-phase simulation is stable and the interfaces are resolved while the microfluidic device resembles physical experiments [15]. The inner fluid is flowed at 2 cm/s and the outer fluid at $u = 2$ cm/s. At these flow rates, a steady stream of droplets is expected to form in the dripping regime [80]. The imposed pressure at outlet is $P_{out} = 0$ Pa. The capillary number is 8.0×10^{-3}, ratio of capillary to viscous force ($Ca = \mu_{out} u/\gamma$). The corresponding Weber number, the ratio of drag to cohesion force, $We = \rho u^2 r/\gamma$ is 6.0×10^{-3}, where r is the radius of the channel. The Capillary and Weber numbers are within the dripping regime where the balance between the capillary forces at the interface of two fluids and the viscous force from the outer fluid determines the formation of a droplet [80]. Once a droplet is formed, it flows through the channel leading to the junction with the opposite dropmaker as shown in Figure 3.1 (Supplementary Materials). The left inlet channel is shortened to mimic a fabrication error while the right channel has an optimized geometry for the flow rates chosen. The left channel begins to form droplets a few milliseconds before the right channel as well as form satellite and non-uniform droplets sporadically. The numerical simulation in COMSOL uses an adaptive mesh to optimize the computational time. Consequently, the data are on a non-uniform grid with finer mesh sizes close to the interfaces. Using the natural neighbor algorithm, we interpolate this data on a uniform grid. The mesh size is 200 nm and the total area of the mesh is 850 $\times$ 215 μm^2.

3.2.2 Signal Decomposition

Variational mode decomposition extracts oscillatory modes of the signal and provides insight into how the flow evolves as a function of time at various positions. VMD is a modern algorithm based on some of the concepts of empirical mode decomposition which were first developed with nonlinear and non-stationary processes in mind to decompose a time-domain signal into intrinsic mode functions [33, 89]. These oscillatory modes, IMF, follow two primary criteria: (i) the number of extrema and number of zero crossings must either be equal or only differ by one; this criteria is equivalent to the narrow band requirement for a stationary Gaussian process. (ii) The mean value of the envelope defined by the local maxima and minima must be zero [34]. The second criterion creates a local time-dependent requirement which assists with decomposing nonlinear signals and allows IMFs to have both modulated amplitude and frequency with a finite bandwidth. However, boundaries and spikes in the original signal can lead to artifacts in the IMFs to satisfy the criteria mentioned above. To resolve such issues, various methods have been developed among which variational mode decomposition (VMD) has been successfully used to describe dynamics in fluid systems [73]. VMD stepped away from recursive decomposition and extracts modes concurrently. It searches through frequencies of the original signal to find central frequencies and oscillatory modes within various basebands [25]. VMD adaptively selects the IMFs concurrently, which results in modes covering finite bandwidth within the original signal. Being weighted towards central frequencies, IMFs contain physically relevant information of various processes that influence the original signal, see Appendix **??**. In this paper, we use the MATLAB (R2020a) built-in variational mode decomposition function to decompose the velocity, u(t), at a given space into its oscillatory modes. The number of IMFs needed to decompose the signal into physically relevant modes is not known a priori. We vary the number of IMFs between 4 and 6 to decompose the signal. We find that five IMFs are sufficient throughout our data to decompose the signal without any redundancy or loss of modes that appear significant in predicting the droplet dynamics. Increasing the number of IMFs affects the decomposition noise and oscillatory components which are of less interest in this system in the laminar regime.

The goal is to analyze the flow dynamics in a time-domain signal to find a signal that will allow us to determine if uniform droplets are being created at certain instances by viewing a single region within the inlet. This is in contrast with other methods of signal analysis in fluids such as dynamic mode decomposition which require a much larger data set in the entire field.

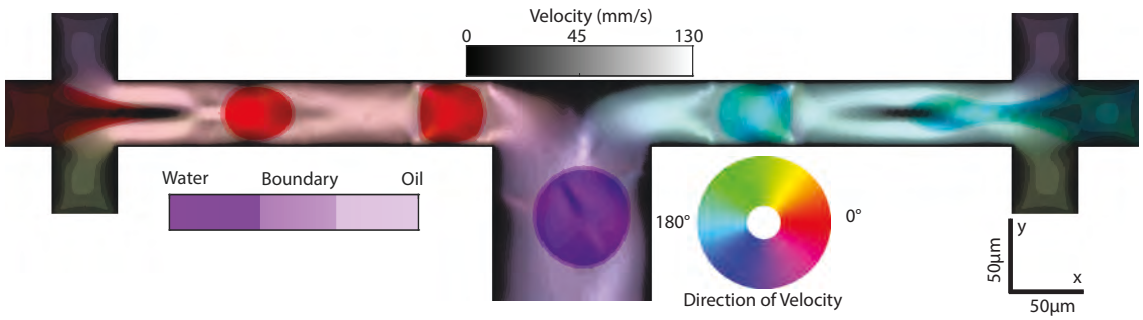

Figure 3.1: Visualization of two-phase fluid and flow velocities in a microchannel where droplets generated from right and left drop-makers meet at the center of the channel. Color Hue represents direction of the velocity, Saturation represents the volume fraction of water, and brightness Value represents the magnitude of the velocity.

3.3 Results

We develop a consolidated visualization method that integrates multiple physical quantities, velocity, and fluid phase, into a simple graphic to better identify different dynamics. To visualize the direction and magnitude of fluid velocities along with the volume fraction of each fluid phase, corresponding colors, intensities, and saturation are assigned to form a single HSV image (Hue, Saturation, Value) as shown in Figure 3.1 (Supplementary Materials). Hue is determined by the angular velocity at each position and is mapped to a 360-degree color wheel with red and cyan corresponding to 0 and 180 degrees, respectfully. Saturation represents the volume fraction of oil and water. Saturation is 1.0, where the volume fraction of water is larger than 55% and 0.25 where the volume fraction is smaller than 45%. Saturation matches the volume fraction of water everywhere else as shown in the Saturation color bar in Figure 3.1 (Supplementary Materials). Moreover, the magnitude of the velocities is represented by Value, which describes how light or dark a Hue is with larger velocities appearing brighter. Since there is an uneven distribution of velocities, with many small velocities and a few large velocities, there is poor contrast within the slow velocity regions. To enhance the contrast in these regions, we use a global transformation that bins and maps velocities across all spatial and temporal points into Values. However, the distinction between the few high velocities is no longer visible. This transformation and mapping, known as histogram equalization, aims to create a uniform probability density function that enhances contrast for tightly grouped velocities. Although it is unlikely to create a completely uniform histogram, histogram equalization generally results in a wider range of the intensity scale to be used and, consequently, the contrast is enhanced [28]. This process is only used for the visualization of the data and the velocities after

histogram equalization are not used in data analysis.

Droplets of water in oil are formed on either side of the long channel and carried by the outer fluid (oil) as shown in Figur). Droplets formed in the left channel appear red as they travel from left to right. These droplets meet droplets from the opposing channel at the T-junction. Droplets either merge or deflect towards the outlet vacating the device while appearing purple due to their now downwards velocity. Interestingly, we observe a considerable number of satellite droplets in the left channel where we intentionally selected non-ideal inlet geometry. Consequently, the sizes of the droplets from the left channel are less uniform and the dynamics at the point of merging become unpredictable with many missed mergers as observed in Figure.

We use variational mode decomposition to analyze temporal flow fluctuations downstream and identify any significant modes. We choose a region of 4×4 μm^2 in the right channel, 290 μm downstream, to investigate where there is less variation in flow velocity away from the inlets prior to the outlet, as shown in Figure 3.2b. We calculate the average flow velocity in this region since our velocity field has a resolution of 200 nm, which is not achievable in most experiments.

Interestingly, droplets pass this region with very little variation in size and shape. We utilize variational mode decomposition to separate fluctuations from the steady flow of droplets and drop formation. Various regions require a different number of modes to produce unique IMFs without frequency and amplitude overlap. We choose five intrinsic mode functions for this position for all IMFs to remain significant and residual to have minimal oscillation. From our visualization of the right channel in Figure 3.1 (Supplementary Materials), no major fluctuations are expected since we see consistent production of uniform droplets. However, IMF 2 and 4 have a large amplitude present at the start of the signal which wanes later in the signal. The maximum amplitude of IMF 2 (IMF 4) from 0 ¡ t ¡ 80 ms (0 ¡ t ¡ 25 ms) is 4.73 (8.83) times greater than the maximum amplitude in the rest of the IMF. The simulation begins with the device filled with oil. Therefore, there are fluctuations in the velocities due to water being introduced to the device. We consider this an initiation stage for the flow. The effect of the initiation of flow is present in IMFs 2 and 4. The amplitude in IMF 3 appears to be modulated periodically, which we attribute to the steady flow of droplets. IMF 5 summarizes both the effect of initiation of flow as well as the periodicity from the flow of droplets. Moreover, the sharp drop in the amplitude in IMF 5 matches the time when IMF 3 transitions to a periodic signal. Additionally, this time is close to where initiation effects in IMF 4 start to wane. The decomposition clearly separates the events affected by the initiation of flow, which appear in IMF 2 and IMF 4, and the steady flow and drop formation that are evident in IMFs 1, 3, and 5. Interestingly, IMF 5 has some of the initiation effects which are

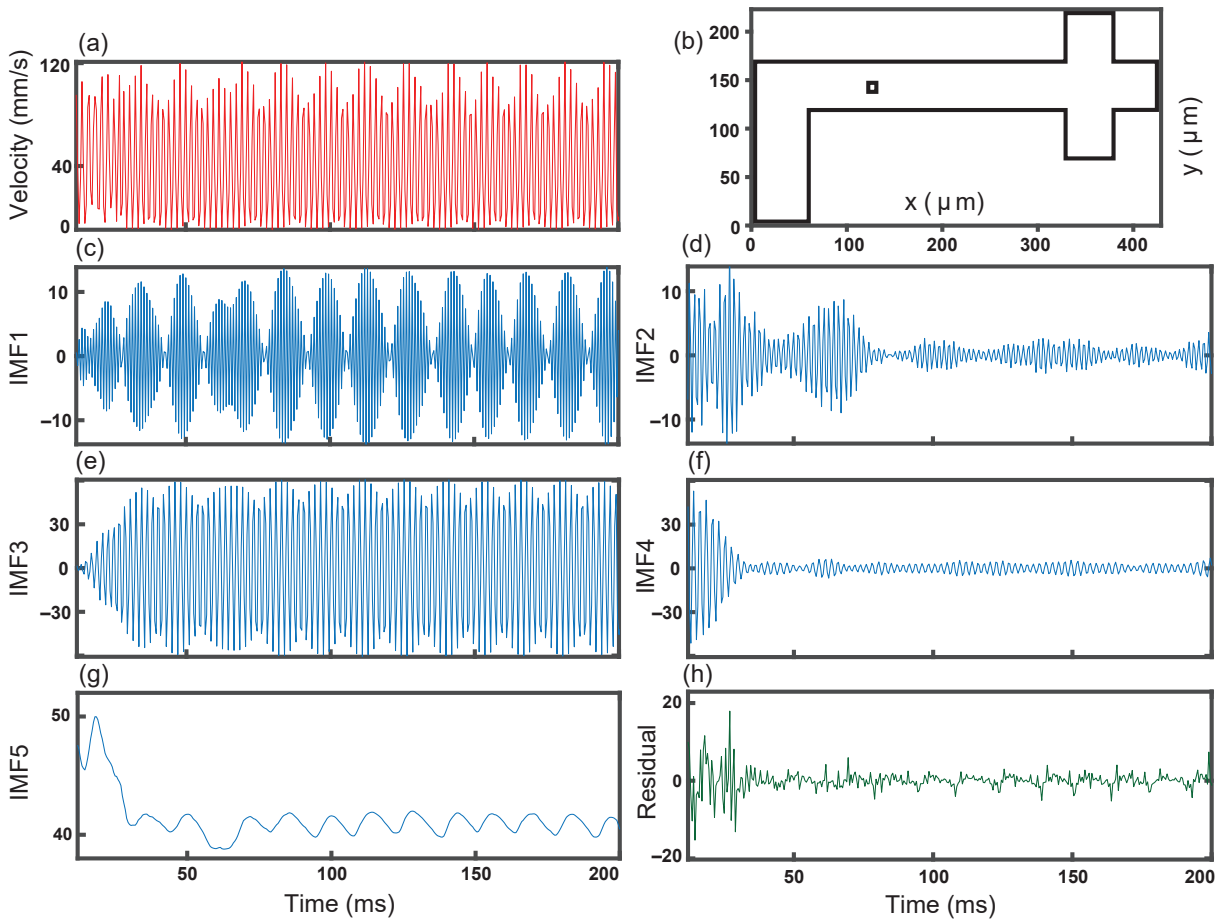

Figure 3.2: Velocity and decomposition at one position as a function of time. (**a**) Magnitude of velocity from 12 to 200 ms (**b**) for a 4 × 4 μm^2 bin in the center of the channel; (**c**) First intrinsic mode function (IMF 1) of the decomposed velocity signal showing the fastest oscillations in the original signal; (**d**) IMF 2, the second largest oscillations heavily affected by the initiation of flow; (**e**) IMF 3 showing the bulk of the original velocity signal; (**f**) IMF 4 slower oscillations with a transition at around 20 ms corresponding to the initiation of flow; (**g**) IMF 5 is the slowest oscillation of the flow with an average close to velocity of the outer fluid at 40 mm/s, and a spike early in the signal at time briefly after the initiation; (**h**) Residual of the signal.

distinct peaks matching the IMF 2 and IMF 4 as well as the fluctuation within relatively consistent signals in IMF 1 and IMF 3 at around 60 ms. The residual does not have any significant physical meaning (Figure 3.2h), except that the signal can be recovered exactly by adding the residual and all other IMFs.

Using variational mode decomposition, we analyze temporal flow fluctuations at both water inlets

and identify any significant modes that indicate changes in droplet formation. We calculate the velocity signal and IMFs of 4×4 μm^2 regions prior to the oil inlets and pinch off points, 20 μm into the water inlets, for the left and right drop-makers shown in Figure 3.3. Interestingly, we observe that the right channel signal and IMFs appear similar to the results found downstream, comparing Figure 3.3h–k to Figure 3.2c–f. The periodicity in IMF 2 coincides with the steady flow of droplets while IMF 3 and 4 show the effects of initiation. Here, IMF 1 is an order of magnitude smaller than the other IMFs. Additionally, IMF 5 contains a peak close to the initiation of the flow and the amplitude falls off close to the average flow velocity after the initiation. We observe that there is almost no periodicity in IMF 5 which is different from data downstream where droplets continuously pass through. The decomposition of the signal for the left channel at the water inlet leads to IMFs with highly variable amplitudes. The amplitudes of IMFs 1 to 3 are comparable to each other and are larger than that of IMF 4, as can be seen in Figure 3.3b–e. We observe multiple large peaks in IMF 5 which are of the same order of magnitude as the effect due to the initiation of flow. By contrast, there is a plateau in IMF 5 during the time interval, 115 ¡ t ¡ 155 ms. Interestingly, this plateau in IMF 5 coincides with the formation of uniform droplets from the left channel. Moreover, during this time interval, the amplitude of IMF 3, which has the largest range among all IMFs, is at its minimum. IMF 4 is also at its minimum during this time interval. We observe that IMF 2 during this time interval has a behavior similar to what is seen in uniform droplet formation in the right channel. Additionally, IMF 2 contains most of the original signal during this time interval. Satellite and non-uniform droplets are formed in the left channel at all other times. The effect of initiation is apparent in IMF 3 and 4 in the right channel, Figure 3.3j,k, while, in the left channel, this effect is not the most significant change in amplitude in any of the IMFs, Figure 3.3d,e, and becomes suppressed. It should be noted that the signal obtained from the left water inlet ranges between 1 mm/s while the signal from the right channel ranges 0.2 mm/s. Additionally, IMF 1 for the left channel (Figure 3.3b) has amplitudes an order of magnitude larger than that seen in IMF 1 of the right channel (Figure 3.3h). IMF 1 contains the highest oscillating component of the signal which is typically attributed to noise in the system.

Our analysis of the decomposed signal demonstrates and predicts if uniform and non-uniform droplets will be formed; surprisingly, our prediction is based on the signal in the region before where droplets are pinched off. Naturally, it is difficult to predict the formation of uniform droplets from this region. We identify characteristics in the decomposed signal that indicate time intervals when uniform droplets are formed. It appears that the peaks in IMFs 3 and 4 mostly coincide with fluctuations that destabilize the formation of uniform droplets. Uniform droplets are formed whenever there is a plateau in IMF 5. To better define the plateau, the average and standard deviation of the IMF 5 are calculated on a moving window of at least 7 ms, corresponding to the

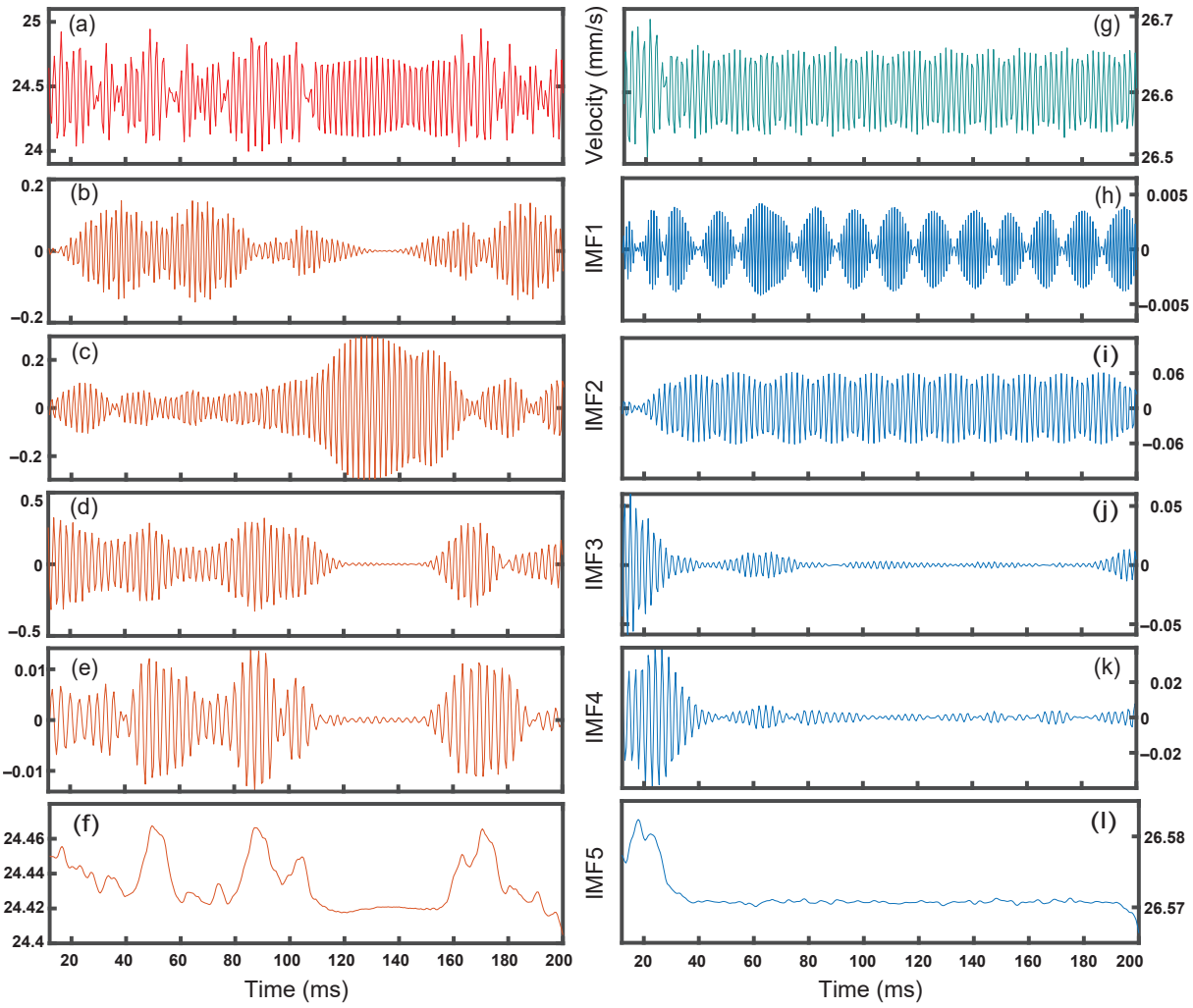

Figure 3.3: Velocity and decomposition in the water inlet as a function of time. **Left**: the velocity signal (**a**) and decomposition into intrinsic mode functions (**b**–**f**) for the left channel of Figure 3.1 (Supplementary Materials) demonstrates various large fluctuations. **Right**: velocity signal (**g**) and decomposition (**h**–**l**) for the right channel with a single large fluctuation.

time needed to form two droplets. The fluctuations in the IMF 5 can be ignored as long as this local standard deviation is smaller than 0.02. To predict if a uniform droplet is formed, we calculate the standard deviation of IMF 5 over 7 ms before this time-step, assuming we have no information about future velocities.

To investigate the applicability of the signal decomposition in lower resolution data, we study the relationship between various spatial resolutions of the signal and decomposition. Additionally, this

helps with evaluating the relevance of this method for experimental data considering simulations that generally have higher spatial resolutions than in experiments. We analyze two velocity signals taken from the same position, centered between the oil inlets, at different resolutions ranging from 4×4 to 20×20 μm^2. To quantify the similarities in the IMFs, we calculate the maximum normalized cross-correlation of the above signals with the signal obtained from a 1×1 μm^2 region (5×5 pixels^2):

$$IMFcorr_{ij} = \frac{\sum_{n=1}^{N-m-1} IMF_{i,n+m}^{(1)} IMF_{j,n}^{(2)}}{\sqrt{\sum_{N}^{n=1} |IMF_{i,n}^{(1)}|^2 \sum_{N}^{n=1} |IMF_{j,n}^{(2)}|^2}} \tag{3.1}$$

where i and j represent the IMF number, and n and m are the elements in each IMF. The superscript (1) and (2) represent the different resolutions of the data. In our calculations, we choose (1) to be at the 1×1 μm^2 resolution and vary (2) between 4×4 μm^2 and 20×20 μm^2. Here, $IMFcorr_{ij}$ is an array with values between -1 and 1. We expect, for $i = j$ at a coincident time, $IMFcorr_{ij}$ to be highly correlated. However, on rare occasions there is a time lag between the signals because we are averaging over a larger window that encompasses fluid elements in nearby locations. Hence, we report the maximum of this array for every combination of IMFs.

Comparing the velocities averaged over a 4×4 and 20×20 μm^2 region centered between the two oil inlets, we find that the higher resolution has larger average velocities. This is natural since the lower resolution signal is averaging velocities closer to the wall, which are slower velocities than the center, as seen in Figure 3.4a. The different IMFs from the two resolutions are barely different in amplitude and frequency from one another as seen in Figure 3.4b–g. Small differences are observed in IMF 1, which is an order of magnitude smaller than the other modes, Figure 3.4b. We attribute these differences at this position to the 20×20 μm^2 window extending into the water channel which has additional inlet noise. Our calculation of the maximum $IMFcorr_{ij}$ demonstrates that the coinciding IMFs are highly correlated regardless of spatial resolution, Figure 3.4h. Additionally, non-coinciding IMFs have very little correlation as demonstrated by the extremely small and negligible sizes of the correlation bubbles in Figure 3.4h. The lowest maximum $IMFcorr_{ij}$ of the coinciding IMFs is 0.97 seen for IMF 4 of the 20×20 μm^2 region. It is apparent that the results of the decomposition are weakly dependent on spatial resolution up to 20×20 μm^2 when using a 1×1 μm^2 region. Our results imply that this method should work on lower resolution experimental data. Additionally, IMFs 2 to 4 and the residual match closely between the two different resolutions.

To verify the robustness of this method, we calculate the maximum normalized cross-correlation, $IMFcorr_{ij}$, across the center of the channel averaged for different positions. To avoid overlaps of

the larger window, we choose these positions to be 65 μm apart. We calculate the $IMFcorr_{ij}$ for the signal obtained from a 1 $\times$ 1 μm^2 window correlated with the 4 $\times$ 4, and the 20 $\times$ 20 μm^2 windows. Interestingly, IMF 5 remains highly correlated regardless of window size and position in the channel as shown in Table 3.1. Coinciding IMFs are heavily correlated for the 4 $\times$ 4 μm^2 window size with very little correlation amongst non-coinciding IMFs, as can be seen by comparing the diagonal elements of Table 3.1 with the off-diagonal elements. These results clearly show that the 4 $\times$ 4 μm^2 window is small enough and the decomposed signal matches the 1 $\times$ 1 μm^2 window closely (max($IMFcorr_{ij}$) > 0.99). However, the $IMFcorr_{ij}$ for $i = j$ for IMFs 2, 3, and 4 are less correlated for the larger window size, 20 $\times$ 20 μm^2. Here, the off-diagonal elements ($i \neq j$) increase as seen in Table 3.2.

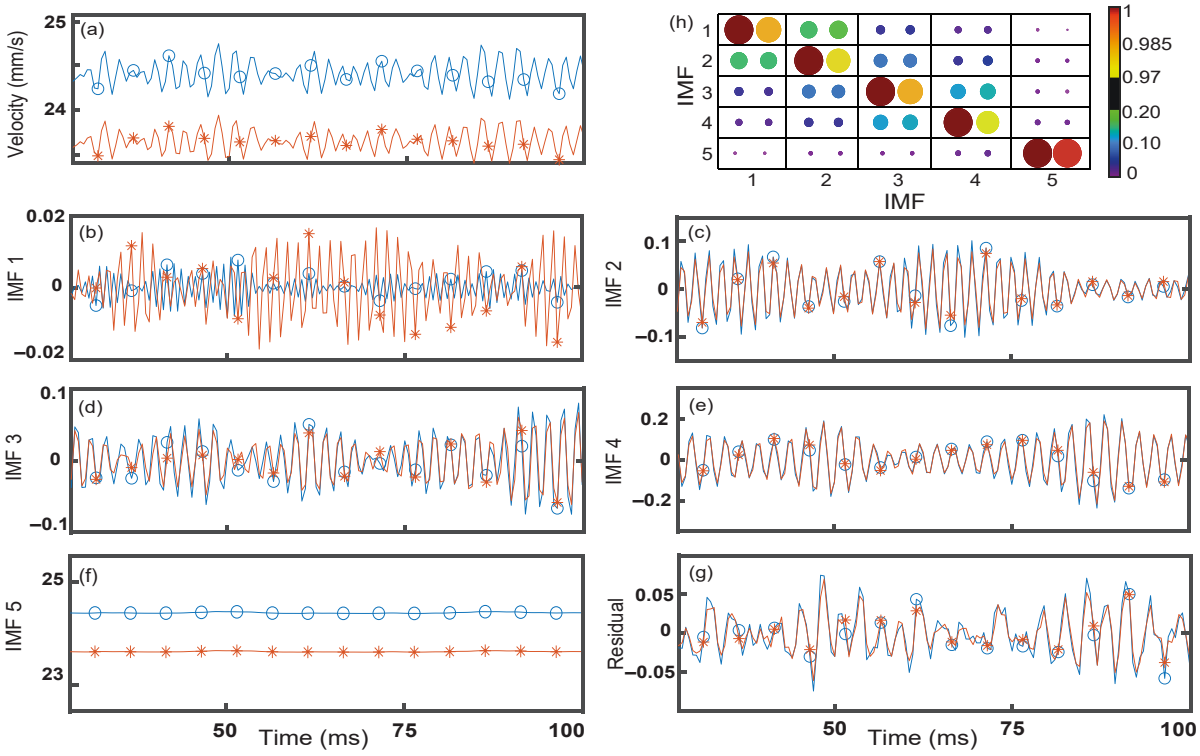

Figure 3.4: Velocity signal (**a**) taken at a single position averaged for two different resolutions, 4 $\times$ 4 μm^2 (blue circles) and 20 $\times$ 20 μm^2 (orange asterisk); (**b**–**g**) the respective Intrinsic mode functions; (**h**) normalized maximum cross correlation between the IMFs of the 4 $\times$ 4 μm^2 (left) and 20 $\times$ 20 μm^2 (right) with a 1 $\times$ 1 μm^2 region. Color bar and relative size represent the strength of the correlations.

Upon further investigation, IMF numbers swap occasionally when decomposing signals from different window sizes or neighboring positions. An example of this swapping is demonstrated for

	IMF 1	**IMF 2**	**IMF 3**	**IMF 4**	**IMF 5**
IMF 1	1.0000	0.1003	0.0293	0.0239	0.0038
IMF 2	0.1003	0.9999	0.0808	0.0447	0.0052
IMF 3	0.0293	0.0805	0.9998	0.1500	0.0054
IMF 4	0.0240	0.0446	0.1487	0.9997	0.0125
IMF 5	0.0038	0.0052	0.0054	0.0124	1.0000

Table 3.1: Maximum normalized cross correlation averaged over 12 positions with areas of 4 $\times$ 4 μm^2 region. The IMF 1 to 5 on the columns are from the 1 $\times$ 1 μm^2 and the rows are from the 4 $\times$ 4 μm^2.

Table 3.2: Maximum normalized cross correlation averaged over 12 positions with areas of 20 $\times$ 20 μm^2. The IMF 1 to 5 on the columns are from the 1 $\times$ 1 μm^2 and the rows are from the 20 $\times$ 20 μm^2 region.

	IMF 1	**IMF 2**	**IMF 3**	**IMF 4**	**IMF 5**
IMF 1	0.9090	0.1622	0.0326	0.0240	0.0037
IMF 2	0.1663	0.4976	0.3705	0.0486	0.0051
IMF 3	0.0332	0.2301	0.5048	0.3761	0.0053
IMF 4	0.0263	0.0518	0.2601	0.6468	0.0124
IMF 5	0.0039	0.0061	0.0061	0.0093	0.9997

two window sizes (4 $\times$ 4 and 20 $\times$ 20 μm^2) at the center of the channel in Figure 3.5. Here, swapping IMFs 2 and 3 of the larger window would result in a greater $IMFcorr_{ij}$. Interestingly, this swapping seems to be contained to IMFs 2, 3, and 4. These three IMFs are small in magnitude and similar in frequency where small changes in the average signal can swap their assigned IMF number. Additionally, the swapping is predominately amongst neighboring modes, IMFs 2 and 3 and IMFs 3 and 4 swapping. The prevalence of swapping increases with window size as additional velocities further from the center of the channel are being averaged into the signal prior to decomposition. However, IMF 1 remains highly correlated regardless of window size up to 20 $\times$ 20 μm^2. The most consistent mode is IMF 5 as it was heavily correlated (Max($IMFcorr_{ij}$) $>$ 0.99) even when using a 20 $\times$ 20 μm^2 window size at various positions. We observe that IMF 5 is a good indicator for changes in droplet formation and remains strongly correlated regardless of the spatial resolution tested.

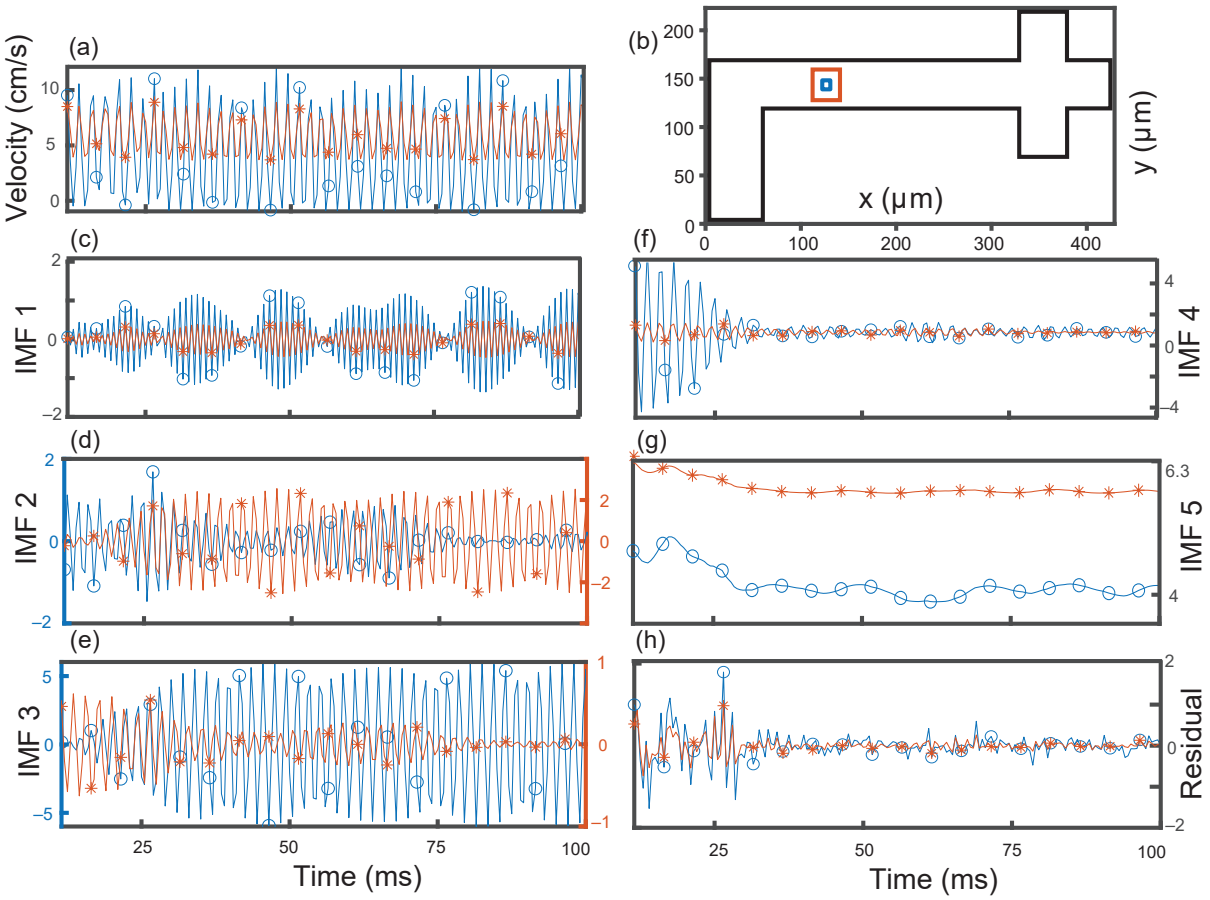

Figure 3.5: Velocity signal and decomposition at one position as a function of time. (**a**) magnitude of velocity from 12 to 200 ms (**b**) for a 4 × 4 μm^2 (blue circles) and 20 × 20 μm^2 (orange asterisk) window size at the center of the channel; (**c**) first intrinsic mode function (IMF 1); (**d**) IMF 2 where the larger window decomposition swaps with IMF 3; (**e**) IMF 3 where the larger window swaps with IMF 2; (**f**) IMF 4; (**g**) IMF 5, (**h**) Residual.

3.4 Discussion

We simulate the formation of water in oil droplets and extract a high resolution velocity field from the simulation. In this microfluidic drop-maker, we incorporate two independent drop-makers with slightly different inlet geometries—in one of which the inlet is shorter than the other. The short inlet leads to the formation of satellite droplets at the same flow conditions as the other inlet. Using variational mode decomposition, we decompose the velocity signal at the center of the channel into its intrinsic modes. We show that, by only decomposing the signal into five intrinsic modes, we can fully separate the oscillatory and noisy parts of the velocity from an underlying average flow at the center of the channel. Interestingly, IMF 5 carries most of the physical information. IMF 5 has

distinct spikes when the flow is initiated and it transitions into a plateau as long as the droplets are uniform. The IMF 5, of variational mode decomposition, has a smooth shape when uniform droplets are formed even if we analyze the velocities in the water inlet and before the region where droplets form. Additionally, this method is not sensitive to the spatial resolution of the signal, as we decompose a velocity signal averaged over a considerably large area. We show that magnitude of IMF 5 remains to be highly correlated with the high resolution velocities further confirming the robustness of prediction of flow fluctuations by IMF 5. By choosing the appropriate number of modes, we efficiently separate the physical part of the signal from oscillatory and noisy parts. Our analysis provides a metric to predict uniform and satellite droplet formations.

The variational mode decomposition is a promising method of signal decomposition suitable for fluid flows with random or periodic fluctuations. Additionally, VMD is integrated into scientific software such as MATLAB, making it readily accessible to a broad range of users. Moreover, VMD can be applied to spatially sparse data without losing critical information about the underlying signal, as we demonstrate in this paper. While some of the conventional methods of signal analysis, such as Fourier transform and Dynamic mode decomposition, have been used in different areas of fluid mechanics, mainly in turbulence and channel flows, the use of signal analysis in microfluidics has received less attention. Nevertheless, the integration of microfluidics circuits in commercial platforms for sorting and processing small volumes of fluids is rapidly growing. Hence, the application of signal analysis in microfluidics for optimization, troubleshooting, and quality assessments is on the rise. Here, we demonstrate the successful application of VMD in predicting droplet sizes and provide a platform for future use of VMD in microfluidics signal analysis. Future exploration of the application of this method and extension into experimental and real time analysis can improve the performance of microfluidics chips with single point velocity monitoring.

3.5 Variational Mode Decomposition

Variational mode decomposition separates a signal into components that can be expressed mathematically as amplitude-modulated-frequency-modulated signals [25]. This is in contrast with Fourier transform which describes a signal as a sum of non-varying sinusoidal functions. A mode, u_k, in VMD is described as

$$u_k(t) = A_k(t)cos(\Phi_k(t)) \tag{3.2}$$

where A is the time-dependent amplitude and Φ is the phase. Decomposing a signal into functions that can vary over time allows VMD to become locally adaptive and have the ability to act as a

narrow band filter. The robust nature of such a decomposition method effectively allows VMD to decompose signals from nonlinear and non-stationary systems [25]. A real function can be represented as an analytic signal that is comprised of the original function and its Hilbert transform as:

$$f_A(t) = f(t) + i\mathcal{H}f(t) = A(t)e^{i\phi(t)} \tag{3.3}$$

Here, $\mathcal{H}f(t)$ is the Hilbert transform of the signal, $f_A(t)$ represents the analytical representation of the signal, and $A(t)$ is the instantaneous amplitude and envelope of the signal. Instantaneous frequency is found by the rate of change of the $\phi(t)$. The mode u_k can be expressed as analytic signals. This allows us to represent the mode in the form of a complex exponential with no negative frequencies:

$$u_{k,A}(t) = u_k(t) + i\mathcal{H}u_k(t) = A_k(t)e^{i\phi(t)} \tag{3.4}$$

In summary, variational mode decomposition utilizes frequency mixing and Hilbert transforms to extract narrow band functions from a signal [25]. This minimization problem is framed by attempting to simultaneously finding a unique number of functions, or modes, around different central frequencies that sum to the original signal. These central frequencies, ω_k, are initialized randomly or selected and are then mixed with a mode of varying phase and amplitude that is narrow-band limited around the respective central frequency. The central frequency is then updated by utilizing the center of mass of the mode's power spectrum. Additionally, the modes are determined adaptively and concurrently to balance the errors between them:

$$\min_{\{u_k\},\{\omega_k\}} \left\{ \sum_k \left\| \partial_t \left[\left(\delta(t) + \frac{i}{\pi t} \right) * u_k(t) \right] e^{-i\omega_k t} \right\|_2^2 \right\} \quad s.t. \sum_k u_k(t) = f \tag{3.5}$$

where $i/\pi t$ denotes the impulse response of a Hilbert Transform. Consequently, the convolution of $i/\pi t$ and the estimated mode results in an analytic signal. The analytical signal is then mixed with the signal containing the estimated central frequency, ω_k. This results in modes frequency spectrum shifted into "baseband" by their respective estimated center frequencies for all k's. The bandwidth of these modes are then estimated by the L^2 Norm of the gradient resulting in a constrained variational problem, Equation (3.5). To render the problem unconstrained, Dragomiretskiy and Zosso recommend using Lagrangian Multipliers and a quadratic penalty term [25]. Additionally, the alternate direction method of multipliers can be used to perform a sequence of iterative sub-optimizations to find the solution to the final minimization problem. A full solution is provided in Dragomiretskiy and Zosso's article.

Chapter 4

Methods

4.1 Introduction to Methods

The methodology outlined here details the procedures and techniques used to study the intermittent transport of emulsions in porous media. The aim is to provide a comprehensive guide to the experimental and analytical methods, ensuring reproducibility and clarity for future research. The subsections systematically cover various aspects of our methodology, offering an in-depth insight not covered in previous publications.

We begin with the design process using AutoCAD 3D, specifying the dimensions and structural elements critical for our experiments. A section on computationally and automatically characterizing the porous designs is addressed next. Following this, the 3D printing techniques are detailed, encompassing the selection of resin, printing profiles, and post-processing steps such as UV and heat curing, and washing. The preparation of Poly(dimethylsiloxane) (PDMS), with a focus on its properties, ratio, and bonding methods, is also thoroughly discussed. Additionally, the application of Aquapel (PGW Auto Glass, LLC, Cranberry Township, PA, USA) for creating hydrophobic surfaces is explained, highlighting its significance in droplet formation and pressure management. The preparation and setting of the device, involving flushing with HFE and drying processes, are outlined to ensure readiness for experiments.

The experimental setup section provides a comprehensive guide to setting up the apparatus, including the pressure transducer, tubing connections, fluid preparations, and the use of Arduino for generating pressure pulses. Finally, the data processing section covers the image processing

techniques employed, including background subtraction, stabilization, local contrast enhancement, and adaptive binarization, along with the development of tracking algorithms, cost matrices, and visualization tools. This structured approach ensures a detailed and replicable methodology, aligning with the rigorous standards required for scholarly research in the field of emulsion transport in porous media.

Ultimately, the design encompasses a comprehensive experimental setup. At its core is the microfluidic chip, housing both the on-chip drop-maker and the 2D porous medium. Precise droplet production is ensured through modulated flow rates delivered by a pressure pulse to the water inlet. Imaging and monitoring of the droplet dynamics within the porous medium are facilitated by a high-resolution Zeiss Microscope (Axiozoom), paired with a FasTec IL5 camera to capture the intricate details of the droplets. The syringe pump stands as a consistent tool in delivering a controlled flow of the continuous phases into the system. Real-time pressure data across the medium is collected through a pressure transducer, specifically an Omega-PX409. Completing the setup is a stage, ensuring that the microfluidic device remains securely in place for stable visualization. This integrated system aims to address the challenges of studying emulsion dynamics, offering precise control and detailed visualization.

4.2 Emulsion Generation and Control

In efforts to mimic the slow flow regimes found in natural subsurface flows, specifically $v_{int} \sim 1$ ft/day or 3 μm/s, our microfluidic drop-maker is engineered to function within the dripping regime, as described by Utada et al. [80]. The core design of the drop-maker features a central inlet for the dispersed fluid, composed of water mixed with 0.1 wt% fluorescein sodium salt. Alternatively, food dye can replace fluorescein in some experiments, offering higher contrast images despite altering the surface tension. This is discussed in detail in a future chapter. The central inlet is flanked by two inlets for the continuous phase, which consists of a specialized fluorinated oil, HFE750 (from 3M), mixed with 5 wt% FSH surfactant oil (from Krytox). The interfacial tension between these phases is measured at $\gamma = 26$ mN/m.

In the dripping regime, the size of the droplets is primarily governed by the inlet geometry, as shown by Barkley et al. [4]. At equilibrium, the pressure inside the droplet (P_d) balances with the pressure of the outer fluid (P_0) and the capillary pressure, following the relation $P_d = P_0 + \frac{2\gamma}{R_d}$, where R_d is the droplet radius. The droplet detaches when the internal droplet pressure exceeds the external pressure, with the droplet radius $R_d > 2R$ in a channel of radius R, assuming a circular

cross-section. This behavior, thoroughly examined in Barkley's 2016 paper, is reproduced here with different geometry but similar results.

Achieving a low flow rate for uniform droplet formation requires maintaining the low flow limit and stability. Surfactants stabilize droplets, ensuring uniformity and preventing breakup and coalescence. Creating a Pressure Collar involves using a hydrophobic coating to promote the formation of a pressure collar, facilitating backward flow of the continuous phase into the inlet, essential for the snap-off mechanism. Geometry significantly influences droplet generation, with the rectangular inlet shape playing a crucial role. Unlike Barkley's 2016 study on circular nozzles, the focus here is on how the rectangular geometry affects droplet size, which is largely determined by the channel design and effective radii. An innovative hybrid design combines pressure pulses and flow control for precise droplet generation, addressing issues such as fluid viscosity and inconsistent droplet sizes.

Laplace Snap-Off Physics, at the core, uses Laplace principles for controlled droplet breakup, enabling fine-tuning of droplet size and frequency for accurate experiments. The channel geometries and pressure systems are engineered for precision, ensuring predictable droplet creation, crucial for emulsion transport studies. Pressure-Induced Flow-Driven Droplet on Demand relies on surface tension, the fluid's inherent tendency to minimize its surface area, playing a critical role in shaping and stabilizing droplets. Laplace Pressure in droplets refers to the pressure difference across the curved surface of a droplet, driven by surface tension. In a droplet of radius R_d, internal pressure (P_d) competes with surface tension's contracting force.

The importance of nozzle design lies in forming a pressure collar (P_c) at the nozzle-dispersed fluid interface, necessitating reverse flow of the continuous phase into the nozzle for effective droplet detachment. As the droplet radius (R_d) increases, internal pressure (P_d) decreases, leading to snap-off when $P_c < P_0$ (ambient pressure). The pressure drop from nozzle pressure (P_n) to P_d occurs over a length scale $L + \epsilon R_d$. Despite the small flow term (Q) for the dispersed fluid, the process is quasi-static. Maintaining a low flow rate of the dispersed fluid ensures uniform droplet formation, with small pressure pulses initiating controlled flow (Q), crucial for consistent droplet size.

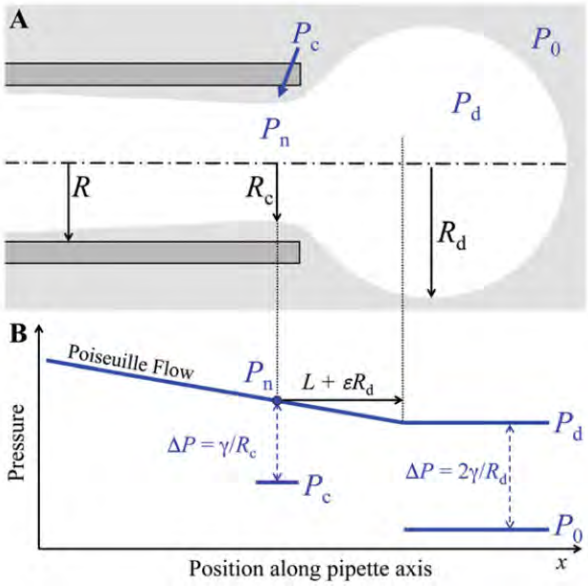

Figure 4.1: (A) Schematic prior to droplet snap-off. Key length scales include the inner radius of the cylindrical nozzle R, minimum radius of the dispersed phase column within the nozzle R_c, and the radius of the growing droplet R_d. Relevant pressures are the bulk continuous phase pressure P_0, the dispersed phase pressure in the growing droplet P_d, the dispersed phase pressure in the nozzle P_n, and the continuous phase pressure in the collar around the dispersed phase P_c. (B) Pressure schematic along the pipette length. Snap-off occurs if $P_c < P_0$, as R_d grows, decreasing P_d and other pressures relative to the fixed P_0. Figure taken from Barkley 2016 [4].

4.3 General Fabrication and Design

In conclusion, our study successfully emulates the slow flow regimes observed in natural subsurface flows integrated with the precise operation of a microfluidic drop-maker operating within the dripping regime. By meticulously controlling the inlet geometry, surfactant usage, and flow rates, we achieve uniform droplet formation critical for emulsion transport studies. The integration of pressure pulses and innovative channel designs, along with an understanding of Laplace principles and surface tension dynamics, ensures the reproducibility and precision necessary for accurate experimental outcomes. This approach not only aligns with the findings of Barkley et al. [4] but also demonstrates the robustness and versatility of our microfluidic system in producing consistent and stable droplets.

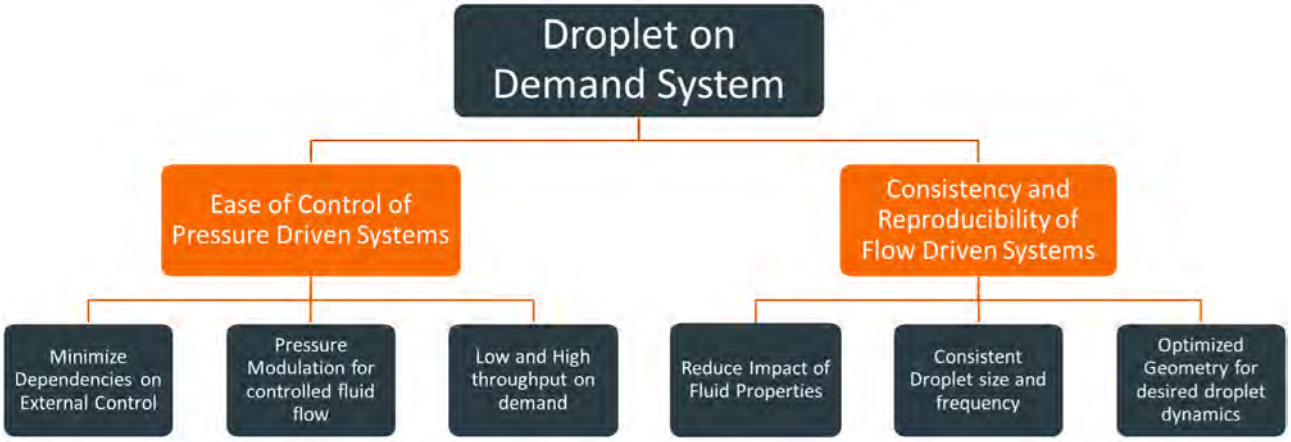

Figure 4.2: Droplet Generation and Control.

4.4 General Fabrication and Design

The 2D porous media were designed and constructed using established soft lithography and microfluidic methodologies [83]. The approach for creating a pattern with a random pore size distribution involved using a 2D micrograph of a three-dimensional glass bead-pack captured through confocal microscopy [1]. To enhance the heterogeneity in pore size, a gradient in pore size distribution, with increased porosity at the inlet compared to downstream sections, was introduced. This gradient is reflective of the variance found in natural and geological porous formations [8]. The porosity and pore size distribution in the 2D porous structure were measured using a novel algorithm rooted in Voronoi tessellation and skeletonization techniques [22, 41, 42, 82].

To guarantee that emulsion droplets could seamlessly enter the medium, the physical dimensions of the porous medium were modified to facilitate the droplets' passage by scaling appropriately. For these experiments, a microfluidic 3D printer, specifically the CADworks3D Pr110-385nm model, was deployed. This advanced resin-based 3D printer, possessing an XY resolution of 40×40 μm^2 and a Z resolution of 5 μm, allowed for the crafting of master molds in various dimensions. To ensure the master mold exhibited smooth surfaces, which is imperative for optimal microfluidic device functionality, the printing parameters were fine-tuned using a commercial powder-based resin characterized by minimal light scattering. By adeptly managing UV exposure and curing durations, fine edges and smooth surfaces were achieved. Subsequently, these master molds were filled with polydimethylsiloxane (PDMS), followed by curing at 60-75°C. The final step involved plasma cleaning and securing them onto a glass slide.

A method to design and fabricate microfluidic molds and devices rapidly using a high-precision and high-resolution 3D printer and specialized photo-resin compatible with PDMS was optimized.

This method aimed to produce microfluidic devices within one week's time, following the protocol and method developed here. This approach resulted in a resource capable of fabricating complex microfluidic devices in-house.

4.5 AutoCAD 3D Design

To design the experimental structures critical for studying the intermittent transport of emulsions in porous media, AutoCAD 3D was utilized. The design process began with creating a 2D base and integrating the drop-maker and microfluidic device. Pillars were added to the 2D inlet regions, and all 2D objects were converted to regions. The porous media, mixing chambers, and initial fluid mixing and filters around the inlet were subtracted from the main region to create depressed regions, which were then extruded into 3D solid objects. This method allowed for precise and functional molds for our experiments.

4.5.1 Base Thickness

The base thickness was set at 2 mm to ensure structural integrity during the heat curing process, minimizing deformation. During initial tests, thinner bases were prone to warping and bending, compromising the device's functionality. A thicker base was necessary to prevent such issues, although it increased printing time and resin usage. This thickness was found to be optimal for maintaining the shape during curing stages.

4.5.2 Negative Space

Negative space was strategically designed by placing objects where voids were desired in the final microfluidic device. This ensured that elevated regions in the mold translated to solid structures in the PDMS device, essential for the functionality of the microfluidic channels and chambers.

4.5.3 Wall Structures

Wall structures were designed to be thick enough to prevent breakage when PDMS was extracted from the molds. During early trials, thin walls often broke at the edges, leading to failed experiments. Angling the walls helped relieve pressure during 3D printing, allowing resin to flow more

easily and reducing the risk of defects. For our experiments, a wall height of 7 mm and thickness of 2 mm was optimal. This design ensured robustness and minimized the likelihood of leaks through the tubing inlet.

4.5.4 Pillars

Pillars were designed to securely hold the polyethylene microtubing without leaks. The upper region of the pillars had a diameter of 0.8 mm, increasing to 1.1 mm at 3 mm down the pillar. This design allowed fluid to pool and flow uniformly. Initial pillar designs failed to securely hold the tubing, leading to leaks. Adjusting the pillar dimensions ensured a tight fit. The tubing used had an I.D. of 0.86 mm and an O.D. of 1.32 mm (Cat. BB31695-PE/5-(5) from Scientific Commodities). This sizing ensured a slight pinch for secure insertion without hindering flow.

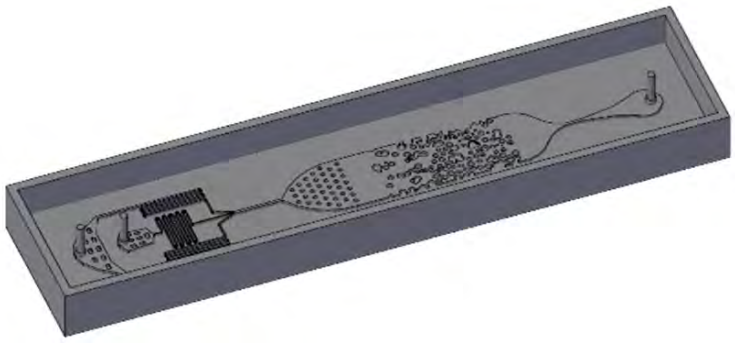

Figure 4.3: Example of 3D Design of microfludic chip mold.

4.6 Porous Characterization

The porous media is a 2D slice selected from a 3D glassbead pack network captured using confocal microscopy. The properties of the porous media were further analyzed using a custom MATLAB code written specifically for this study. This code calculates critical metrics such as dimensions, void percentage, solid percentage, total volume, solid area/volume, void area/volume, and average pore throat size. The analysis begins with an image of the porous media designed in AutoCAD. The image is converted to binary format, and a Euclidean distance transform is applied, followed by skeletonization to identify the media's centerline. Delaunay triangulation is then utilized to determine pore centers and measure pore throat sizes. The code also includes steps to filter closely spaced

points for accuracy. The results are visualized through various figures, including the skeleton, Delaunay triangulation, and pore throat distribution, and are summarized in a detailed message box, providing a comprehensive understanding of the porous media's structural properties. Additionally, the final device can also be characterized by making a mask of the solid structure from an image of the fabricated device. This provides more accurate characterization due to it being of actual physical network being used in experimentation.

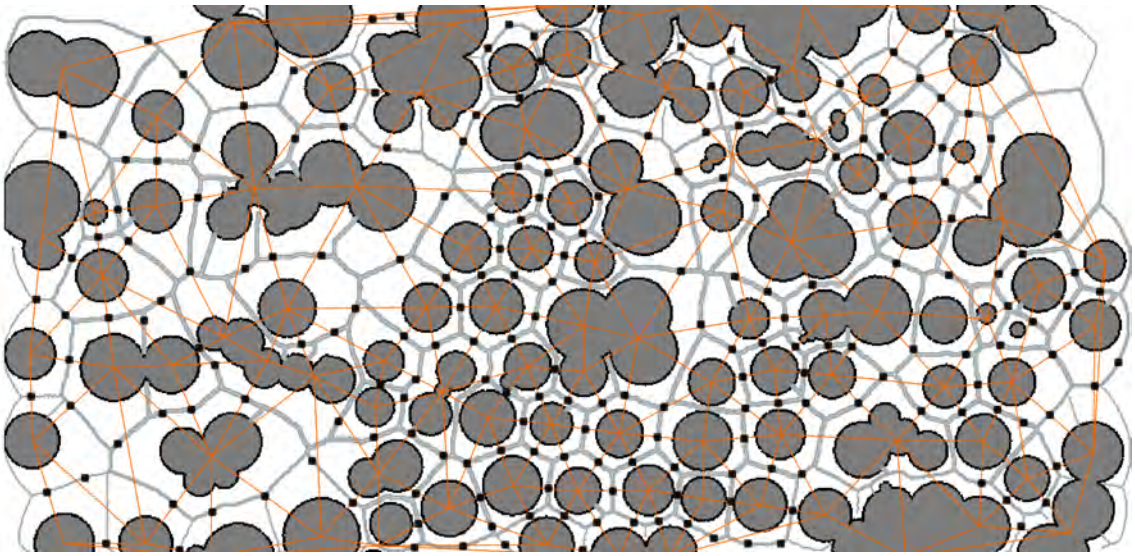

Figure 4.4: Example of Delaunay Triangulation of Porous Media - The image shows the thinned skeleton (gray lines), Delaunay triangles (orange lines), and thresholded points (black circles) used to analyze pore throat sizes and geometric properties.

4.7 3D Printing and Printer Limitations

The design of experimental structures using 3D AutoCAD was brought to life through extensive use of resin-based 3D printing. Adhering to the constraints of the 3D printer, the design ensured that no features were smaller than the printer's resolution limits. The printer used, the Pr110-385nm from CADworks3D, had an X:Y resolution of 40 µm and a Z resolution of 5 µm. Designing within these parameters was crucial for achieving consistent and high-quality prints. Initial attempts to print finer details below the resolution limit resulted in inconsistencies and poor print quality, emphasizing the importance of adhering to printer capabilities.

The printer employed was a Digital Light Processing (DLP) printer, which utilizes UV light to cure

a photosensitive resin into solid objects. The STL file designed in 3D AutoCAD was converted into a layered file format, guiding the printer through the printing process. Proper settings were crucial for achieving high-resolution prints and minimizing failed attempts.

4.7.1 Printer Setup and Process

The printer setup included a build plate, a vat of resin, and a Teflon sheet at the vat's bottom. The process followed these steps:

- **Layer Projection:** UV light projected by a digital light projector cures each resin layer onto the build plate. The low surface energy of the Teflon sheet prevents the cured layer from adhering to it and onto the build plate instead.
- **Layer Building:** The build plate rises incrementally, and this process repeats layer-by-layer until the print is complete.
- **Post-Processing:** Post-printing steps included washing, UV curing, and heat curing to prepare the model for use in creating PDMS devices.

4.7.2 Principles of DLP 3D Printing

DLP 3D printing relies on photochemistry and photopolymerization principles:

- **Photopolymer Resin Composition:** The resin comprises a monomer and a photoinitiator. The photoinitiator, upon exposure to light, triggers the polymerization of the monomer, solidifying the resin.
- **Light Projection:** The digital light projector projects an image of each cross-section of the 3D model onto the resin, solidifying the exposed areas. This forms a standing wave pattern, where the resin solidifies in specific regions.
- **Control of Mechanical Properties:** The intensity and duration of light exposure affect the final mechanical properties of the cured resin, such as hardness, flexibility, and transparency. The photoinitiator absorbs light energy, converting it into chemical energy, which initiates polymer chain formation.

- **Influencing Factors:** The rate and extent of polymerization are influenced by factors like the concentration of the photoinitiator, light intensity, wavelength, and temperature. These factors enable precise control over the printing process, ensuring high-resolution, detailed, and consistent parts.

4.7.3 Optimizing Print Quality

- **Material Selection:** Different resins with varying properties such as viscosity, curing time, and mechanical strength were evaluated to achieve the desired resolution and structural integrity.
- **Environmental Control:** Maintaining a controlled printing environment (temperature, humidity, and cleanliness) was necessary to ensure repeatable and high-quality prints.
- **Balancing Speed and Quality:** Optimizing the balance between print speed and quality was crucial. Faster print speeds often compromised resolution and surface finish, so settings were adjusted accordingly.
- **Support Structures:** For complex geometries, support structures are required to prevent deformation and collapse during printing. Their placement are optimized to minimize surface quality impacts and ease post-printing removal. For our designs, it was crucial to eliminate any need for support structures as additional features create exposure to surface and print defects.
- **Dimensional Accuracy:** Regular calibration and maintenance of the printer ensured dimensional accuracy. A test cube was periodically printed to assure dimensional accuracy.

4.7.4 Practical Considerations

- **Cost Efficiency:** Efficient use of materials and optimization of print settings helped manage costs without compromising quality.
- **Iterative Design Process:** Numerous iterations and adjustments addressed challenges and optimized model functionality, ensuring final structures met experimental requirements.

In conclusion, understanding and working within the limitations of the Pr110-385nm printer was a critical aspect of the design process. By addressing these constraints, we were able to produce

high-quality, functional models that met our experimental needs. Leveraging DLP 3D printing technology allowed for the precise and high-resolution creation of experimental models. The next section will detail the specific methods and techniques used to successfully transition from design to physical prototypes, illustrating the integration of 3D printing in the development process.

4.7.5 Resin Selection

Selecting the appropriate resin was a critical step in achieving high-quality prints and ensuring compatibility with subsequent experimental procedures. Initially, a high cost microfluidic resin from CADworks3D was chosen due to its compatibility with polydimethylsiloxane (PDMS) and the minimal number of curing steps required. This resin was specifically designed to not inhibit curing of PDMS, a key requirement for the fabrication of microfluidic devices.

However, optimizing the printer settings for high-resolution prints using the initial resin proved to be challenging. The microfluidic resin's specific properties necessitated precise adjustments in exposure times and layer thicknesses to achieve the desired resolution. This trial-and-error process resulted in significant resin waste and increased the overall time required for printing.

To address these challenges, a commercial resin containing microcrystalline ceramic powders was tested. This resin offered several advantages over the initial choice:

- **Higher Resolution Prints:** The inclusion of microcrystalline ceramic powders improved the resin's ability to capture fine details, resulting in higher resolution prints. This was particularly important for the intricate geometries required in our experimental designs.
- **Easier Optimization:** The commercial resin's properties made it more forgiving with regard to printer settings, simplifying the optimization process. This reduced the time and material waste associated with printing trials.
- **Additional Curing Steps:** Although the new resin required additional heat curing and washing steps, these were manageable within our workflow. Post-printing, the models were subjected to heat curing to enhance their mechanical properties and stability.
- **Surface Treatment:** To eliminate surface chemicals that could inhibit PDMS curing, the printed models were washed with Tween 20 (Sigma-Aldrich, St. Louis, MO). This surfactant effectively removed any residual inhibitors, ensuring a clean surface for PDMS application.

- **Higher Heat Tolerance:** The new resin's higher heat tolerance allowed for quicker PDMS curing in an oven. This sped up the overall fabrication process of devices.
- **Cost Efficiency:** The commercial resin was significantly more cost-effective, with a cost per unit volume that was 10 times less than the previous resin. This reduced material costs substantially, making the overall process more economical.

In summary, the transition to a commercial resin containing microcrystalline ceramic powders significantly improved the printing process. The benefits included higher resolution prints, easier optimization, and better compatibility with PDMS curing protocols. These improvements were instrumental in achieving consistent and high-quality results, ultimately contributing to the success of our experimental models.

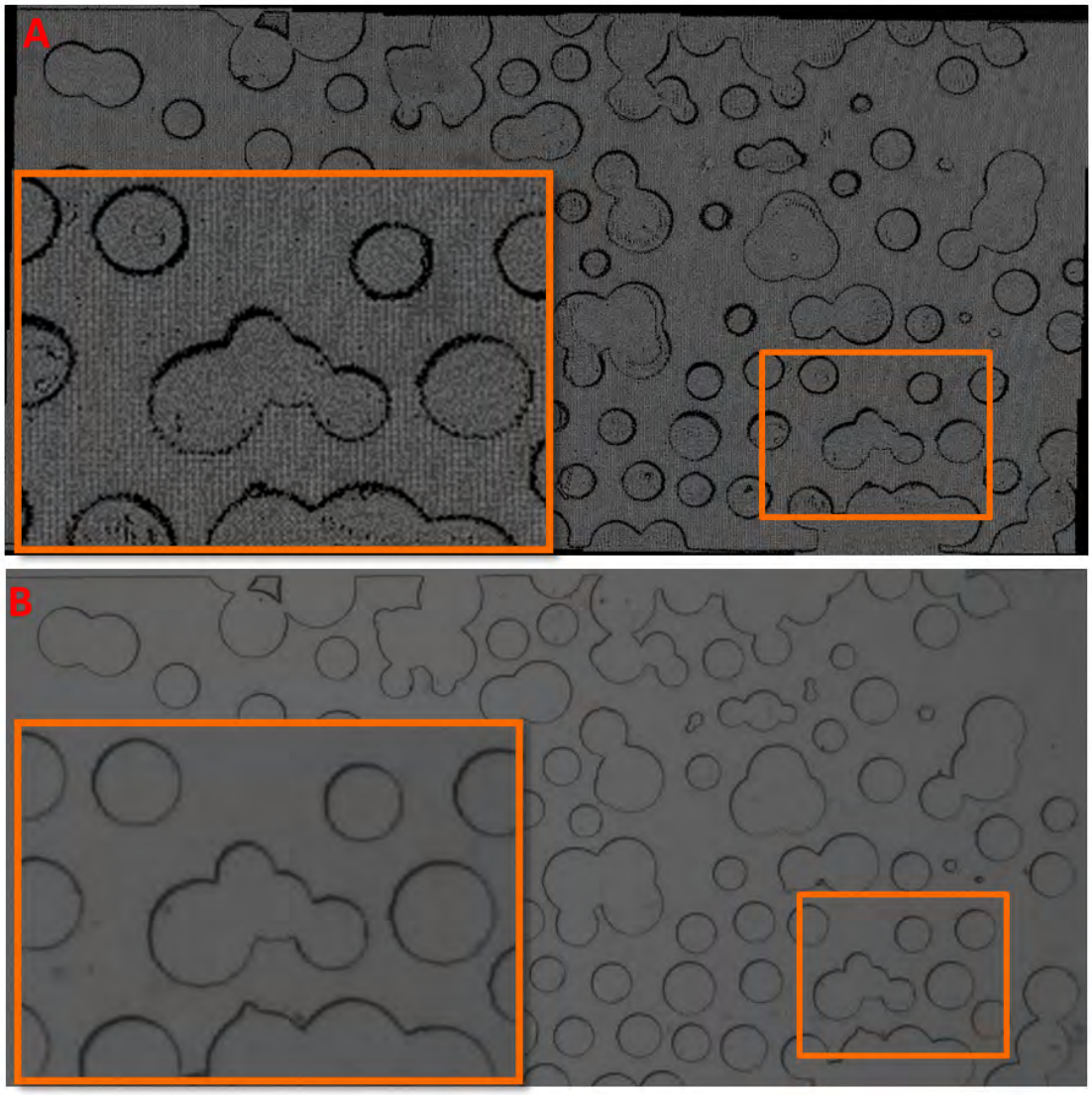

Figure 4.5: Resin Comparison: A) Proprietary Microfluidic Resin from CADworks3D. B) Commercialized microcrystalline ceramic powder based resin. Total Field of View for both images is 13 x 7.4 mm

4.7.6 Printing Profiles

Printing profiles played a crucial role in controlling the settings for each layer, including layer thickness, number of base layers, base curing time, and buffer layers. These settings directly impacted the quality and accuracy of the printed models.

The most critical setting was the curing time. Incorrect curing times could lead to over-curing, which resulted in bleeding and low resolution, or under-curing, which caused deformations and

structural weaknesses. To determine the optimal settings, a systematic approach was employed:

- **Test Cube Method:** A test cube with varying feature sizes was printed to evaluate the effect of different curing times. This allowed for a visual inspection of edge sharpness and resin accumulation.
- **Adjusting Curing Time:** If the test cube's edges appeared too soft or blurred, the curing time was increased incrementally. Conversely, if excess resin accumulated around features, the curing time was decreased. This iterative process continued until the optimal curing time for a 50 µm layer was established.
- **Proportional Adjustment for Other Thicknesses:** Once the ideal curing time for a 50 µm layer was found, curing times for other layer thicknesses were adjusted proportionally. The following method was used to estimate curing time for different thicknesses near 50 µm:

$$\text{New CT} = \text{Original CT} - \left(\frac{\text{Original CT} \times (\text{Original Thickness} - \text{New Thickness})}{2 \times \text{Original Thickness}} \right)$$

For example, if the optimal curing time for a 50 µm layer was 1 second, the initial curing time for a 25 µm layer was estimated as follows:

$$\text{New CT} = 1 \text{ second} - \left(\frac{1 \text{ second} \times (50\mu m - 25\mu m)}{2 \times 50\mu m} \right) = 1 \text{ second} - 0.25 \text{ seconds} = 0.75 \text{ seconds}$$

This formula provided a starting point for further fine-tuning.

- **Base Layers and Curing Times:** The number of base layers and their curing times were critical for establishing a solid foundation for the print. Base layers required longer curing times to ensure strong adhesion to the build plate. Typically, base layers were cured for 5 to 10 times longer than standard layers.
- **Buffer Layers:** Buffer layers acted as a transition between the base layers and the main structure. They had intermediate curing times to gradually reduce the curing intensity, preventing sudden changes that could lead to defects.
- **Layer Thickness:** The chosen layer thickness influenced the print resolution and time. Thinner layers provided higher resolution but increased print time, whereas thicker layers reduced print time at the expense of resolution. The optimal layer thickness was selected based on the specific requirements of the model ranging from 5-100 µm.

In summary, developing optimal printing profiles involved careful calibration of various parameters, especially curing times, to achieve high-resolution, accurate, and defect-free prints. By systematically testing and adjusting these settings, we ensured that the printed models met the desired specifications and quality standards.

4.7.7 Surface Area and Suction

High surface area prints posed unique challenges, particularly in managing the separation process between the build plate and the Teflon sheet. Ensuring efficient peeling from the Teflon sheet was critical to maintaining print integrity and quality.

- **Slower Build Plate Separation:** For high surface area prints, a slower separation speed of the build plate from the Teflon sheet was necessary. Rapid peeling could cause layers to adhere to the Teflon sheet, leading to misprints and potential damage to the sheet itself. By reducing the separation speed, we minimized the risk of layers sticking and ensured a clean detachment.
- **Suction Forces and Trapped Fluid Areas:** Designs with trapped fluid areas could generate suction forces during the separation process. These forces might pull layers off the print, resulting in defects or complete print failure. Implementing a slower and more controlled separation mitigated these risks by allowing trapped air or fluid to release gradually, reducing the suction effect.
- **Teflon Sheet Properties:** The Teflon sheet served as a crucial component due to its nonstick properties. Its low surface energy ensured that cured resin layers adhered to the build plate rather than the Teflon surface. This characteristic was essential for consistent layer formation and successful print completion.
- **Maintenance of the Teflon Sheet:** Maintaining a clean and uniform Teflon sheet was vital for print quality. Any scratches, dents, or contamination on the Teflon surface could transfer to the print, resulting in surface defects and affecting the overall functionality of the device. Regular inspection and replacement of the Teflon sheet were necessary to prevent such issues.
- **Optimizing Design Features:** To further reduce the impact of suction forces, design features were optimized. Incorporating small venting channels or avoiding large flat areas in the design helped to alleviate the suction effect. These adjustments allowed air to flow more freely during the separation process, enhancing print reliability.

- **Monitoring and Adjustments:** Continuous monitoring of the separation process and making real-time adjustments based on observed issues were crucial. Any deviations in the expected behavior were addressed promptly by tweaking separation speeds or modifying design aspects, ensuring consistent print quality.

In conclusion, managing surface area and suction during the printing process required a combination of careful speed adjustments, meticulous maintenance of the Teflon sheet, and thoughtful design optimizations. By addressing these factors, we minimized print defects and ensured the successful production of high-quality, functional models.

4.7.8 Washing and Curing Devices

Post-printing, thorough washing and curing of the printed device were essential to ensure the removal of any uncured resin and to achieve the desired mechanical properties and stability. The washing process removes residual resin, preventing interference with curing and further processing steps, while curing solidifies the material, enhancing its durability and functionality. This multi-step procedure is critical for preparing the device for subsequent experimental use and ensuring high-quality results.

- **Initial Washing with Isopropyl Alcohol (IPA):** Once the device was removed from the build plate, it was subjected to an initial wash using isopropyl alcohol (Amazon Brand, USA). This step involved rinsing the surface of the device with a spray bottle filled with IPA to dislodge and remove any semi-cured resin particulates. The IPA acted as a solvent, efficiently cleaning the surface.
- **Drying and Inspection:** After washing, the device was dried using compressed air to remove any residual IPA and particulates. The device was then inspected under optical magnification to ensure no resin residue remained. This wash-and-dry cycle was repeated until the device was completely clean, ensuring no contaminants interfered with subsequent curing steps.
- **UV Light Curing:** The cleaned device was placed in a UV light chamber for thorough curing. Each side of the device was exposed to UV light for 20 minutes. This step ensured complete polymerization of the resin, enhancing the device's mechanical properties and stability while setting the surface properties.
- **Heat Curing:** Following UV curing, the device underwent heat curing in an oven set to 75 degrees Celsius for a duration of 24 hours or more. This prolonged heat exposure allowed

any residual solvents or uncured resin to either evaporate or rise to the surface, ensuring the internal and external structure of the device was fully cured.

- **Soaking in Tween 20 Solution:** After heat curing, the device was soaked in a solution of water and 0.1% Tween 20. Tween 20, a surfactant, helped in removing any remaining surface residues that could inhibit further PDMS curing. The device was then rinsed thoroughly with deionized (DI) water to remove any surface residues.
- **Final Drying and Preparation:** The device was air-dried and then placed back in the oven for a short duration to ensure complete dryness and readiness for PDMS application. This final drying step was crucial to eliminate any moisture that could interfere with PDMS bonding.

This comprehensive washing and curing process ensured that the printed models were free of any contaminants and fully cured, providing a high-quality, stable foundation for subsequent experimental procedures. The next section will detail the preparation and application of PDMS, further advancing the creation of functional microfluidic devices.

4.8 Fabrication of Device

Poly(dimethylsiloxane) (PDMS) is a silicon-based organic polymer known for its flexibility, optical transparency, and chemical inertness. These properties make it particularly suitable for use in microfluidic devices, which require precise control over fluid flow and robust, biocompatible materials. PDMS's biocompatibility and ease of fabrication further enhance its suitability for applications in biomedical and biochemical research.

In the fabrication of microfluidic devices, PDMS was prepared using a 9:1 ratio of base agent to curing agent. This ratio was selected to achieve a balance between flexibility and mechanical strength, tailored to the desired device thickness and properties influenced by oven temperatures during curing.

The fabrication process encompassed several key steps to ensure high-quality and functional microfluidic devices:

- **Mixing and Degassing:** The base and curing agents were thoroughly mixed to ensure uniform distribution. The mixture was then degassed in a vacuum chamber to eliminate air

bubbles, which could compromise the integrity, optical quality, and performance of the final device.

- **Pouring:** The degassed PDMS mixture was poured into 3D printed molds to form the desired microfluidic structures. The PDMS and molds are placed in the vacuum chamber once again to eliminate any air bubbles.
- **Curing:** The filled molds were placed in an oven at a controlled temperature to cure the PDMS. This step solidified the PDMS, creating a stable and durable structure.
- **Demolding:** Once cured, the PDMS structures were carefully removed from the molds using a sharp. This step required precision to avoid damaging the delicate microfluidic features.
- **Surface Treatment and Bonding:** The PDMS structures were then washed, dried then treated to facilitate bonding to other surfaces, such as glass slides. Plasma treatment was employed to activate the surfaces, enabling strong covalent bonding.

Plasma bonding was utilized to achieve a durable seal between PDMS and glass slides. This process involved exposing both surfaces to oxygen plasma, creating reactive sites that formed strong covalent bonds upon contact. This bonding technique was essential for ensuring the reliability and leak-proof performance of the microfluidic devices.

Finally, heating steps post-bonding were crucial for reinforcing the bond strength and ensuring complete bonding of the PDMS and glass slide. The bonded devices were placed in an oven at 75 degrees Celsius for a duration of 2 hours or more.

In conclusion, the fabrication of PDMS-based microfluidic devices involved a series of meticulous steps, from material preparation and molding to bonding and post-curing treatments. These processes were designed to maximize the functionality, reliability, and performance of the devices for various experimental applications.

Properties of PDMS

Poly(dimethylsiloxane) (PDMS) is a versatile material extensively used in the fabrication of microfluidic devices due to its unique physical and chemical properties. PDMS possesses several key properties that make it ideal for microfluidic applications:

- **Low Surface Energy:** PDMS has a low surface energy, making it hydrophobic and resistant to wetting. This property is advantageous for microfluidic channels where fluid flow control and minimal adhesion of unwanted substances are crucial.
- **Flexibility and Elasticity:** The flexibility of PDMS allows it to be molded into complex shapes. Its low modulus of elasticity means it deforms easily under small stresses, which is beneficial for devices with moving components or where mechanical flexibility is required. Altering the ratio of curing agent adjusts the mechanic flexibility of the final product.
- **Chemical Inertness:** Chemically, PDMS is inert and does not react with most chemicals and biological materials. This makes it suitable for handling a wide range of fluids in microfluidic devices, ensuring compatibility with various solvents, reagents, and biological samples.
- **Biocompatibility:** PDMS is biocompatible, meaning it does not harm living cells and tissues. This is essential for biological and medical applications, where PDMS-based devices can be used for cell culture, drug delivery, and diagnostic assays.
- **Optical Transparency:** PDMS is optically transparent, allowing for easy observation and analysis of the fluids and reactions occurring within the microfluidic channels. This property is particularly useful in applications involving microscopy and optical detection methods.
- **Thermal Stability:** PDMS exhibits good thermal stability, maintaining its properties over a wide range of temperatures. This allows for its use in processes that require heating or cooling without compromising the material's integrity.

Preparation of PDMS

The preparation of PDMS for microfluidic device fabrication involves several steps to ensure the material's optimal performance and integration into the device structure:

- **Mixing:** PDMS is prepared by mixing a base agent with a curing agent, typically in a 10:1 ratio. A 9:1 ratio provides a balance between flexibility and mechanical strength. Thorough mixing is crucial to ensure a homogeneous blend, which affects the uniformity of the final cured product.
- **Degassing:** After mixing, the PDMS mixture is placed in a vacuum chamber to remove trapped air bubbles. Degassing is an essential step as air bubbles can create defects in the microfluidic channels, affecting device performance and reliability. Additionally, this process

ensures optical quality results, which are crucial for applications requiring precise visual observation and analysis.

- **Casting:** The degassed PDMS mixture is then cast onto a mold to form a thick layer. The mold defines the microfluidic structures and channels. Additional degassing is required to remove any additional air bubbles from the PDMS and 3D mold's surface.
- **Curing:** The cast PDMS is cured in an oven at a controlled temperature. Curing solidifies the PDMS, creating a stable and durable structure. The curing time and temperature are optimized based on the desired properties of the final device.
- **Demolding:** Once cured, the PDMS layer is carefully peeled off the mold. This step requires precision to avoid damaging the delicate microstructures. The resulting PDMS piece contains the negative replica of the mold's features.
- **Surface Treatment and Bonding:** To create a microfluidic device, the PDMS layer is bonded to a substrate, typically a glass slide. Surface treatment, such as plasma activation, is performed to enhance bonding. Plasma treatment introduces reactive groups on the PDMS and glass surfaces, enabling strong covalent bonding.
- **Final Curing:** After bonding, the device may undergo additional curing steps to ensure complete polymerization and stabilization of the PDMS. This final curing process enhances the mechanical strength and durability of the device, preparing it for experimental use.

In summary, PDMS is an excellent material for microfluidic device fabrication due to its favorable properties and ease of preparation. The combination of flexibility, chemical inertness, biocompatibility, and optical transparency makes PDMS a preferred choice for a wide range of applications in biomedical and biochemical research.

4.8.1 PDMS Mixing and Curing

Typically, a 10:1 ratio of base agent to curing agent is used to cure PDMS. For these experiments, a 9:1 ratio was used to produce less flexible PDMS devices, resulting in structures that are closer to solid porous materials. This adjustment enhances the structural rigidity of the PDMS, which is crucial for maintaining the integrity of the microfluidic channels under various experimental conditions. Additionally, this ratio promotes curing even in the presence of minor surface defects on the print that might otherwise inhibit the curing process.

Temperature significantly affects the curing time of PDMS. Higher temperatures accelerate the curing process, making it more efficient. At room temperature, PDMS can take several days to fully cure. Extracting it from the mold prematurely can leave a sticky residue, ruining the print. To overcome this, the molds filled with PDMS were placed in an oven to achieve faster curing times and improve overall fabrication efficiency.

Using an Arrhenius plot calculation, based on manufacturer data and empirical observations, it was determined that curing at 75 degrees Celsius results in approximately 2-hour curing times. This temperature-dependent curing process allows for precise control over the final properties of the PDMS devices. By adjusting the temperature, the curing time can be finely tuned to ensure complete polymerization and optimal mechanical properties, which are essential for the functionality and durability of the microfluidic devices.

Table 4.1: Curing Times of PDMS at Various Temperatures

Temp (°C)	20	25	30	35	40	45	50	55	60	65	70
Hours	58.81	41.32	29.37	21.10	15.33	11.25	8.33	6.23	4.69	3.57	2.74

Temp (°C)	75	80	85	90	95	100	105	110	115	120
Hours	2.11	1.64	1.29	1.02	0.81	0.64	0.52	0.42	0.34	0.28

4.8.2 Plasma Bonding to Glass

Once cured, the PDMS was carefully extracted from the 3D print using a scalpel to avoid any damage to the intricate microfluidic structures. The extracted PDMS was then thoroughly washed with isopropyl alcohol (IPA) to remove any residual uncured material or contaminants, ensuring a clean surface for bonding. After washing, the PDMS was air-dried completely.

Similarly, the glass slide, which serves as the substrate for the microfluidic device, was washed with IPA and air-dried to ensure it was free of any dust or oils that could impede bonding.

The bonding process involved using a plasma pen to create oxygen plasma. This plasma treatment modifies the surface of both the PDMS and the glass slide, enhancing their adhesion properties. The plasma pen generates a localized plasma field that activates the surfaces by introducing silanol groups, which increase the surface energy of the PDMS and glass, enabling the formation of strong covalent bonds between them.

- **Surface Activation:** The plasma pen (Plasma Etch Carson City, NV) was moved uniformly

over the surfaces of both the PDMS and the glass slide. The oxygen plasma interacts with the surfaces, creating reactive sites that facilitate the bonding process.

- **Alignment and Bonding:** After plasma treatment, the PDMS was carefully aligned with the glass slide to ensure proper channel configuration and prevent misalignment. The activated surfaces were then brought into contact, and pressure was applied to ensure a uniform bond without trapping air bubbles.
- **Bonding Integrity:** Proper bonding is critical to avoid trapping fluid or altering pressure within the microfluidic device. Inadequate bonding can lead to leaks between the PDMS and the glass slide, compromising the device's functionality. Therefore, ensuring a strong and uniform bond is essential for the reliability and performance of the microfluidic device.

Plasma bonding significantly increases the surface energy of both PDMS and glass, allowing for a strong covalent bond to form between them. This process not only ensures a robust seal but also maintains the transparency and optical clarity of the device, which is crucial for many microfluidic applications.

In conclusion, plasma bonding is a vital step in the fabrication of PDMS-based microfluidic devices. By utilizing oxygen plasma to activate the surfaces, a strong and reliable bond is achieved, ensuring the device's structural integrity and functionality. This method is particularly effective in preventing leaks and maintaining the precise control of fluid flow within the microfluidic channels.

4.8.3 Heating After Bonding

After plasma bonding, the device was placed in the oven to ensure proper bonding. The PDMS surface is less hydrophobic immediately after plasma treatment but regains its hydrophobic properties after a few hours. This post-bonding heating step is essential for reinforcing the bond between the PDMS and glass, ensuring it is robust and long-lasting. Proper bonding is crucial for maintaining the device's performance over extended periods and preventing leaks or detachment during use.

The heating process involves placing the bonded device in an oven at a controlled temperature. This step serves multiple purposes:

- **Enhanced Bond Strength:** Heating facilitates the formation of stronger covalent bonds between the PDMS and glass, enhancing the overall bond strength. This ensures that the bond can withstand various stresses and strains during the device's operation.

- **Stabilization of Surface Properties:** Post-bonding heating helps stabilize the surface properties of PDMS. Immediately after plasma treatment, the PDMS surface is less hydrophobic, which aids in bonding. However, over time, the surface gradually regains its hydrophobic nature. Heating accelerates this stabilization process, ensuring the device's surface properties are consistent and reliable.
- **Prevention of Delamination:** Proper heating after bonding minimizes the risk of delamination, where the PDMS may separate from the glass over time. This is particularly important for applications involving fluid flow, where pressure changes could otherwise compromise the bond.

Typically, the heating process involves placing the bonded device in an oven at a temperature around 75 degrees Celsius for 1-2 hours. This temperature and duration are sufficient to reinforce the bond without causing any damage to the PDMS or the microfluidic structures.

These detailed steps ensure the successful preparation and application of PDMS in our experiments, providing a robust foundation for the creation of functional microfluidic devices. The next section will discuss the application of Aquapel to create hydrophobic surfaces in these devices.

4.9 Application of Aquapel

The application of Aquapel for creating hydrophobic surfaces is crucial in our experiments, particularly for droplet creation and pressure management. Aquapel, a commercial product designed to increase the hydrophobicity of glass windshields, is employed to coat the inside of the microfluidic device. It consists of petroleum distillates with proprietary additives that enhance adhesion to surfaces, making it an effective solution for our needs.

The process for applying Aquapel to the microfluidic device involves several precise steps:

- **Filling the Device:** The device is filled with Aquapel and allowed to rest for 10 minutes. This duration ensures that the Aquapel adequately coats all internal surfaces, enhancing their hydrophobic properties.
- **Flushing the Device:** After the resting period, the device is flushed with air to remove excess Aquapel. This is followed by flushing with HFE (Hydrofluoroether) to ensure any

remaining Aquapel is removed. Finally, another air flush is performed to dry the internal surfaces.

- **Drying:** The device is then placed in an oven to dry for 30 minutes. This drying step is crucial to ensure that any residual fluids are completely evaporated, leaving behind a uniform hydrophobic coating.
- **Timing of Use:** It is essential to begin the experiment within 30 minutes of completing the drying process. Aquapel can precipitate when exposed to air over extended periods, which could diminish its effectiveness. Therefore, timing is critical to maintain the hydrophobic properties of the coated surfaces.

The application of Aquapel significantly enhances the hydrophobicity of both the glass slide and the surrounding PDMS. This increased hydrophobicity is vital for creating the pressure collar required for uniform droplet generation. When water is introduced through the inlet, the enhanced hydrophobicity ensures the formation of a stable pressure collar, facilitating consistent and reliable droplet production.

These steps ensure that the device is adequately prepared for experiments, leveraging Aquapel's properties to achieve the desired hydrophobic conditions. Proper application of Aquapel is essential for maintaining the performance and reliability of the microfluidic device, particularly in applications involving precise fluid control and droplet generation.

In conclusion, the careful application of Aquapel prepares the microfluidic device for optimal performance, providing the necessary hydrophobic conditions for successful experimental outcomes. The next section will discuss the preparation and setting up of the experimental devices, ensuring readiness for precise and reliable data collection.

4.10 Experiments

The setup for our experiments was carefully designed to ensure precise and reliable data collection, focusing on the components and processes essential for studying emulsion transport in porous media. Each component of the experimental setup was selected and configured to maintain consistency and accuracy throughout the experiments, from the pressure transducer to the imaging systems.

To achieve our objectives, the following aspects were critically evaluated and optimized:

- **Pressure Measurement and Control:** Accurate pressure measurement and control were paramount for maintaining consistent fluid dynamics within the microfluidic device. The pressure transducer, connected between the continuous fluid inlet and the microfluidic device, provided real-time data essential for adjusting and maintaining the desired experimental conditions.
- **Fluid Delivery System:** The tubing connection setup facilitated the seamless flow of fluids into the device, preventing leaks and maintaining system integrity. This ensured that the water, HFE surfactant, and other fluids were delivered precisely to the designated inlets and outlets.
- **Fluid Preparation:** Proper preparation of fluids, including FSH oil, HFE, and dyed water, was crucial for achieving reliable and reproducible results. Each fluid was prepared to specific concentrations and properties to ensure optimal performance in the experiments.
- **Droplet Generation:** The pressure pulse system, controlled by an Arduino board, allowed precise regulation of pressure pulses, facilitating consistent droplet formation. This setup was key to studying the dynamics of droplet creation and movement within the microfluidic device.
- **Imaging and Analysis:** High-quality imaging was essential for capturing the behavior of emulsions within the device. The FASTEC monochrome high-speed camera and the Zeiss Axio Zoom.V16 microscope were configured to provide detailed, high-contrast images, enabling accurate analysis of the experimental results.
- **Microscope Configuration:** The microscope setup, including the motorized 3D stage and appropriate objectives, ensured precise orientation and focusing. This allowed for detailed observation of the emulsion dynamics and facilitated the collection of high-resolution images necessary for subsequent analysis.

These detailed steps ensured the successful preparation and execution of experiments, providing a robust foundation for studying emulsion transport in porous media. Each component was carefully chosen and integrated to maintain the integrity and reliability of the experimental setup, ultimately contributing to the generation of precise and reproducible data.

The following subsections will delve into the specifics of each component, detailing the procedures and configurations used to achieve the desired experimental outcomes. This comprehensive approach ensures that all aspects of the experimental setup are thoroughly documented and optimized for studying emulsion transport.

4.10.1 Pressure Transducer

The pressure transducer was a critical component in our experimental setup, positioned between the continuous fluid inlet and the microfluidic device. This precise placement was essential for accurate pressure measurement and control, ensuring the reliability and consistency of fluid dynamics within the device. To integrate the pressure transducer into the setup, the following steps were undertaken:

- **Calibration:** The transducer was calibrated before each experiment to ensure accurate readings. This involved setting a baseline pressure and verifying the transducer's response to constant pressure.
- **Connection:** The transducer was securely connected between the continuous fluid inlet and the microfluidic device. Care was taken to ensure airtight connections, preventing any leaks that could affect the pressure readings and the overall experiment.
- **Fluid Filling:** The transducer was filled with the HFE + surfactant fluid mixture. This step was performed carefully to avoid introducing air bubbles, which could interfere with pressure measurements.
- **Monitoring:** During the experiments, the transducer continuously monitored the pressure within the system. The data collected was used to analyze how pressure changes with emulsions transport and dynamics.

By utilizing a pressure transducer in this manner, we ensured that the microfluidic device operated under stable and controlled conditions. This precision was critical for the success of our experiments, allowing us to study emulsion transport and other fluid dynamics with high accuracy and reliability.

In conclusion, the pressure transducer was an indispensable component of our experimental setup. Its role in maintaining consistent fluid dynamics and providing accurate pressure measurements was crucial for the integrity and reproducibility of our experimental results.

4.10.2 Tubing Connection

The connection of microfluidic tubing to the device is a critical aspect of the experimental setup, requiring precision and reliability to ensure seamless fluid flow and prevent leaks. In our experiments, we utilized 3D-printed pillars to create holes for tubing connections, addressing common issues associated with traditional methods such as biopsy punches.

Traditionally, biopsy punches are used to create holes in PDMS devices for tubing connections. However, this method often presents several challenges:

- **Risk of Damage:** Biopsy punches can cause tearing or ripping of the PDMS, particularly if the punch size is not perfectly matched to the tubing size or the punch is dulled.
- **Imprecise Sizing:** Inconsistent punch sizes can lead to holes that are either too loose or too tight, resulting in leaks or difficulties in inserting the tubing securely.

To overcome these challenges, we incorporated 3D-printed pillars into our device design. These pillars were specifically designed and printed as part of the device structure, providing several advantages:

- **Precision and Consistency:** The 3D-printed pillars ensured precise and consistent hole sizes, tailored to the exact dimensions required for the microfluidic tubing. This precision minimized the risk of leaks and made the insertion of tubing straightforward and secure.
- **Ease of Integration:** The holes created by the pillars facilitated easy connection of the microfluidic tubing to the device. This design eliminated the need for additional manual punching, reducing the potential for human error and material damage.
- **Enhanced Durability:** The integrated pillars provided a more durable and stable connection point for the tubing, improving the overall robustness of the device.

The specific tubing connections in our setup included:

- **Inner Inlet:** The water column was connected to the inner inlet, ensuring controlled delivery of the inner fluid for droplet formation.
- **Outer Inlet:** HFE surfactant fluid was connected to the outer inlet. This fluid acted as the continuous phase, critical for maintaining stable fluid dynamics and droplet formation.
- **Outlet:** The outlet was connected to an empty reservoir for waste collection. This setup ensured that the spent fluids were safely and efficiently removed from the system, preventing any backflow or contamination.
- **Emergency Outlet:** An additional outlet was positioned prior to the main porous media chamber. This outlet was typically pinched closed but could be opened to a waste reservoir

in case of droplet formation failure. This emergency exit allowed for the removal of failed emulsions before they reached the porous media, ensuring that only properly formed droplets entered the main experimental area.

By utilizing 3D-printed pillars for tubing connections, we ensured a seamless flow of fluids into the device, maintaining system integrity and reliability. This design innovation not only improved the ease of setup but also enhanced the overall performance of the microfluidic device by providing consistent and leak-free connections.

In conclusion, the integration of 3D-printed pillars for tubing connections addressed common issues associated with traditional methods, offering a precise, reliable, and durable solution for our microfluidic experiments.

4.10.3 Preparing Fluids

The preparation of fluids was a crucial step in ensuring the success of our experiments. Each fluid used in the microfluidic device had specific roles and properties that contributed to the overall functionality and accuracy of the experimental setup.

FSH Oil: FSH oil, a fluorinated oil, served as a surfactant in our experiments. It was mixed overnight with HFE (Hydrofluoroether) to form the outer fluid at 5% by weight. This mixture was essential for consistent droplet formation by decreasing interfacial tension. Surfactants, like FSH oil, play a critical role in stabilizing emulsions by reducing the surface tension between two immiscible liquids, such as oil and water. The dual nature of surfactants, with hydrophobic and hydrophilic components, allows them to spread evenly at the interface and stabilize the mixture. Surfactants are widely used in various industries, including cleaning agents, personal care products, and oil extraction, due to their ability to alter surface properties and enhance mixing and stability.

HFE: HFE-7500, an engineering fluid, was used as the continuous fluid in the device. It flowed at a controlled rate of 5 ml/hr using a syringe pump. Maintaining a steady flow rate was vital for stable fluid dynamics and ensuring the accuracy of experimental results. HFE-7500, a hydrofluoroether fluid, is known for its low global warming potential and high thermal stability, making it suitable for applications requiring high performance with minimal environmental impact. Additionally, HFE-7500 is non-toxic and non-flammable, providing a safer alternative compared to other industrial fluids. Its properties make it an ideal choice for various industrial processes, such as heat transfer and fluid power systems, where reliable and safe performance is paramount.

Water + Various Dyes: Water served as the inner fluid for droplet formation, controlled by a pressure pulse Arduino device. To enhance contrast for imaging, dyes such as food dye and Fluorescein sodium salt were added to the water. These dyes allowed for better visualization and tracking of droplets during experiments, facilitating accurate data collection and analysis. Food dye, which contains Propylene glycol, was prepared by boiling at 300°C to remove the Propylene glycol, ensuring appropriate interfacial tension for droplet formation. The use of dyes was particularly important for capturing detailed images of the droplet dynamics within the microfluidic channels, enabling precise observation and measurement of the experimental outcomes.

Preparation Process

The preparation of each fluid involved specific steps to ensure their proper function in the experiments:

- **Mixing FSH Oil with HFE:** The FSH oil was mixed with HFE-7500 overnight to ensure thorough incorporation and uniform distribution of the surfactant. This prolonged mixing period was essential to achieve the desired interfacial tension reduction, critical for stable droplet formation.
- **Preparing HFE-7500:** HFE-7500 was prepared and stored in a clean, sealed container to prevent contamination. Before each experiment, the fluid was loaded into a syringe pump ensuring consistent experimental conditions.
- **Dyeing Water:** Water was mixed with the appropriate dyes to achieve the required concentration for imaging. When food dye was used, it was first boiled at 300°C to remove Propylene glycol, ensuring appropriate interfacial tension for droplet formation. This preparation step ensured clear and consistent visualization of the droplets during the experiments.

By diligently preparing each fluid, we ensured that the microfluidic device operated under optimal conditions, facilitating accurate and reliable data collection. These preparation steps were crucial for maintaining the integrity and consistency of the experimental setup, ultimately contributing to the success of our studies on emulsion transport in porous media.

4.10.4 Pressure Pulse (Arduino)

The precise control of pressure pulses was essential for achieving consistent and reproducible droplet formation in our microfluidic experiments. To achieve this, we utilized an Arduino board connected to a solenoid valve, which provided an efficient and customizable means of regulating pressure pulses.

System Components and Setup:

- **Arduino Board:** The Arduino board served as the central controller for the pressure pulse system. It was programmed to manage the timing and duration of the solenoid valve's operation, ensuring precise control over the pressure pulses.
- **Solenoid Valve:** The solenoid valve was responsible for regulating the flow of the pressurized fluid. Its opening and closing times were critical for generating the pressure pulses needed for droplet formation.
- **Control Mechanisms:** The system included a knob to adjust the valve's opening time and a button to trigger the pressure pulse. These manual controls allowed for real-time adjustments during the experiments, providing flexibility in managing the droplet generation process.

Operational Procedure:

- **Pressure Regulation:** The system was calibrated to regulate the pressure to 25 psi. This pressure level was chosen based on preliminary experiments to ensure optimal droplet formation. The water column was balanced to stop the flow at the device inlet, allowing controlled flow only when additional pressure was applied.
- **Triggering Pressure Pulses:** The operator could trigger pressure pulses by pressing the button, which activated the solenoid valve according to the preset opening time. This action allowed a controlled burst of pressure to be delivered to the fluid inlet, facilitating the formation of droplets.
- **Adjusting Pulse Duration:** The knob allowed fine-tuning of the valve's opening time, providing precise control over the duration of each pressure pulse. This adjustability was crucial for optimizing the size and consistency of the droplets produced. A single pulse can produce a single droplet to tens of droplets of uniform size depending on the opening time.

Benefits of the Arduino-Controlled System:

- **Precision:** The Arduino-based system offered high precision in controlling the timing and duration of pressure pulses, which is essential for consistent droplet formation.
- **Reproducibility:** By standardizing the pressure pulse parameters, the system ensured reproducible results across multiple experiments, enhancing the reliability of the data collected.
- **Flexibility:** The ability to manually adjust the pressure pulse parameters in real-time allowed for flexibility in responding to varying experimental conditions, facilitating the optimization of droplet generation.

In conclusion, the Arduino-controlled pressure pulse system was a key component in our experimental setup. Its precise control over pressure pulses enabled accurate and reproducible droplet formation, which was critical for studying emulsion transport in porous media. This setup not only enhanced the reliability of our experiments but also provided the flexibility needed to adapt to different experimental requirements.

4.10.5 Camera Settings

High-quality imaging was essential for accurately capturing the behavior of emulsions within the microfluidic device. For this purpose, a FASTEC monochrome high-speed camera was employed. Optimizing the camera settings was critical to ensure proper signal capture, contrast, and data processing, facilitating precise analysis of the experimental results.

Camera Configuration:

- **Frame Rate (FPS):** A lower frame rate was selected due to the slow movement of emulsions within the device. This choice minimized the amount of data to process while still capturing sufficient temporal resolution to analyze the droplet dynamics and acquire positional updates. Typically, frame rates were set to around 50-100 FPS, which balanced the need for temporal resolution with manageable data file sizes.
- **Exposure Time:** Higher exposure times were used to improve image contrast. However, a balance had to be struck to avoid blurred edges caused by motion within the frame. Through careful calibration, the exposure time was optimized to enhance the visibility of droplets and their interfaces without compromising image sharpness depending on the velocities of the emulsions.

- **Resolution and Bit Depth:** The camera's resolution and bit depth settings were configured to maximize image clarity and detail. Higher resolution allowed for detailed observation of the microfluidic channels and droplets, while a bit depth ensured a robust dynamic range, capturing subtle variations in light intensity.

Region of Interest (ROI):

- **Defining the ROI:** The region of interest (ROI) was carefully defined to capture only the relevant area within the microfluidic device. This focus on the area of interest helped in reducing data file sizes and improved processing speeds.
- **Adjusting the ROI:** During the setup, the ROI was adjusted to align perfectly with the microfluidic channels where emulsion dynamics were to be observed. This ensured that all significant interactions were captured, and extraneous areas were excluded from the analysis.

Additional Optimizations:

- **Lighting Conditions:** Proper lighting was crucial for achieving high-quality images. The microfluidic device was illuminated using a collimated RGB LED backlight, which provided uniform illumination across the field of view, reducing shadows and highlights that could obscure details.
- **Calibration:** Regular calibration of the camera system was performed to ensure consistency in imaging quality. This involved checking the alignment, focus, and exposure settings before each set of experiments.

In conclusion, the thorough optimization of camera settings was vital for obtaining high-quality images required for analyzing emulsion behavior in the microfluidic device. The chosen settings ensured a balance between data processing efficiency and image clarity, enabling precise and reliable experimental observations.

4.10.6 Microscope Setup

The microscope setup was a critical component of our experimental system, designed to capture high-quality images of the intricate dynamics within the microfluidic device. The use of advanced

microscopy techniques and precise control mechanisms ensured that we could observe and analyze the behavior of emulsions in detail.

Microscope Configuration:

- **Zeiss Axio Zoom.V16 Microscope:** This widefield optical microscope provided a large field of view without distortion, making it ideal for capturing the entire area of interest within the microfluidic device. Equipped with a PlanApo 0.5x/0.125 WD 114mm objective, the microscope delivered high-resolution images with excellent clarity and detail.
- **Motorized 3D Stage:** The microscope was mounted on a motorized 3D stage, which allowed for precise orientation and focusing. This stage enabled fine adjustments in the X, Y, and Z axes, optimizing the positioning of the microfluidic device for imaging. The motorized stage was essential for maintaining consistent focus and alignment across multiple experiments.

By following these detailed procedures, the experimental setup ensured accurate and reproducible results, providing a solid foundation for studying emulsion transport in porous media. The combination of advanced microscopy, precise stage control, and high-speed imaging allowed for comprehensive analysis of the emulsion dynamics, contributing significantly to the reliability and validity of our experimental findings.

The next section will discuss data processing techniques, including image analysis and tracking algorithms, to interpret the collected data effectively.

4.11 Data Processing and Analysis

Data processing involved sophisticated image processing techniques, which were essential for analyzing the collected data accurately and reliably. These techniques included background subtraction, image stabilization, local contrast enhancement, adaptive binarization in Matlab, and object detection algorithms. Additionally, the development of a tracking algorithm, cost matrix, and visualization tools, along with GUI implementation and data structure conversions, ensured a comprehensive and replicable methodology.

This structured approach aligns with the rigorous standards required for scholarly research in the field of emulsion transport in porous media. The subsequent sections will delve into the specifics of each technique and its implementation.

4.12 Image Processing Techniques

The image processing techniques employed in our study are critical for analyzing the collected data accurately. These methods are essential for transforming raw experimental data into meaningful insights about emulsion transport in porous media. This section discusses the various techniques and software tools used, including image stabilization, contrast enhancement, binarization, object detection, and particle image velocimetry (PIV).

ImageJ and Fiji: ImageJ is an open-source, cross-platform software for scientific image analysis, written in Java. It provides tools for image processing, measurement, and data analysis. Fiji, an extended version of ImageJ, includes additional plugins and libraries for enhanced functionality like 3D visualization and registration, tailored for biological image analysis. We used ImageJ for initial visualization and testing, followed by advanced processing in Matlab.

Particle Image Velocimetry (PIV): PIV is a non-intrusive fluid dynamics measurement technique used to determine fluid flow velocity. It involves introducing tracer particles into a fluid sample and illuminating the sample with a laser light sheet. Images of the illuminated tracer particles are captured, and the displacement of the particles between two consecutive frames is analyzed to determine the fluid flow velocity. In our study, PIV was used with tracer particles rather than emulsions to better characterize flow within the device when void of emulsions as a comparative measure [79].

PIV Algorithm Steps

Computationally, PIV algorithms involve the following steps:

- **Image Acquisition**: Sequential images of the illuminated tracer particles are captured using a high-speed camera.
- **Image Pre-processing**: The images are pre-processed to improve their quality, such as by correcting for image distortion, noise reduction, and background subtraction.
- **Image Correlation**: The displacement of the tracer particles between two consecutive images is determined using image correlation techniques, such as cross-correlation or phase-correlation.

- **Velocity Calculation**: The particle displacement is converted into fluid flow velocity using the known properties of the fluid, the tracer particles, and the imaging system.
- **Data Post-processing**: The velocity data obtained from PIV is often post-processed to correct for errors and to improve its accuracy, such as by removing false or erroneous vectors and smoothing the velocity field.

PIV algorithms are computationally intensive and require sophisticated image analysis software to extract accurate velocity information from the images of the tracer particles. The PIV algorithm is a key component of the PIV measurement technique and has been continuously developed and improved over the years to provide more accurate and reliable velocity measurements. In this work, Thielicke's PIVlab module from Matlab was utilized when PIV calculations where required.

4.12.1 Flow Visualization and PIV Analysis

Figure 4.6 illustrates the flow of florescent particles through a small section of porous media, captured with different camera settings. The top row (A-D) presents images with the focal plane closer to the glass slide, while the bottom row (E-H) shows images with the focal plane in the middle of the glass slide and PDMS roof. Each column represents a different exposure time, ranging from 2.5 ms to 10 ms.

Particles near the boundaries mix with higher flow particles in the middle of the channel, causing complications in PIV analysis. Faster-moving smaller particles require shorter exposure times to prevent blurring, but they produce lower signals. In contrast, larger, slower clumps provide stronger signals but are more affected by longer exposure times. A balance is necessary between focal plane placement and exposure time to capture the dynamics accurately.

Panel A (2.5 ms) and E (2.5 ms) demonstrate shorter exposure, revealing faster particles as discrete points, but some particles blink in and out of view due to signal noise. Panels B (5 ms) and F (5 ms) show a balance where both slow and fast particles are visible, although some faster particles start to blur. Panels C (7.5 ms) and G (7.5 ms) illustrate increasing exposure, where blurring of faster particles becomes more evident. Panels D (10 ms) and H (10 ms) show the longest exposure, where fast particles are significantly blurred into lines, complicating PIV grouping and averaging velocities of slow and fast particles.

This analysis highlights the importance of optimizing focal plane placement and exposure time to accurately capture particle dynamics and improve PIV results. Additionally, more comprehensive

PIVs were done using confocal microscopy to achieve more consistent and valid results.

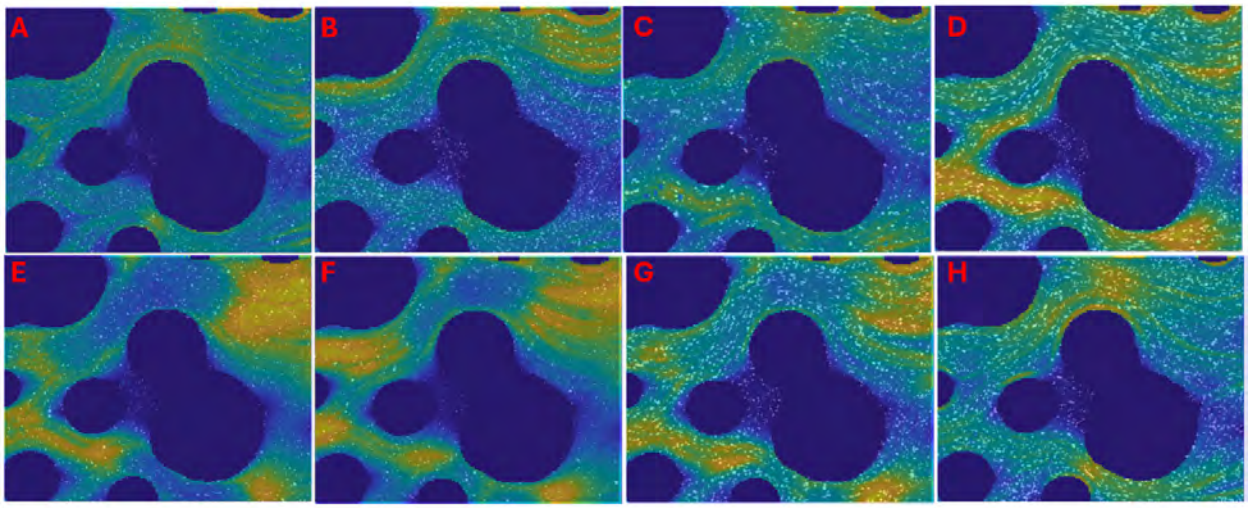

Figure 4.6: Particle flow visualization with PIV results overlay. Top row (A-D): focal plane closer to glass slide. Bottom row (E-H): focal plane in the middle of the glass slide and PDMS roof. Columns represent different exposure times: (A, E) 2.5 ms, (B, F) 5 ms, (C, G) 7.5 ms, and (D, H) 10 ms. The images illustrate the challenges of balancing exposure time and focal plane placement for accurate PIV analysis. Field of View for each is 1mm x 1 mm.

Once adequate parameters are established to capture Particle Image Velocimetry (PIV), a complete device can be characterized by capturing tiles of the entire device. An autocorrelation algorithm was developed, which extracts the top center portion of an image and identifies the highest correlated position for the tile above, recording the coordinates. This process is repeated for each column of tiles. Subsequently, the stitched columns undergo similar processing, using the middle right of the image to determine the highest correlation and the most accurate match. This procedure yields the relative coordinates of each tile, enabling the integration of their respective PIV results. A weighted matrix is employed to combine these results, assigning greater weight to the center of the data while reducing the weight at the corners to account for the edge effects typically observed in PIV. The final results are illustrated in Fig. 4.7.

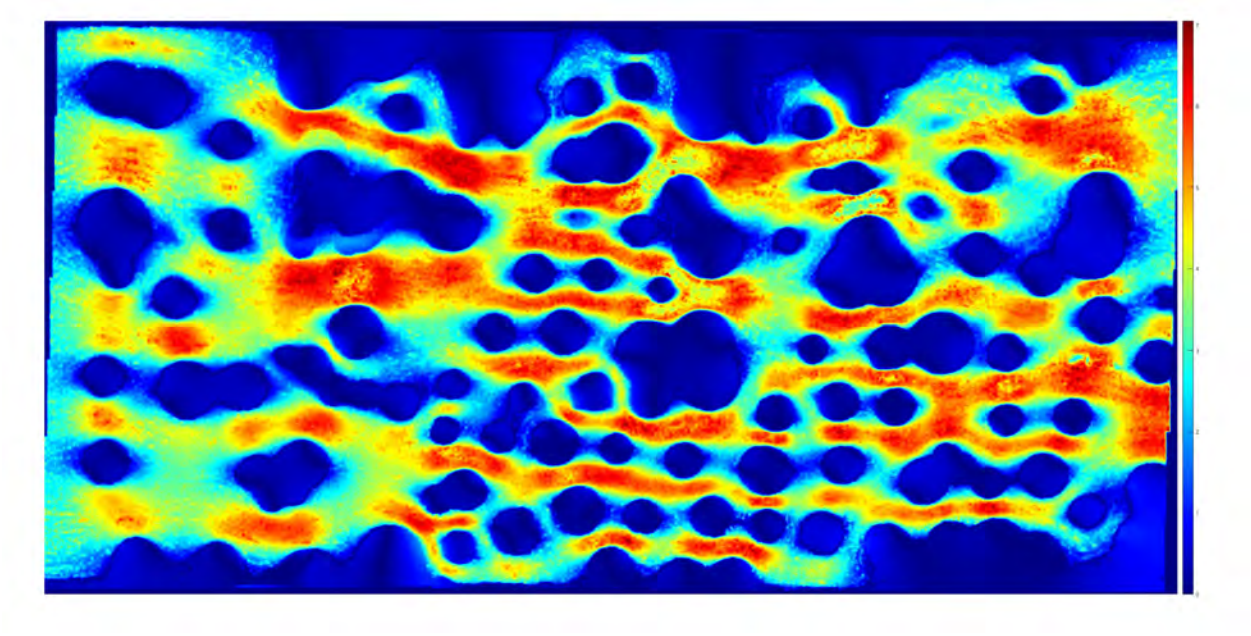

Figure 4.7: PIV Characterization of a whole device using weighted stitching of 60 tiles. Field of View 7.4 x 13 mm

4.13 Image Pre-Processing

4.13.1 Background Subtraction and Stabilization

Background subtraction and stabilization are crucial steps in our image processing workflow, designed to enhance the clarity and accuracy of the captured data. These techniques help isolate the emulsion droplets from the background, reducing noise and improving the reliability of subsequent analyses.

Stabilization Process: Before performing background subtraction, a stabilization process is undertaken to address any potential vibrations or movements during the experiment. The following steps outline the stabilization method:

- **Selection of a Reference Region:** A small, undisturbed region within the microfluidic device is selected. This region serves as a reference point for the stabilization process.
- **Autocorrelation:** Autocorrelation techniques are applied to the reference region. This involves comparing the structure within the reference region of the background image to each frame of the experiment. By calculating the degree of similarity, the images are aligned such that the reference structure remains in the same position across all frames.

- **Image Shifting:** Based on the autocorrelation results, each frame is shifted appropriately to compensate for any detected movement. This alignment reduces the impact of vibrations and ensures that the captured data is consistent and stable over time.

Background Subtraction: Once stabilization is complete, background subtraction is performed to isolate the droplets from the background. The steps involved in background subtraction are as follows:

- **Capture of Background Image:** An image of the microfluidic device is captured prior to the introduction of any droplets. This background image represents the static components of the device without any experimental activity.
- **Subtraction Process:** The background image is subtracted from each stabilized frame of the experiment. This process removes the static elements of the device, highlighting only the dynamic components, such as the moving emulsion droplets.
- **Enhancement of Dynamic Features:** By subtracting the background, the resulting images primarily display the changes and movements within the device. This enhances the visibility of the droplets and other relevant features, facilitating more accurate detection and analysis through increased contrast.

Benefits of Stabilization and Background Subtraction:

- **Signal Enhancement:** These techniques help enhance the signal by minimizing interference from static elements and background artifacts, providing clearer and higher contrast images of the emulsion dynamics.
- **Improved Accuracy:** Stabilized and background-subtracted images allow for more accurate detection of droplets and their movements, improving the reliability of positional measurements and analyses.
- **Consistency Across Frames:** Ensuring that the reference region remains in the same position across all frames enhances the consistency of the data, making it easier to track changes and detect patterns over time.

In conclusion, the processes of background subtraction and stabilization are fundamental to preparing the captured images for detailed analysis. By removing static elements and compensating for

vibrations, these techniques ensure that the focus remains on the dynamic features of the experiment, thereby enhancing the quality and accuracy of the data collected.

Code Breakdown

This will breakdown the code responsible for image stabilization and background subtraction.

```
function processImages(imageFolder, outputFolder, backgroundModel, stabilizationRect, deviceCropRect, s
    % Define Max_shift value
    Max_shift = 15;
    tifFiles = dir(fullfile(imageFolder, '*.tif'));
    % Parallel processing of frames
    parfor idx = 1:length(tifFiles)
        frame = imread(fullfile(imageFolder, tifFiles(idx).name));
```

The function begins by setting a maximum shift value, Maxshift, to control how much each frame can be adjusted. It then gathers all the TIFF files from the specified image folder. To boost performance, the frames are processed in parallel using parfor. Each frame is individually read from the folder.

```
        % Extract a region around the ROI from the frame from stabilization ROI
        yStart = max(1, round(stabilizationRect(2) - Max_shift));
        yEnd = min(size(frame, 1), round(stabilizationRect(2)
                        + stabilizationRect(4) + 2 * Max_shift));
        xStart = max(1, round(stabilizationRect(1) - Max_shift));
        xEnd = min(size(frame, 2), round(stabilizationRect(1)
                        + stabilizationRect(3) + 2 * Max_shift));
        frameROI = frame(yStart:yEnd, xStart:xEnd);
```

A region around the stabilization ROI is extracted from each frame. This region is expanded by Maxshift to allow for alignment adjustments.

```
        bestShift = [0, 0];
        minSSD = inf;

        for y = 1:2*Max_shift
```

```
            for x = 1:2*Max_shift
                currentROI = frameROI(y:y+size(stabilizationRoi,1)-1,
                                      x:x+size(stabilizationRoi,2)-1);
                ssd = sum((double(currentROI) - double(stabilizationRoi)).^2, 'all');
                if ssd < minSSD
                    minSSD = ssd;
                    bestShift = [y, x];
                end
            end
        end
```

A nested loop iterates over possible shifts within the range of Maxshift to find the best alignment. The sum of squared differences (SSD) between the current ROI and the reference ROI is calculated. The shift that minimizes the SSD is selected as the best shift.

```
        yOffset = bestShift(1) - Max_shift;
        xOffset = bestShift(2) - Max_shift;
        % Shift the frame based on the computed offset
        shiftedFrame = circshift(frame, [-yOffset, -xOffset]);
```

The best shift is applied to the frame using circshift, aligning the frame with the reference region.

```
        % Convert to double for further operations
        shiftedFrame = double(shiftedFrame);  % Normalize to [0, 1]

        % Subtract the background model
        diffImage = shiftedFrame - double(backgroundModel);

        rescaled = (diffImage - min(diffImage(:))) / (max(diffImage(:)) - min(diffImage(:)));
```

The shifted frame is converted to double precision for numerical operations. The background model is subtracted from the shifted frames. The resulting difference image is rescaled to the range [0, 1] and then converted to an 8-bit unsigned integer format for further processing.

```
        % Convert the rescaled image to uint8 range [0, 255]
        finalImageUint8 = uint8(255 * rescaled);

```

```
        % Use imcrop with deviceCropRect to crop the final image
        croppedFinalImage = imcrop(finalImageUint8, deviceCropRect);

        % Save the resulting image
        imwrite(croppedFinalImage, fullfile(outputFolder,
                            [tifFiles[idx).name]), 'TIFF', 'Compression', 'lzw');
    end
end
```

The final image is cropped to the region of interest specified by deviceCropRec and saved to the output folder in TIFF format with LZW compression. This ensures that the processed images are correctly aligned and focus on the relevant regions for further analysis.

4.13.2 Local Contrast Enhancement

In low contrast experiments where droplets blend with the background, Contrast Limited Adaptive Histogram Equalization (CLAHE) is used to enhance local contrast. The process is as follows:

1. **Tile Division:** The image is divided into small, non-overlapping tiles.
2. **Local Histogram Equalization:** Histogram equalization is applied within each tile to redistribute intensity values.
3. **Contrast Limiting:** To prevent noise amplification, the histogram is clipped at a specified limit before redistribution.
4. **Interpolation:** Enhanced tiles are seamlessly combined using bilinear interpolation to avoid artificial boundaries.

This method improves the visibility of droplets against the background, enhancing detection accuracy. In our experiments, adjusting parameters like clip limit and tile size allowed for optimal contrast enhancement without introducing noise. CLAHE's ability to adapt to varying conditions makes it a powerful tool for improving detection accuracy in low contrast scenarios. This tool is an option when experimental images have low contrast.

4.13.3 Adaptive Binarization (Matlab)

Adaptive binarization in Matlab, performed using the imbinarize function with the 'adaptive' method, converts grayscale images to binary images by adjusting the threshold for each pixel based on local image statistics. This method improves detection accuracy in varying lighting conditions by considering local contrast variations. The process is enhanced with a median filter to eliminate scattered, isolated signals that are not emulsions, ensuring a clearer distinction of relevant features in the image.

4.14 Object Detection: Circle Hough Transform

The primary method utilizes a circle Hough transform, effective when droplets maintain a circular shape. This algorithm follows these steps:

1. **Edge Detection:** Detect edges in the image using methods like the Canny edge detector to identify potential circle boundaries.
2. **Accumulator Array Creation:** For each edge pixel, the algorithm votes in an accumulator array for potential circle centers and radii.
3. **Finding Circles:** Peaks in the accumulator array indicate the presence of circles. The algorithm identifies these peaks to determine the center and radius of each circle.
4. **Validation:** The detected circles are then validated against the original image to ensure accuracy.

This method is highly effective for detecting droplets that retain a circular shape due to consistent interfacial tension.

4.14.1 Code for Circle Hough Transform Detections

The function applies the circle Hough transform to detect droplets within images, focusing on identifying circular shapes. Below is a detailed breakdown of the function.

```
function runFullProcessing()
    imageFiles = dir(fullfile(imageFolder, '*.tif'));
```

```
    mask = imread(maskPath); % Load the mask
    saveDetectionImages = saveDetectionImagesCheckbox.Value;
    saveStepSize = saveStepSizeField.Value;
    % Parameters from UI fields
    circleRange = [circleRangeStartField.Value, circleRangeEndField.Value];
    circleSensitivity = circleSensitivityField.Value;
    adaptiveSensitivity = adaptiveSensitivityField.Value;
    % Initialize storage for centers and radii for all images

    % Initialize parallel pool
    if isempty(gcp('nocreate'))
        parpool;
    end
```

The function starts by loading the image files and mask, and initializes parameters for the circle Hough transform based on UI input fields. A parallel pool is created if it doesn't already exist.

```
    % Use parfor for parallel processing
    parfor idx = 1:length(imageFiles)
        imagePath = fullfile(imageFolder, imageFiles(idx).name);
        image = imread(imagePath);
```

Parallel processing is employed to handle each image efficiently. Each frame is read from the image folder.

```
        % Image processing to detect circles
        BW2 = imbinarize(image, 'adaptive', 'ForegroundPolarity', 'dark',
                                    'Sensitivity', adaptiveSensitivity);
        [centers, radii] = imfindcircles(BW2, circleRange, 'ObjectPolarity', 'dark',
                                'Method', 'TwoStage', 'Sensitivity', circleSensitivity);
```

The image is binarized using adaptive thresholding to prepare for circle detection. The 'imfindcircles' function is then used to detect circles based on the specified parameters for circle range and sensitivity.

```
        % Filter out circles based on the mask
        validCircles = arrayfun(@(x, y) mask(round(y), round(x)) == 255, centers(:,1), centers(:,2));
```

```
        centers = centers(validCircles, :);
        radii = radii(validCircles);
```

Detected circles are validated against the mask to ensure they fall within the region of interest. Only valid circles are retained. Due to the circular nature of the solid space in porous media, solid structures can be incorrectly identified as a detection.

```
        allCenters{idx} = centers;
        allRadii{idx} = radii;
```

Centers and radii of the detected circles are stored for each image.

```
        % Check if saving is enabled and if the current image matches the step size
        if saveDetectionImages && mod(idx, saveStepSize) == 0
            % Create the overlay image with detected circles only if saving this image
            overlayedImage = image;
            for circleIdx = 1:length(radii)
                overlayedImage = insertShape(overlayedImage, 'FilledCircle',
                    [centers(circleIdx, :) radii(circleIdx)], 'Color', 'blue', 'Opacity', 0.3);
            end

            % Save the overlayedImage with circles marked
            outputPath = fullfile(outputFolder, sprintf('processed_%s', imageFiles(idx).name));
            imwrite(overlayedImage, outputPath, 'Compression', 'lzw');
        end
    end
```

If saving of detection images is enabled via the UI, the function checks whether the current image index matches the step size for saving. If it does, circles are overlaid on the image and the result is saved.

```
    % After processing all images, save the detection results to a .mat file
    save(fullfile(outputFolder, 'detection_results.mat'), 'allCenters', 'allRadii');
    % Compile settings into a string
    settingsStr = sprintf([
        'Image Folder: %s\n', ...
        'Output Folder: %s\n', ...
```

```
        'Mask File: %s\n', ...
        'Circle Range Start: %d\n', ...
        'Circle Range End: %d\n', ...
        'Circle Sensitivity: %.3f\n', ...
        'Adaptive Sensitivity: %.3f\n', ...
        'Save Detection Images: %s\n', ...
        'Save Step Size: %d\n'], ...
        imageFolder, ...
        outputFolder, ...
        maskPath, ...
        circleRangeStartField.Value, ...
        circleRangeEndField.Value, ...
        circleSensitivityField.Value, ...
        adaptiveSensitivityField.Value, ...
        num2str(saveDetectionImagesCheckbox.Value), ...
        saveStepSizeField.Value);

    % Specify the filename for the settings file
    settingsFilename = fullfile(outputFolder, '_processing_settings.txt');

    % Write settings to the file
    fid = fopen(settingsFilename, 'wt');
    if fid > 0
        fprintf(fid, '%s', settingsStr);
        fclose(fid);
    else
        error('Failed to open settings file for writing.');
    end

end
```

Finally, detection results are saved to a ‘.mat‘ file, and processing settings are compiled into a string and written to a settings file. 6.1 illustrates an example of the results utilizing this method.

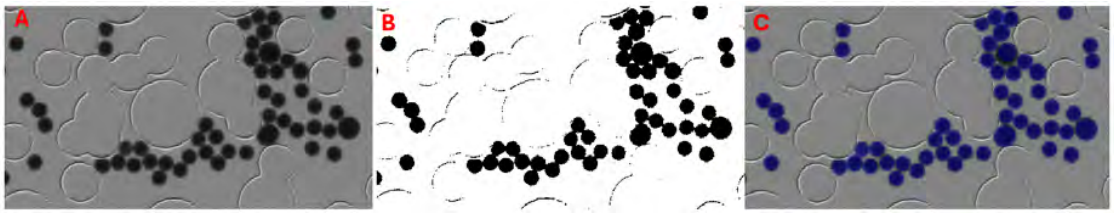

Figure 4.8: Circle Hough Transform Detection Method A) Background Subtraction and stabilization B) Adaptive Binarization C) Circle Hough Transform Detection

4.15 Object Detection: Deformable Droplets

For droplets with lower interfacial tension that deform easily, a combination of blob analysis, watershed segmentation, and morphological operations is employed. This approach involves the following steps:

1. **Preprocessing:** Apply preprocessing steps from previous section to increase contrast and enhance the image.
2. **Watershed Segmentation:** Segment overlapping droplets by treating the image as a topographic surface and finding watershed lines that separate distinct regions.
3. **Morphological Operations:** Apply operations like erosion and dilation to refine the detected shapes and separate closely packed droplets.
4. **Blob Analysis:** Detect connected regions in the binary image using properties such as area, centroid, and bounding box. This helps identify and isolate individual droplets.

These methods ensure accurate detection of both regular and irregularly shaped droplets. While there may be some errors in size calculation, the positional data and overall detection accuracy are optimized. This dual-method approach balances the need for precise detection with the challenges posed by varying droplet shapes and interfacial tensions.

Code for Deformable Droplets Detection

The function employs blob analysis, watershed segmentation, and morphological operations to detect deformable droplets. Below is a concise breakdown of the function.

```
% Tunable parameters
adaptiveSensitivity = 0.35;
```

```
minObjectSize = 100;
sizeErode1 = 6;
sizeErode2 = 4;
diskSize = 6;
gaussSigma = 6;
```

The function begins by defining several tunable parameters used throughout the image processing workflow. These parameters control the sensitivity of adaptive thresholding, the size of objects to retain, and the structuring elements for morphological operations.

```
parfor idx = 1:nFiles
    image = imread(fullfile(inputDir, files(idx).name));

    % Adaptive binarization and initial cleanup
    BW = imbinarize(image, 'adaptive', 'ForegroundPolarity', 'dark',
                                'Sensitivity', adaptiveSensitivity);
    BW = bwareaopen(~BW, minObjectSize);  % Remove small objects from binary image
```

The parallel loop reads each image and performs adaptive binarization to convert the image to a binary format. Small objects are removed from the binary image using bwareaopen.

```
    % Distances and Gaussian filtering
    D = bwdist(~BW);
    D = imgaussfilt(D, gaussSigma);
    L = watershed(-D);
    BW(L == 0) = 0;
    % Further morphological processing
    se1 = strel('rectangle', [sizeErode1 sizeErode1]);  % First erosion
    se2 = strel('rectangle', [sizeErode2 sizeErode2]);  % Second erosion
    sedisk = strel('disk', diskSize);                   % Disk for opening
```

The function computes the distance transform of the binary image and applies Gaussian filtering for smoothing. Watershed segmentation is used to separate overlapping droplets. Morphological operations, including erosion and opening, refine the detected shapes. The watershed operation splits pinched and deformed droplets, while erosion keeps them as a single droplet. Both operations split droplets that are merely in contact.

```
    BW_eroded = imerode(BW, se1);
    BW_eroded = imerode(BW_eroded, se2);
    BW_cleaned = imopen(BW_eroded, sedisk);

    % Combine with watershed processed image to finalize the binary mask
    finalBW = BW_cleaned | BW;

    % Extract properties from the final binary image
    props = regionprops(finalBW, 'Area', 'Centroid', 'BoundingBox');

    % Filter centroids based on the mask
    validProps = props(arrayfun(@(p) mask(round(p.Centroid(2)),
                    round(p.Centroid(1))) > 0 && p.Area >= minObjectSize, props));
    % Store the valid properties in the cell array
    allValidProps{idx} = validProps;
```

Erosion operations are performed using the defined structuring elements. The cleaned binary mask is combined with the watershed segmented image. Properties such as area, centroid, and bounding box are extracted from the final binary image using regionprops. The detected regions are filtered based on the mask to ensure only valid regions are considered.

```
    % Save the visual output
    numObjects = numel(validProps);
    if mod(idx, 1000) == 0  % Check if idx is a multiple of 1000
        figure('Visible', 'off');
        imshow(image); hold on;
        for i = 1:numObjects
            rectangle('Position', validProps(i).BoundingBox, 'EdgeColor',
                    'r', 'LineWidth', .5);
        end
        hold off;

        % Save the image with bounding boxes
        saveas(gcf, fullfile(outputDir, replace(files(idx).name,
                    '.tif', '_processed.tif')), 'tif');
        close; % Close the figure to free system resources
    end
end
```

Erosion ensures that droplets squeezed between pores are not eliminated. These droplets often have a narrow region in the middle, which a watershed algorithm alone might cut, resulting in two separate detections. By using double erosion, we maintain the definition of squeezed droplets, ensuring accurate detection and separation only for droplets that are genuinely in close contact. This combination ensures robust detection of squeezed droplets while also achieving proper separation of closely packed droplets.

For visualization, the function overlays detected bounding boxes on the original image and saves the result periodically.

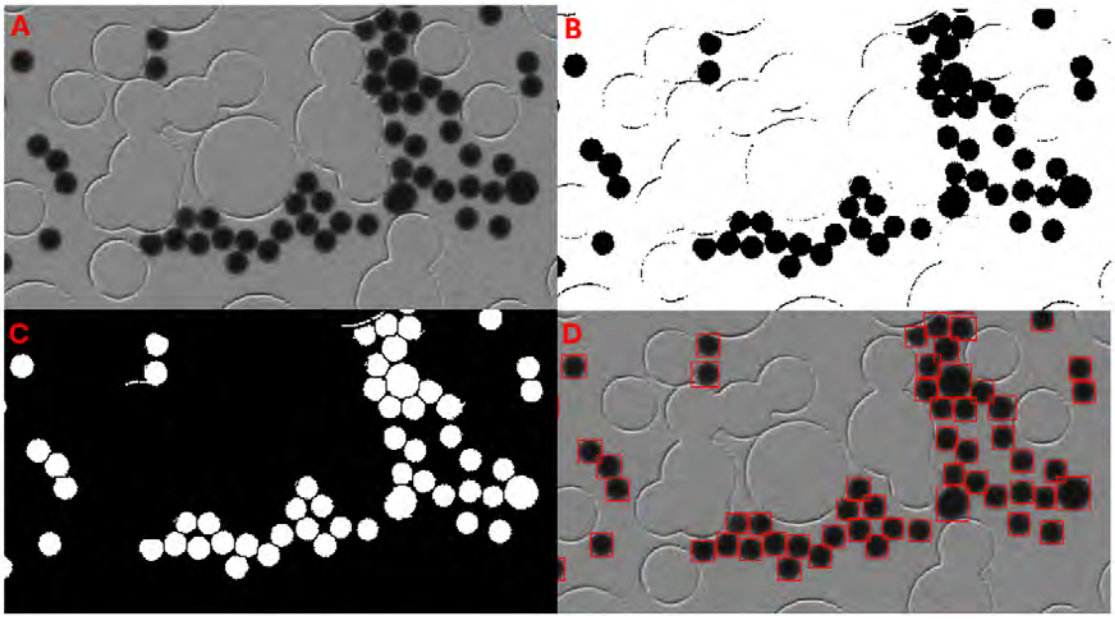

Figure 4.9: Updated Detection Method A) Background Subtraction and stabilization B) Adaptive Binarization C) Morphological and watershed processing D) Detection using Blog Analysis

4.16 Tracking Algorithm

A global nearest-neighbor algorithm is used to track detections. The detections are converted to be compatible with the tracker, which employs an interacting multiple model (IMM) filter to handle non-linear and intermittent motion by switching between constant velocity, acceleration, and turn acceleration models. The tracking process involves several key steps:

1. **Filter Initialization:** The tracking filter, such as a constant velocity unscented Kalman filter (CVUKF), is initialized to adapt to the motion dynamics of the tracked objects.
2. **Detection Association:** A global nearest-neighbor approach associates new detections with existing tracks based on spatial proximity, ensuring accurate tracking.
3. **Model Switching:** The IMM filter switches between different motion models (constant velocity, acceleration, turn acceleration) to better predict and track the object's trajectory under varying motion conditions.
4. **Cost Matrix Calculation:** A cost matrix is computed to facilitate the partial hard assignment of detections to tracks, optimizing the update of predicted positions.
5. **Track Management:** Tracks are managed using specific parameters, including assignment thresholds, confirmation thresholds, and deletion thresholds, to maintain accurate and reliable tracking over time.

Important parameters include:

Assignment Threshold: Controls the maximum cost for assigning a detection to a track.

Confirmation Threshold: Specifies the number of consistent detections required to confirm a new track.

Deletion Threshold: Defines the number of missed detections before a track is deleted.

Max Number of Tracks: Limits the maximum number of tracks that can be maintained simultaneously.

Max Number of Detections: Sets the maximum number of detections the tracker can process at one time. These parameters ensure robust tracking of multiple objects, handling complex motion patterns and maintaining accurate position updates throughout the tracking process.

```
% Tracker settings
tracker = multiObjectTracker('FilterInitializationFcn', @initcvukf, ...
                             'AssignmentThreshold', [400 500], ...
                             'MaxNumTracks', 10000, ...
                             'ConfirmationThreshold', [3 4], ...
                             'DeletionThreshold', [10 10], ...
                             'MaxNumSensors', 1, ...
                             'MaxNumDetections', 1000);
```

4.16.1 Cost Matrix

The cost matrix increases the cost of creating new tracks in the middle of the device and ending tracks there as well. This approach prefers tracks to begin at the entrance and end at the exit, helping lost tracks find the true path during intermittent and non-linear dynamics.

By employing these detailed image processing techniques and algorithms, the study ensures precise and reliable analysis of the collected data, providing a solid foundation for understanding emulsion transport in porous media.

Code for Tracking Droplets

The tracking code tracks droplets across frames by using their centroids and radii from the previous detections. Below is a detailed breakdown of the tracking code.

```
% Loop over all frames in matFile.allCenters
for frameIdx = 1:length(matFile.allCenters)

    % Use centers and radii from the mat file
    centroids = matFile.allCenters{frameIdx};
    radii = matFile.allRadii{frameIdx};
```

```
    % Convert the centroids to objectDetection reports
    numDetections = size(centroids, 1);
    detections = cell(numDetections, 1);
    for i = 1:numDetections
        % Create an objectDetection report for each detection with a dummy 3D
        dummyZ = 0;
        detections{i} = objectDetection(currentTime, [centroids(i, :), dummyZ],
                'MeasurementNoise', eye(3));
    end
```

The centroids are converted to objectDetection reports, which include a dummy third dimension for compatibility with 3D tracking systems used in Matlab. The measurement noise is set to an identity matrix.

```
    if ~isempty(detections)
        [currentTracks, ~, ~] = tracker(detections, currentTime);

        % Direct assignments instead of looping
        allTrackIDs = [currentTracks.TrackID];
        allAges = [currentTracks.Age];
        allStates = {currentTracks.State};
        allCovariances = {currentTracks.StateCovariance};
```

If detections are not empty, the tracker processes them to update the tracks. Track IDs, ages, states, and covariances are extracted directly from the currentTracks structure.

```
        % Store data for this frame
        frameData(frameIdx).trackIDs = allTrackIDs;
        frameData(frameIdx).centroids = centroids;
        frameData(frameIdx).trackAges = allAges;
        frameData(frameIdx).radii = radii;
        frameData(frameIdx).trackStates = allStates;
        frameData(frameIdx).trackCovariances = allCovariances;
    end
```

The tracking data for each frame, including track IDs, centroids, ages, radii, states, and covariances, is stored in the ‘frameData‘ structure for further analysis.

```
    currentTime = currentTime + 1;

    % Update waitbar
    if mod(frameIdx, updateInterval) == 0
        waitbar(frameIdx/totalImages, h,
                sprintf('Processing image %d of %d...', frameIdx, totalImages));
    end
end
```

The currentTime variable is incremented for the next frame, and a waitbar is updated periodically to show progress.

Advantages of the Tracking Approach: This tracking approach ensures accurate and consistent tracking of droplets over time. By converting centroids to objectDetection reports and using

a tracker system, the code maintains precise positional information. Including radii in the tracking data ensures that both the position and size of each droplet are monitored. This method provides comprehensive tracking information that adapts to changes and maintains continuity across frames. The combination of centroid and radius data ensures robust tracking of droplets, even in dynamic environments, enhancing the accuracy and reliability of the tracking process. This method is illustrated in Fig. 4.10.

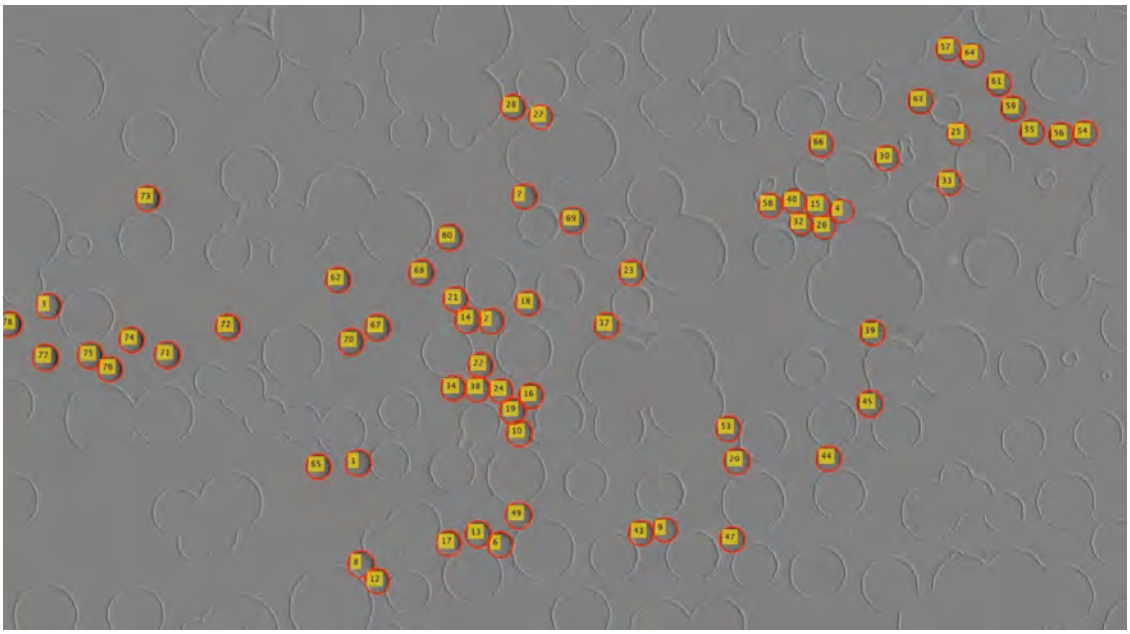

Figure 4.10: Labeled Emulsions Tracked using the Algorithm described within this section. FOV is 13 x 7.4 mm

4.17 UI Development

The development of software tools is essential for efficient data processing and analysis. This section covers the graphical user interface (GUI) design, implementation, and data structure conversions.

4.17.1 GUI Implementation

The detection and tracking algorithms were packaged into a user-friendly GUI. This GUI allows users to omit certain processing steps, save intermediate steps, and preview results before processing

the entire experiment. It leverages Matlab's parallel computing toolbox to reduce processing time and optimize performance. Key features of the GUI include:

- **User-Friendly Interface:** The GUI provides an intuitive interface that enables users to interact with the software efficiently. Users can select specific processing functions, set parameters, and view intermediate results, facilitating a streamlined workflow.
- **Customizable Processing Workflow:** Users can customize the data processing workflow by omitting certain steps or modifying parameters. This flexibility ensures that the software can adapt to various experimental needs and conditions.
- **Parallel Computing:** By utilizing Matlab's parallel computing toolbox, the GUI significantly reduces processing time. Parallel execution of computationally intensive tasks optimizes performance and enhances the user experience.
- **Intermediate Step Saving:** The ability to save intermediate processing steps allows users to review and validate results at different stages of the analysis. This feature enhances the reliability of the data processing and ensures that errors can be identified and corrected early in the workflow.
- **Previewing Results:** Users can preview the results of specific processing steps before committing to the full analysis. This capability helps in fine-tuning parameters and verifying the accuracy of the detection and tracking algorithms.
- **Efficient Data Handling:** The GUI handles data structure conversions seamlessly, ensuring compatibility with various input formats and facilitating smooth integration with other code used in the analysis pipeline.

The implementation of this GUI facilitates user interaction and ensures that the data processing workflow is streamlined and efficient. By providing a flexible, powerful, and user-friendly tool, the GUI significantly enhances the ability to analyze and interpret experimental data, contributing to more accurate and insightful findings.

4.17.2 Data Structures and Conversions

The original tracking data is saved on a per-frame basis, with each frame containing object IDs, positions, velocities, and accelerations. For efficient analysis of individual objects and their trajectories, an additional data structure is created in a map format. This assigns keys (object IDs) to

each object, associating all corresponding frame data with it. This structure allows quick access to an object's data throughout its life in the device, reducing computational time and redundancies. It also enables the trajectory GUI to update quickly and use minimal resources.

Efficient Data Handling: By organizing data in this manner, the system minimizes the processing load and enhances the speed of data retrieval. This is crucial for handling large datasets generated during the experiments, ensuring that analysis can be performed swiftly and accurately.

Trajectory Analysis: The map-based data structure supports detailed trajectory analysis, allowing researchers to track the movement of individual droplets over time. This capability is essential for understanding the dynamics of emulsion transport in porous media, providing insights into the behavior of droplets under various experimental conditions.

By following these detailed image processing and software development procedures, we ensure accurate analysis and efficient data handling, providing a robust foundation for studying emulsion transport in porous media. The integration of sophisticated algorithms with user-friendly interfaces enhances the research process, enabling precise control and comprehensive analysis of experimental data.

4.18 Visualisation Methods

This section and the following subsections will detail the various visualization methods employed in this work, which have not been extensively covered in previous publications.

4.18.1 Simulations

Creating an effective visualization method for our simulations and figures is crucial, as microfluidic characteristics and flow dynamics can be complex and multifaceted. We employ the HSV color space for visualizing the flow field around the droplet. Unlike the integrated RGB color space, HSV allows for better separation and distinction of components.

The HSV color space consists of three components: hue (color), saturation (purity), and value (brightness). Hue represents the flow direction, saturation indicates the fluid percentage, and value shows the magnitude of the flow. This approach is more intuitive and aligns with human color perception, providing clearer insights into the flow dynamics.

Advanced visualization methods enable us to observe changes in various parameters simultaneously, aiding in result interpretation and identifying key dynamics for further investigation. This method has proven valuable in understanding the physics of droplet formation and the flow fields within and around the droplets. This is clearly shown in Figure 3.1

4.18.2 Advanced Visualization Method for Emulsion Residency Time in Porous Media

In order to better visualize the residency time of emulsions within porous media, this code involves several key steps, starting with the utilization of a predefined binary mask to delineate regions of interest within the experimental setup.

A crucial component of this visualization method is the computation of density maps from the positional data of tracked particles. These maps offer a quantitative depiction of particle concentration across the experimental domain, providing insights into how emulsions distribute within the porous medium over time.

The process continues with the creation of a difference map to highlight variations between density maps. Values outside the mask are set to NaN, ensuring the visualization focuses exclusively on relevant regions. This difference map is then enhanced using a custom diverging colormap, which transitions from red to black for negative differences and from black to blue for positive differences. This colormap effectively distinguishes areas of varying residency times, offering a clear and intuitive visual representation of the spatial dynamics of emulsions.

The final visualization is displayed as a heatmap using MATLAB's `pcolor` function. By applying flat shading, grid lines are removed, which enhances the clarity of the visual data. The 'jet' colormap is employed to further distinguish between different values, and a colorbar is included to provide a reference scale. The y-axis direction is reversed to maintain proper orientation, and the aspect ratio of the axes is set to equal, preserving spatial relationships.

This visualization method underscores the significance of precise and accessible representation in scientific research. By leveraging advanced visualization techniques, this approach not only enhances our understanding of emulsion behavior within porous media but also establishes a robust framework for future research. The meticulous attention to detail in the creation and presentation of these visualizations ensures that complex data is conveyed effectively, facilitating both scholarly analysis and practical applications. This code can also be used with velocity data to create a

velocity density map as shown in as shown in Figure **??**.

Figure 4.11: Velocity Density map normalized by Interstitial Velocity Displaying regions where burst events occur

4.18.3 Interactive GUI for Trajectory Visualization

To facilitate the visualization of the trajectories of emulsions within porous media, we introduce a graphical user interface (GUI) designed to display the paths of tracked objects stored in a trackData map object. This GUI allows users to select a range of trackIDs using a slider, with the corresponding trajectories overlaid on a provided background image. Additionally, the interface offers tunable parameters such as linewidth, line color, and line style to enhance the clarity and detail of the visualization.

The method requires that both the trackData map and a representative background image are loaded into the workspace prior to execution. The trackData map is a containers.Map object where each key corresponds to a trackID, and the associated value is a structured array containing the tracking data for that object across various frames.

Initially, the tracking data is converted to a trajectory format suitable for the GUI. The representative background image is loaded and displayed as the visualization backdrop. A figure window is created to host the GUI components, including controls for adjusting the linewidth, selecting the line style, and specifying the range of trackIDs to be visualized.

The user can interact with several GUI elements:

- A text box to set the linewidth of the trajectories.
- A dropdown menu to select the desired line style from options such as solid, dashed, dotted, and dash-dot.
- Text boxes to input the start ID and the range of trackIDs to be visualized.
- A button to update the visualization based on the selected parameters.

Upon triggering the update, the trajectories within the specified range are overlaid on the background image. Each trajectory is plotted using the selected linewidth and line style, ensuring that the visualization is both clear and customizable according to the user's preferences.

The GUI is designed to provide a dynamic and intuitive way to explore the motion patterns of emulsions, allowing for real-time adjustments and immediate visual feedback. This interactive approach not only enhances the user's ability to analyze the spatial dynamics of tracked objects but also supports more effective communication of complex data through visually compelling and easily interpretable graphics.

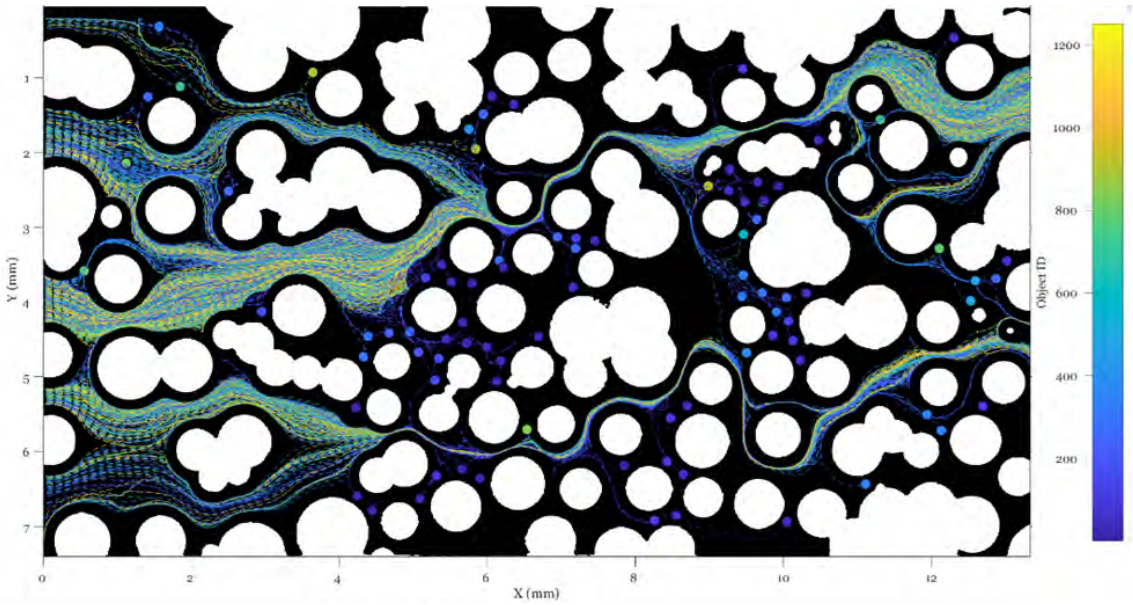

Figure 4.12: Trajectory Results

4.18.4 Simulation and Visualization of Sphere Packing

To effectively visualize the packing of spheres within a defined volume, this method involves a comprehensive approach that includes simulation parameters, sphere placement, and detailed visualization techniques. The primary goal is to simulate the packing of a specified number of spheres, ensuring that they fit within the given volume constraints while allowing for a slight overlap to maximize space utilization. This method serves as a way to create simulated bead-packing designs in porous media, enabling researchers to test and analyze these designs by acquiring 2D slices of the simulation.

The simulation begins with the definition of key parameters:

- **Total Spheres:** The total number of spheres to be packed, set to 5000 in this case.

- **Max Attempts:** The maximum number of attempts to place each sphere without overlap, set to 25.
- **Volume Size:** The dimensions of the volume (X, Y, Z) are specified as [30, 15, 25].
- **Mean Radius and Standard Deviation:** The mean radius ($\mu = 0.75$) and standard deviation ($\sigma = 0.05$) of the spheres follow a Gaussian distribution.
- **Overlap Allowance:** A fractional reduction of the sphere radius for overlap checks, set to 0.2.

The simulateSpherePacking function is then called to generate the packed spheres based on these parameters. This function attempts to place each sphere within the volume by randomly generating positions and ensuring no significant overlap with already placed spheres. The result is a set of spheres defined by their coordinates and radii.

For visualization, the method includes both 3D and 2D representations:

- **3D Visualization:** The spheres are visualized in a 3D plot, where each sphere is represented by a scaled and translated sphere surface. The plot includes labels for the axes and a title, and it utilizes Gouraud lighting to enhance the appearance. A light source is added to improve the visualization of the spheres.
- **2D Cross-Section Visualization:** This is achieved through a GUI that allows users to view cross-sections of the packed spheres at different depths (z-values) within the volume. A slider is provided to adjust the z-value, dynamically updating the plot to show the intersection of spheres with the current plane. This 2D representation uses circles to depict the cross-sections of spheres, providing a clear view of their spatial distribution.

The combination of these visualization techniques offers a comprehensive view of the sphere packing, facilitating a deeper understanding of spatial arrangements and packing density within the volume. The interactive elements, particularly in the 2D visualization, allow for detailed exploration of the packed structure. This method is particularly valuable for creating and testing simulated bead-packing designs in porous media, with the Gaussian distribution of beads serving as the basis for this simulation.

The next section will explore a bimodal selection of beads based on volume, offering a different approach to simulating bead packing in porous media.

4.18.5 Bimodal Bead Packing Simulation

This subsection describes a method for simulating the packing of two types of spheres within a 3D volume. The goal is to fill a predefined space with spheres of specified radii and volume percentages. This simulation serves as an extension to the previous method, incorporating a bimodal selection of beads based on volume to better mimic the complexities of porous media designs.

The simulation involves the following key parameters:

- **Volume Size:** The dimensions of the packing volume (X, Y, Z) specified as [30, 15, 10].
- **Sphere Radii:** Radii of the two sphere types, where the first type has a radius of 0.25 units and the second type has a radius of 0.106 units.
- **Volume Percentage:** The volume percentage allocated to the first sphere type, set to 50%.
- **Max Attempts:** The maximum number of attempts for placing each sphere without overlap, set to 100.

The simulateTwoSizeSpherePacking function generates the packed spheres based on these parameters. This function calculates the required number of spheres for each type based on their volume percentages and attempts to place them within the volume while avoiding significant overlaps.

For visualization, the method includes both 3D and 2D representations similar to the Gaussian distributed bead packing code.

Additionally, the method includes procedures for manipulating the smaller spheres to fit more compactly within the packing structure. Small spheres are pulled towards the nearest larger spheres, and their positions are updated accordingly. This adjustment helps achieve a more realistic packing density, and distribution.

The simulation concludes with the generation of a DXF file representing a 2D slice of the packed spheres, which is useful for further analysis and practical applications. The slice parameters, such as the center and thickness along the Z-axis, can be adjusted to meet specific research requirements. This DXF file can then be converted to a 2D autoCAD file to prepare for printing.

This method not only enhances the understanding of packing densities and spatial arrangements within porous media but also provides a robust framework for simulating and visualizing complex bead-packing designs.

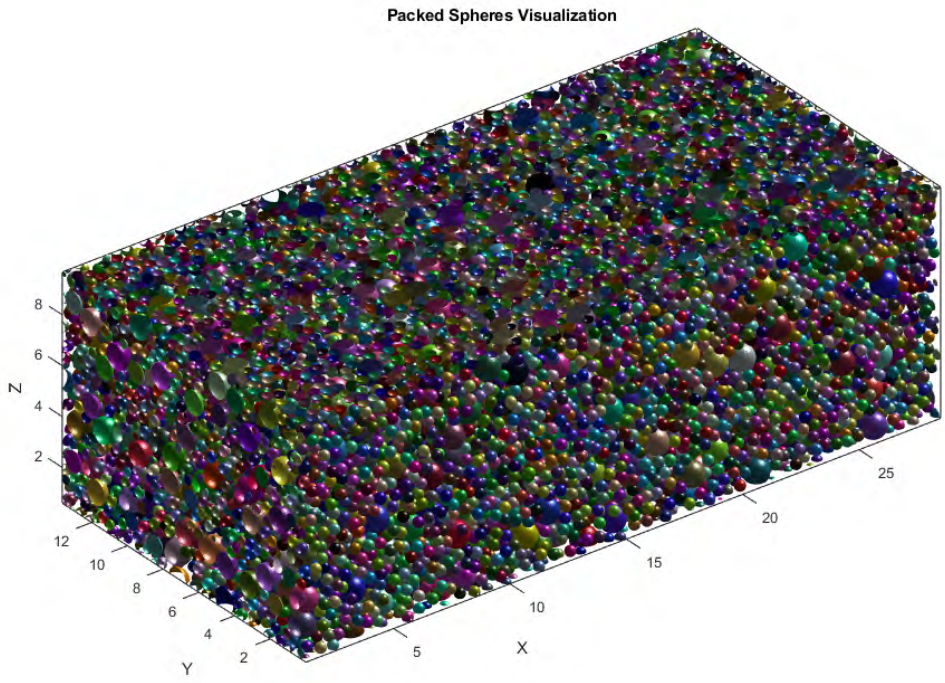

Figure 4.13: Bimodal Spherical Packing Simulation Results

4.18.6 Velocity Data Conversion and Histogram Calculation

This section provides a concise summary of the steps taken to process and visualize velocity data from two experiments:

1. **Velocity Conversion:**
   - Velocities for both experiments are converted from pixels per frame to millimeters per second using specific conversion factors.
2. **Edge Computation for Histograms:**
   - Logarithmically spaced edges are calculated for both positive and negative x and y velocity values from both experiments, ensuring appropriate binning for histogram creation.

This was done to differentiate between tightly packed values.

3. **Histogram Calculation and Visualization:**

   - Histograms for both positive and negative velocity values are computed and normalized to probability densities. These histograms are then plotted to visualize the velocity distributions.
   - Histograms for x velocities from both experiments are plotted together, using logarithmic scaling on the y-axis to highlight differences in velocity distributions.
   - Similarly, histograms for y velocities are computed and visualized.

4. **Magnitude Velocity Analysis:**

   - Combined magnitude velocities from both experiments are used to compute logarithmically spaced edges.
   - Histograms of magnitude velocities are calculated and normalized to probability densities, then plotted with logarithmic scaling on both axes.

5. **Overall Comparison:**

   - Histograms for all datasets (x and y velocities, and magnitudes) are plotted together using shared bin edges, allowing for direct comparison of distributions between the two experiments and additional PIV data.

4.18.7 Residency and Velocity Analysis

This section outlines the process of analyzing age and velocity data of tracked objects in an experiment. The key steps include loading mask data, calculating maximum object age, computing average velocities, and visualizing the results.

1. **Loading Mask and Computing Maximum Age:**

   - The mask image is loaded to define the regions of interest.
   - Maximum age of tracked objects is determined by iterating through the track data and converting frame counts to seconds.

2. **Average Velocity Calculation:**

- Average velocities for each tracked object are computed by averaging the magnitudes of their recorded velocities.
- Objects with velocities above a certain threshold are filtered out if unrealistic and likely due to incorrect tracking.

3. **Velocity Mapping:**
   - A velocity accumulation map and a density map are initialized to store the sum of velocities and counts respectively.
   - These maps are used to compute an average velocity map, which is then converted to represent velocities in millimeters per second.
4. **Visualization:**
   - The average velocity map is normalized and displayed as a heatmap, with physical measurements labeled on the axes.
   - The trend of average velocities for objects that complete their paths is plotted against object numbers.
5. **Filtering and Regression Analysis:**
   - Objects are filtered based on their completion of paths and maximum age.
   - A log-log scale transformation is applied to analyze the relationship between average velocity and object age.
   - Linear regression is used to classify objects into two groups based on their velocity trends, and the results are visualized.
6. **Centroid Analysis:**
   - Final Y-positions of centroids are analyzed for objects classified into two paths.
   - Start times and final Y-positions are plotted to examine the movement patterns.
7. **Dynamic Visualization:**
   - Y-positions of centroids closest to a range of target X-values are dynamically analyzed and plotted.
   - The figures are saved as PNG files, providing a visual representation of centroid paths at different target X-values.

These analyses offer insights into the dynamics of tracked objects, facilitating a deeper understanding of their behaviors within the experimental setup. It is the primary steps used to identify the preferential paths in the aformentioned chapter.

4.18.8 Final File Types and Conversion Descriptions

This subsection provides a brief overview of the final file types used and their respective data structures.

frameData Struct: The `frameData` struct represents tracking data across multiple frames, with dimensions of `1xM`, indicating data for M frames. Each entry in the struct corresponds to a frame and includes information about N tracked objects. The structure for each frame includes:

1. **trackIDs:**
   - **Size:** `1xN`
   - **Type:** double array
   - **Description:** Unique identifiers for each tracked object in the frame.
2. **centroids:**
   - **Size:** `Nx2`
   - **Type:** double array
   - **Description:** (x, y) coordinates for the centroid of each tracked object.
3. **trackStates:**
   - **Size:** `Nx4`
   - **Type:** double array
   - **Description:** State of each tracked object, with columns representing:
     - Column 1: x position
     - Column 2: x velocity
     - Column 3: y position
     - Column 4: y velocity
4. **radii:**

- **Size:** `Nx1`
- **Type:** double array
- **Description:** Radius of each tracked object.

5. **trackAges:**
   - **Size:** `Nx1`
   - **Type:** uint32 array
   - **Description:** Age (number of frames since detection) of each tracked object.

Note: The value of N varies for each frame and represents the number of objects tracked in that particular frame.

trackData Map Object: The `trackData` variable is a MATLAB `containers.Map` object designed to efficiently store and retrieve tracking data from multiple frames. Each key in the map corresponds to a unique `trackID` of an object, and the associated value is an array of structured data representing that object's tracking data across frames. The structure of the data for each object includes:

1. **positionfromstates:**
   - **Size:** `1x2`
   - **Type:** double array
   - **Description:** (x, y) position from `trackStates` for the object.
2. **centroid:**
   - **Size:** `1x2`
   - **Type:** double array
   - **Description:** (x, y) coordinates for the centroid of the object.
3. **velocity:**
   - **Size:** `1x2`
   - **Type:** double array
   - **Description:** (x, y) velocity of the object.

4. **radius:**
    - **Size:** `1x1`
    - **Type:** double
    - **Description:** Radius of the object.
5. **frame:**
    - **Size:** `1x1`
    - **Type:** double
    - **Description:** Frame number from which this data was extracted.
6. **age:**
    - **Size:** `1x1`
    - **Type:** uint32
    - **Description:** Age (number of frames since detection) of the object.

To retrieve data for an object with a specific `trackID`, use:

```
objectData = trackData(trackID);
```

where `objectData` will contain an array of structured data for that object across all frames where it appeared.

The final map object `trackData` is saved to a .mat file named `trackData_mapped.mat`.

4.18.9 Annotating Results on Images

This section describes the process of annotating tracked object data on image frames and compiling the annotated images into a video.

1. **Mapping and Updating Track IDs:**
    - A mapping structure is created to uniquely identify and update trackIDs in `frameData`.
    - The trackIDs in `frameData` are updated using this mapping.

2. **Handling Missing Data:**
    - For each frame, trackStates centroids are extracted and matched with centroids and radii from the `matFile`.
    - If a match is not found, the radius is set to the average value of the other radii in the same frame.
    - `frameData` is updated with the matched radii and centroids.
3. **Annotating Images:**
    - Images are loaded from the specified input folder, and a corresponding output folder is created if it does not exist.
    - For each image, the corresponding tracking data is overlaid on the image. Circles are drawn around tracked objects, and trackIDs are annotated next to them.
    - Annotated images are saved in compressed TIFF format in the output folder.
4. **Creating a Video:**
    - Annotated images are sorted and compiled into a video using the `VideoWriter` object.
    - The frame rate and quality of the video are set as required.
    - Each annotated image is added to the video, which is then saved in MP4 format.

This process allows for the clear visualization of tracked objects over time, facilitating a better understanding of their movements and behaviors within the experimental setup.

4.19 Conclusion

The methods detailed here are employed in the following chapters to visualize and analyze the experimental data. They establish a robust analytical framework, ensuring that results are consistent and comprehensive. Designed for user-friendliness, these methods feature an intuitive UI that allows for parameter adjustments specific to each experiment and offers preview capabilities to streamline long processing times.

Looking ahead, the goal is to process future experimental data and create masks, frame data, and Map objects, which will be stored in databases. These databases can then be leveraged for machine learning applications, enhancing our understanding of emulsion transport in porous media.

Chapter 5

Preferential Flow Paths in Emulsion Transport

Building on the foundational insights from the initial research on microfluidic droplet generation using variational mode decomposition (VMD), which provided crucial understanding of droplet size and concentration control, we now transition from the methods detailed in the previous chapter to explore the behavior of emulsions within porous media. In this investigation, we employ techniques to precisely control the concentration and sizes of emulsions injected into a two-dimensional porous medium using an on-chip microfluidic drop-maker. This ability to finely tune droplet characteristics is vital, as it allows for detailed observation and analysis of how these emulsions interact with the intricate structures of porous media. The dynamics of these interactions are characterized by their high intermittency, despite the relatively slow average velocity over the trajectory of individual emulsions. At lower concentrations, the emulsions frequently move through pores that exhibit higher local velocities, which may be smaller than the size of the emulsion droplets themselves. This interaction can lead to the trapping of emulsions and a reduction in the porosity of the medium. As the porosity decreases, certain pathways begin to dominate the flow of emulsions, highlighting the significant impact that controlled droplet formation has on the macroscopic transport properties within the medium. Introducing slight variations in the size distribution of these emulsions further reveals additional pathways for transport, underscoring the importance of droplet size control as observed in our earlier studies. These findings illustrate the critical role of microfluidic control in influencing the larger-scale behaviors of emulsions in porous environments. Such detailed understanding of pore-level dynamics, informed by our prior work on droplet formation, provides invaluable insights into the overall flow patterns and enhances our ability to predict

and manipulate fluid movement in various applications. This research progression demonstrates how foundational studies on the microscale control of fluid properties can be effectively applied to complex, heterogeneous systems, offering profound implications for industrial, medical, and environmental applications. By bridging microfluidic technology with the study of porous media dynamics, we can address practical challenges and innovate in the design and optimization of fluid transport processes. This chapter has been adapted from This chapter has been adapted from Izaguirre's 2024 paper. [36]

5.1 Introduction

Transport of emulsions in porous media is a subject of significant interest in industrial, medical, and environmental applications including many food products, drug delivery, and immiscible displacement. [6, 39, 44, 45, 60, 67] The diversity and heterogeneity of most natural and environmental porous materials lead to heterogeneous flow distribution which significantly impacts the transport of droplets of emulsions in a medium. [1] Furthermore, the transport properties of porous media can undergo dynamic alterations as a result of the flow and retention of materials inside the pores. [21,58,59] Growth of biofilms in filters [39,53], transport of water-based emulsion in personal care product [4, 9], or oil recovery [44, 46, 58, 59] are some of the examples in which the properties of the medium change in response to the flow of droplets of an immiscible phase. Earlier research shows that although the changes in bulk transport properties such as medium permeability and interstitial flow velocity are not considerably large upon the flow of individual droplets, the local and pore-scale flow can change dramatically leading to anomalous flow behavior locally. [14, 58, 59, 88] The transport properties of a single droplet of emulsion in porous media are dictated by the droplet sizes and network properties such as pore size distribution and medium wettability. [14,29,60,67,87] Hence, the dynamics of a droplet can be described by the balance of the viscous, interfacial, and drag forces. Only two non-dimensional numbers Capillary number (ratio of viscous to interfacial forces) and Weber number (ratio of drag to interfacial forces) are used to describe the dynamics of droplets with small deformations. [7, 11, 50, 60, 74] However, the collective dynamics of a group of emulsions in a complex network of pores are affected by the fluctuations in local flow due to the droplet-droplet and droplet-pore structure interactions. [29] The collective transport of high concentration of emulsions in a medium with random pinning sites shows that dynamics of the droplets sharply transition from a creeping regime to flow along smectic rivers and in groups. [40] The deformation of droplets in these experiments was negligible and the majority of the droplets (99.7%) never squeeze through small pores and only pin on the surfaces. Furthermore, measurements of

bulk transport of large quantities of polydisperse droplets stabilized by a surfactant and injected into a three-dimensional porous medium show that mostly small droplets appear in effluent and large droplets remain trapped in the medium due to the large pressure required to deform the large emulsion droplets. [14,29,87,92] Nevertheless, the pore-level and collective dynamics of droplets in a network of pores, and the impact of trapping and re-mobilization of droplets on pore-level and macro-scale transport properties remain to be examined at the pore-scale. One of the challenges in accurate experimental investigation is tracking and precise object detection in an environment where the interfaces of droplets are in contact and droplets deform based on pore sizes.

In this paper, we quantify the pore-level dynamics of monodisperse emulsions flowing through a two-dimensional (2D) porous medium experimentally. By incorporating a microfluidics drop-maker on the same chip as the 2D porous medium, we control the concentration and sizes of the injected emulsions precisely. In these experiments, we track individual droplets as they flow into the medium using optical microscopy and a long-range recording mode while monitoring the bulk pressure gradient across the medium. By employing advanced image analysis and object tracking, we track individual emulsions as they flow through the medium. We show that at low concentrations, emulsions flow through pores with higher local velocities without being selective about the size of the pores they encounter, and this lack of selectivity can lead to the emulsions becoming trapped. Once a significant number of pores are filled with droplets, newly injected emulsions continuously flow through a few remaining open paths. We show that the average velocity of the droplets that flow through the medium scale with the inverse of the total time of residence in the medium and is proportional to the path lengths of the droplets independent of the distribution of sizes of the emulsions.

5.2 Experimental Method

We generate emulsions and characterize the dynamics of emulsions in 2D micromodel of porous media using microfluidics, fluorescent microscopy, and bulk transport properties of the medium. One of the challenges in studying emulsions in porous media is to control the size, concentration, and injection frequency of emulsions. [18,29] This is mainly due to the density contrast between the dispersed phase (emulsions) and the continuous phase. To overcome this challenge, we leverage the capabilities of microfluidics in producing well-controlled monodisperse emulsions. [7,51,71,80] We design an on-chip drop-maker in series with a 2D porous medium as shown in Fig.**??**a. This design allows us to control the injection frequency and concentration of emulsions in a porous medium.

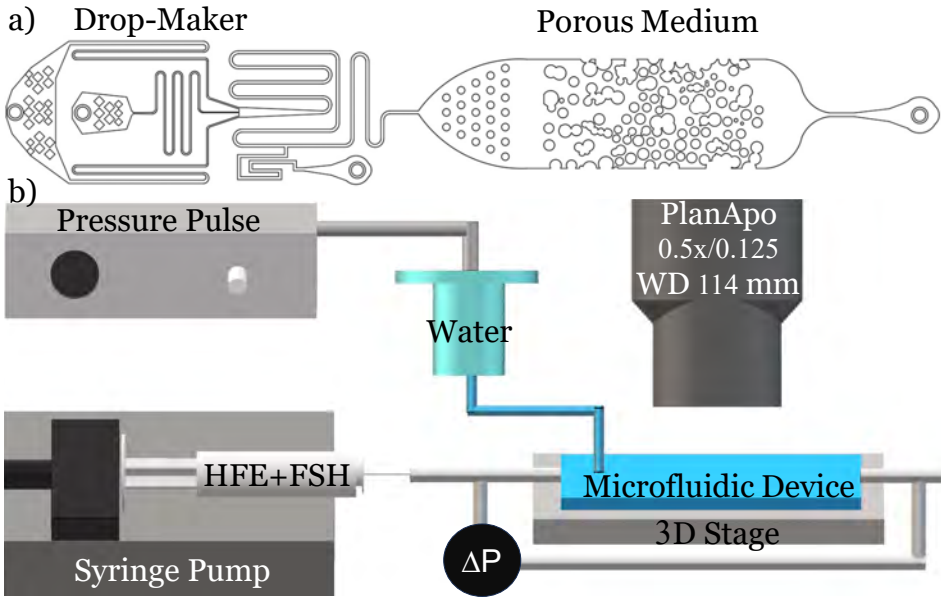

Figure 5.1: **a)** 2D drawing of the drop-maker and porous medium on one chip. **b)** Schematic of the experimental setup.

5.2.1 Microfluidics 2D porous media

To generate monodisperse droplets and inject them into a porous medium in a laminar flow condition, we design the microfluidic drop-maker to operate in the dripping regime. [80] The drop-maker consists of an inlet for the dispersed fluid (water and 0.1w% fluorescin sodium salt) at the center, and two inlets for the continuous phase on either side. The continuous phase is a fluorinated oil HFE750 (engineering fluid by 3M) with 5w% surfactant FSH oil (by Krytox). The interfacial tension between the dispersed phase and the continuous phase is $\gamma = 26$ mN/m. In the dripping regime, the droplet sizes are proportional to the inlet geometry. [4] At equilibrium, where the inner phase fluid is protruding out of the inlet and into the outer phase, the pressure inside the droplet P_d is balanced by the pressure in the outer fluid (P_0) and the capillary pressure, $P_d = P_0 + \frac{2\gamma}{R_d}$. Here, R_d is the radius of the droplet. The droplet snaps off once the pressure inside the droplet exceeds the outer pressure. The radius of the droplet is $R_d > 2R$, in a channel with radius R and circular cross-section. [5, 19, 20, 64, 81]

Here, the water inlet is a rectangular channel with dimensions of 84μm $\times$ 200μm, entering an area measuring 1050μm $\times$ 200μm, as shown in Fig.**??**a. The two oil inlets each have dimensions of 115μm $\times$ 200μm. The entire channel spans 1100μm in length and 200μm in height, tapering down to a 325μm channel before entering the porous medium. We use a syringe pump to inject the continuous phase at a constant flow rate of 5 mL/hr. However, to control the generation of individual

droplets precisely, we use a pneumatic pump as shown in the schematic of the experimental setup in Fig.??b. The viscous pressure of the flow of the continuous phase is balanced by a constant pressure, provided by the hydrostatic pressure of the closed water column. The pneumatic pump applies an additional pulse of pressure to the closed water column at 174 kPa for a duration of 200 ms. This method robustly produces monodisperse emulsion droplets with an average diameter of 295±7 μm with a narrow distribution as shown in Fig.5.2. The corresponding capillary and Weber number of the dropmaker in these experiments are Ca = 3×10^{-3} and We = 1.5×10^{-3}. The radii of the emulsions match our prediction of $R_d > 2R$. The snap-off and monodispersity of the droplets in our experiments are assisted by the hydrophobic coating (aquapel) of all surfaces. [55] However, small variations in pulses result in a slightly more polydisperse distribution of droplet sizes. For example, we find that multiple consecutive pulses result in a wider distribution of droplet sizes of 350±10 μm as shown in Fig.5.2. We continuously monitor the pressure gradient across the medium using a pressure transducer (Omega-PX409) and apply variational mode decomposition to the signal to eliminate the high-frequency noise of the transducer. [35]

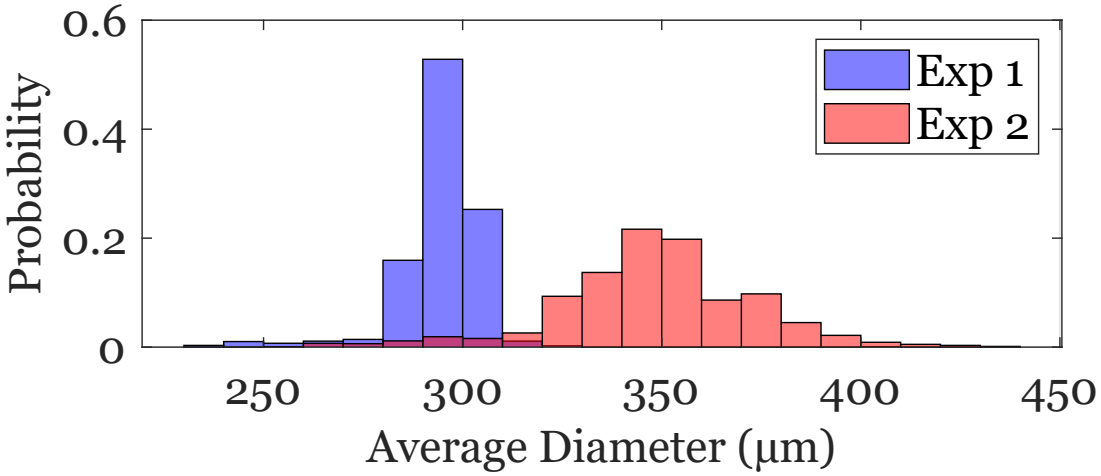

Figure 5.2: Probability distribution function of the sizes of the emulsions in monodisperse (Exp1: blue) and polydisperse (Exp2: red) experiments. The total number of emulsions in Exp1 is 1334, and in Exp2 is 1666.

We design and fabricate 2D porous media using standard soft lithography and microfluidics techniques. [83] To obtain a pattern of random pore size distribution, we use a 2D micrograph of a three-dimensional glass bead-pack imaged by a confocal microscope. [1] We further enhance the pore size heterogeneity by imposing a gradient in pore size distribution with a larger porosity at the inlet compared to the porosity downstream. This gradient in porosity represents the hetero-

geneity of natural and geological porous structures. [8] We quantify the porosity and pore size distribution of the 2D porous medium using a novel algorithm that utilizes Voronoi tessellation and skeletonization. [22, 41, 42, 82] The pore size distribution in the medium has an average pore size of 403 μm and varies between 150 and 1150 μm as shown in Fig.5.3.

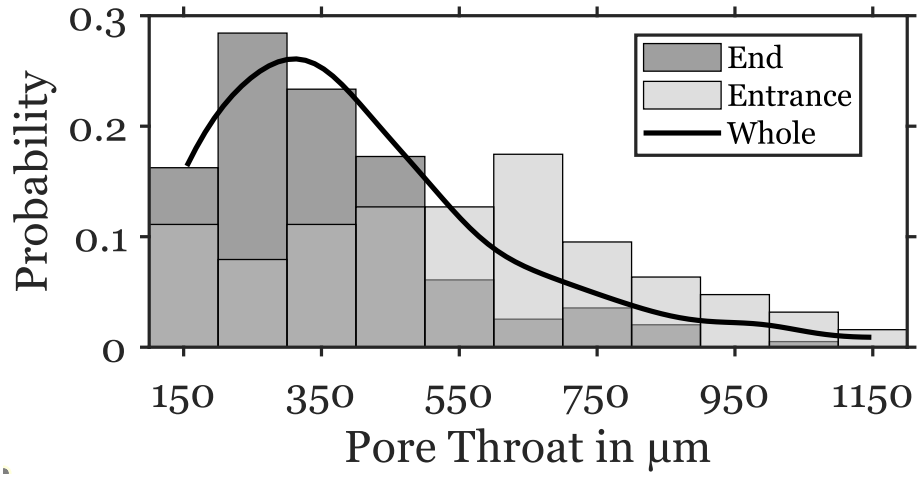

Figure 5.3: Probability distribution of the pore sizes in the medium (solid line), the 1/3 entrance to the medium (light gray), and the 2/3 end of the medium (dark gray)

To ensure that the emulsion droplets are small enough to enter the medium, the physical dimensions of the porous medium are proportionally adjusted to allow some passage of the droplets. In these experiments, we utilize a microfluidics 3D printer (CADworks3D Pr110-385nm). Using this cutting-edge resin-based 3D printer, boasting an XY resolution of 40×40 μm^2 and a Z resolution of 5 μm, we fabricate microfluidic master-molds with a variety of dimensions. To achieve smooth surfaces on the master-mold, which is critical for the performance of our microfluidic devices, we optimize the printing settings for a commercial powder-base resin with low light dispersion. By controlling the UV-exposure and curing time, the edges and surfaces are smooth. The master-molds are then filled with polydimethylsiloxane (PDMS) and cured at 60^o C before plasma cleaning and bonding to a glass slide.

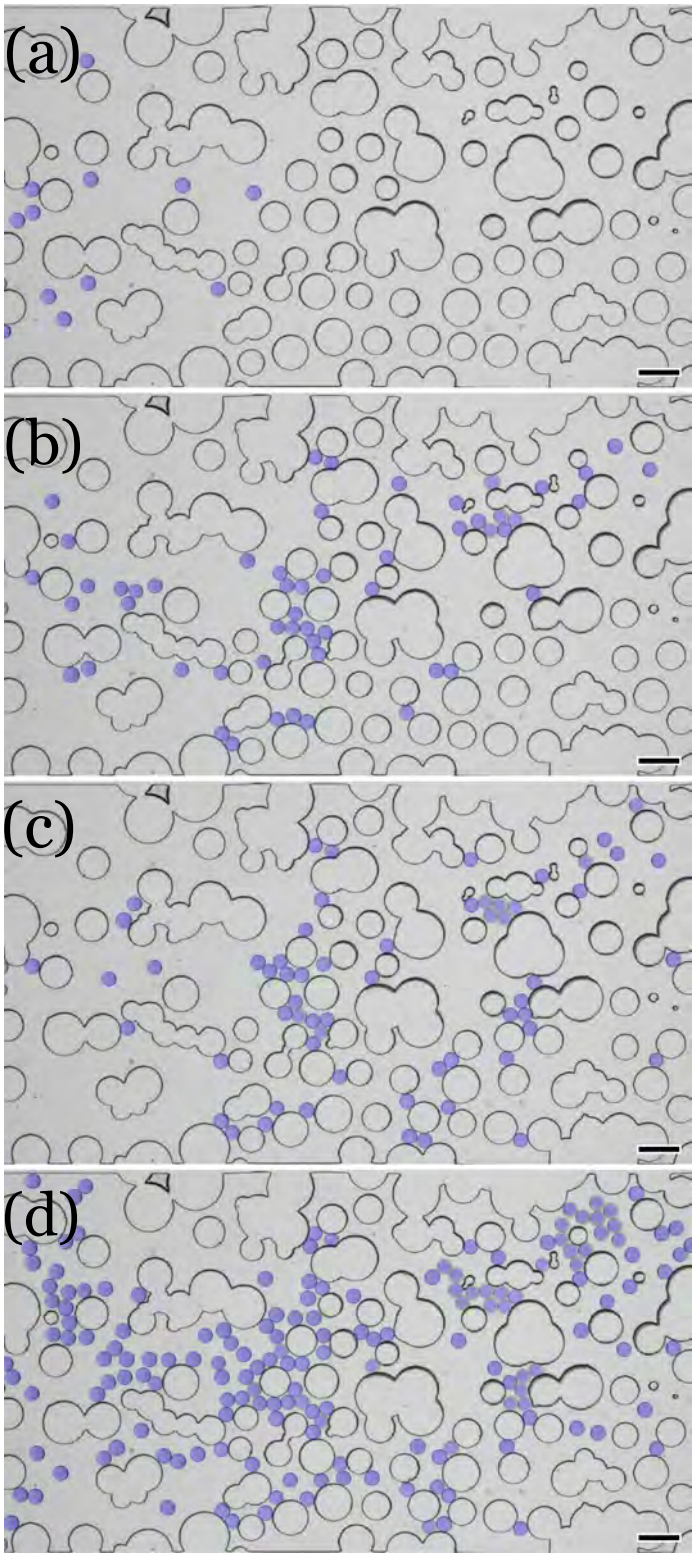

Figure 5.4: Transport of individual droplets injected into a 2D porous medium as a function of time a) 5 s, b) 25s, c) 42.5s, d) 62.5s. Blue circles mark the emulsions. Scale bar is 1 mm.

5.2.2 Pore-scale Imaging

To quantify the dynamics of emulsion within the porous medium, we use a widefield optical microscope (Axiozoom) and a long-range-record camera (FasTec IL5). The camera is operated at 50 Hz with a resolution of 2500×1000 pixels at 16 bits, providing a high dynamic range. The microfluidic porous medium is illuminated with a collimated RGB backlight LED providing a high contrast image where emulsions can be identified.

We characterize the dynamics of emulsions at the pore-level and across the entire model porous medium utilizing a modified particle tracking algorithm that accounts for objects in close contact and with highly intermittent kinematics. While most particle tracking methods are optimized to identify sparse objects [57], emulsions trapped in a porous medium are in close contact with each other and are squeezed into a solid structure and can be slightly deformed, see Fig.5.4. Here, we first subtract the solid background while applying a drift correction on all images to enhance the accuracy of object detection. Using a Circular Hough Transform, we identify individual droplets within the medium as shown in Fig.5.4. Once all droplets are identified, we employ a Global Nearest-Neighbor (GNN) tracking method under Sensor Fusion and Tracking Toolbox in MATLAB R2023. The GNN tracker uses the global nearest-neighbor assignment algorithm to match its detection to identified tracks based on predicted position, velocity, and acceleration. The GNN tracker forms a cost matrix by calculating the distance between each detection and existing tracks. Using this cost matrix, it categorizes the detected objects into either assigned pairs with tracks or unassigned, subsequently updating or initializing tracks as appropriate. Since our detection method is highly accurate, we assign a high cost to new tracks created outside the spatial area in which new emulsions are introduced into the field of view. We overcome the natural challenge of tracking objects that are constantly trapped and mobilized by using an Interacting multiple-model filter. The high-resolution imaging and enhanced edge detection are crucial in successfully applying the GNN tracker to the highly intermittent dynamics of emulsion. See supplementary materials of Fig.5.4 providing a dynamic visual representation of the emulsion transport through the porous medium.

5.3 Results

The dynamics of emulsions in porous media are highly intermittent despite the tendency of the droplets to travel at the center of the pores. As single droplets enter the porous medium, they flow through paths with a higher average velocity. In these experiments, we form and inject the droplets at low concentrations and distribute their points of entry into the medium in the cross-

sectional direction, Fig.5.4a. The low concentration of emulsion is crucial to avoid a yield stress behavior. [82] The emulsions flowing into a porous medium, naturally follow the streamlines with larger velocities. However, there is no feedback mechanism that would prohibit their entry to a pore or a pore throat smaller than the diameter of the droplet. Interestingly, in a porous medium with a random distribution of pore sizes, a considerable number of high-velocity paths flow through small pores. Hence, we observe a substantial number of emulsions getting trapped in the medium during the injection of the first batches of emulsions as seen in Fig.5.4b. While a few emulsions find their way to the outlet, more than 65% of the emulsions are trapped following their predecessors as seen in Fig.5.4c. A droplet trapped in a pore does not completely block the flow of the continuous phase in this area and the continuous phase passes around the droplet. Consequently, the changes in the local flow within the first few seconds of these experiments do not lead to a change in the global flow, as opposed to pore blocking seen in experiments focusing on conformance control in oil recovery. [59,91] Additionally, our continuous measurement of the pressure drop across the medium confirms that the bulk flow is not affected by a few trapped emulsions in the medium. Trapping of a few droplets in the medium changes the medium porosity from 55% in Fig.5.4a to 49% in Fig.5.4c. Despite the considerable change in porosity, the pressure gradient across the medium increases only from 1400 Pa to 1450 Pa, further confirming the presence of a flow around individual emulsions and through the pores. Further injection of emulsions into the medium results in substantial clogging of individual pores in the medium as seen in Fig.5.4d. Considering that the volumetric flow rate is held constant throughout this experiment, one expects that flow should be redirected to other open pores. Once the porosity of the medium decreases to 36% and many pores are filled with emulsions, newly injected emulsions follow paths that were not explored earlier and find their way to the medium outlet. Interestingly, we find that some entire paths are filled with emulsions (seen in the center of Fig.5.4d) before the flow of emulsions is diverted. Finally, a tortuous path is formed which is followed by newly injected emulsions. We do not observe clogging of the entire medium at the constant injection flow rate and the concentration of the droplets remains to be below a jamming transition. [62] Moreover, the balance between viscous and capillary forces does not change dramatically to mobilize a large number of droplets. [3,32]

To quantify the emerging flow paths within the medium, we track individual emulsions and superimpose the paths taken by these emulsions as shown in Fig.5.5. A few preferential paths are formed in the medium and the subsequently injected emulsions continue flowing along these paths. While only a few tortuous paths are established in the flow of monodisperse emulsions (Fig.5.5a), additional paths are explored by introducing a slight polydispersity in the emulsion sizes (Fig.5.5b). Interestingly, in the experiment with larger and polydisperse emulsions, large droplets squeeze through the pores and create small perturbations in the flow of subsequent trailing droplets. Hence, droplets

are more likely to switch paths as shown in Fig.5.5b.

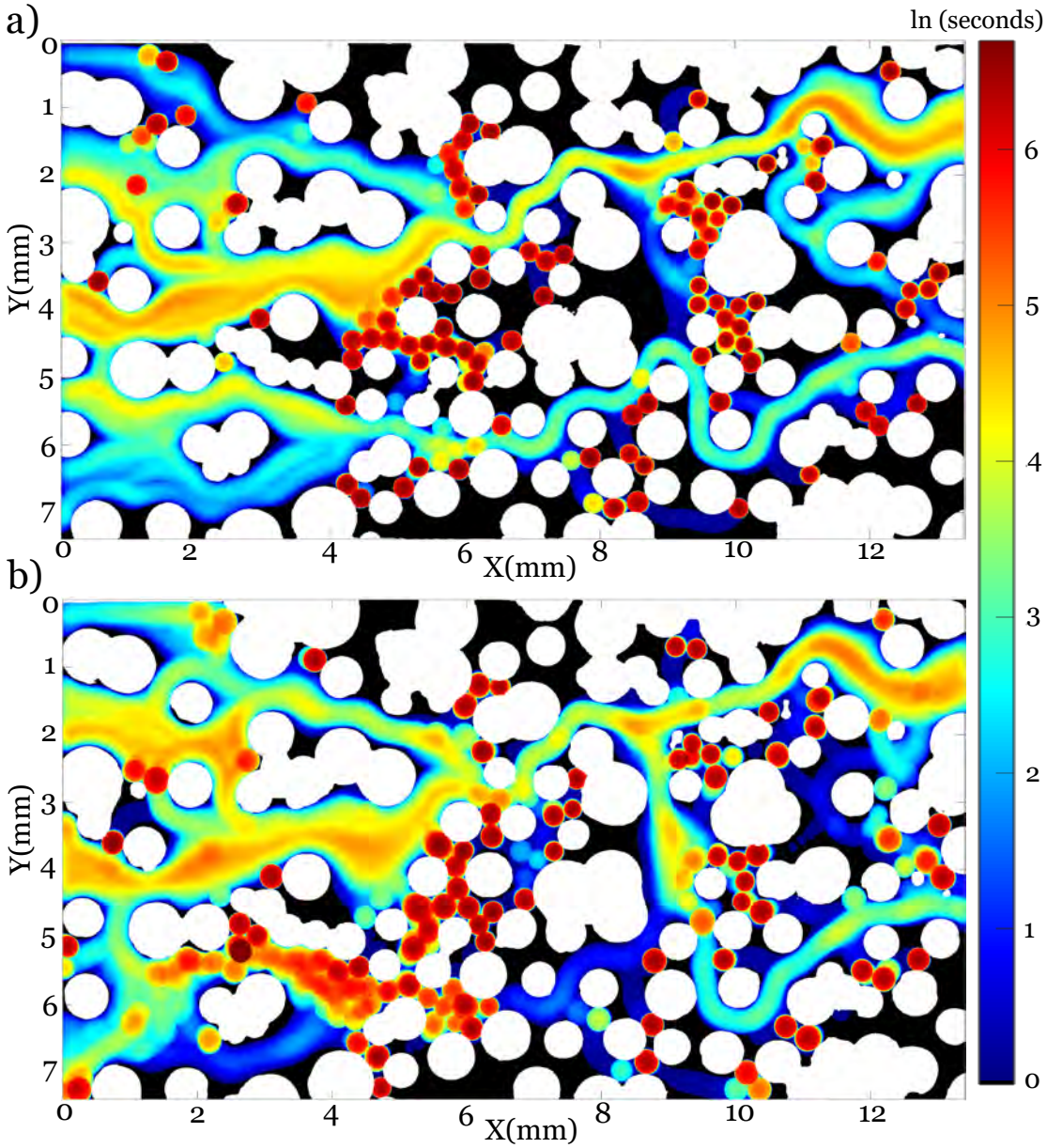

Figure 5.5: Spatial distribution of emulsions in (a) monodisperse (Exp1) and (b) polydisperse (Exp2) experiments. Heatmap represents the log-transformed time (in seconds) spent at each location, normalized to match the maximum time value of Exp2.

To quantify the variability of the velocities of the emulsions, we calculate the probability density function (PDF) of the velocities in different experiments as shown in Fig.5.6a. The PDF of the

magnitude of the velocities of emulsions has an exponential decay with a long stretched tail indicating the presence of rare events with very large velocities compared to the interstitial velocity. The interstitial velocity is $v_{int} = q/\phi$, where q is the volumetric flow rate per cross-sectional area and ϕ is the medium porosity. The distributions of velocities of emulsions have similarities with the PDF of the velocities of the flow of a single-phase continuous fluid, measured in identical but separate experiments using 1μm tracer particles using Particle Image Velocimetry (PIV) . [1, 59] However, the tail of the PDF of the velocities of droplets stretches to much larger velocities ($5\times v_{int}$ than that of the single-phase flow ($3\times v_{int}$).

Comparing the PDF of velocities of droplets with a single-phase flow confirms the intermittency in the dynamics of droplets where trapping, re-mobilization, squeezing and bursts through pore throats are common. The dynamics of emulsions in these experiments exhibit unique features reminiscent of transport in a porous medium: 1) emulsions only pass through certain areas and some pores within the medium are never explored by the droplets, as seen in Fig.5.5. 2) Trapping and accumulation of emulsions within the porous structure result in changes in the medium permeability, leading to an increase in the viscous forces. The latter effect, only observable in pore-level measurements [21,59,91], can significantly change the flow in neighboring pores and consequently affect the global flow. Despite the finite size of the emulsions, and an expected slower velocities than fluid elements (represented as tracers), we find that the PDF of magnitude of the velocities of emulsions has an average comparable to a single phase flow in agreement with the constant flow driven experiment.

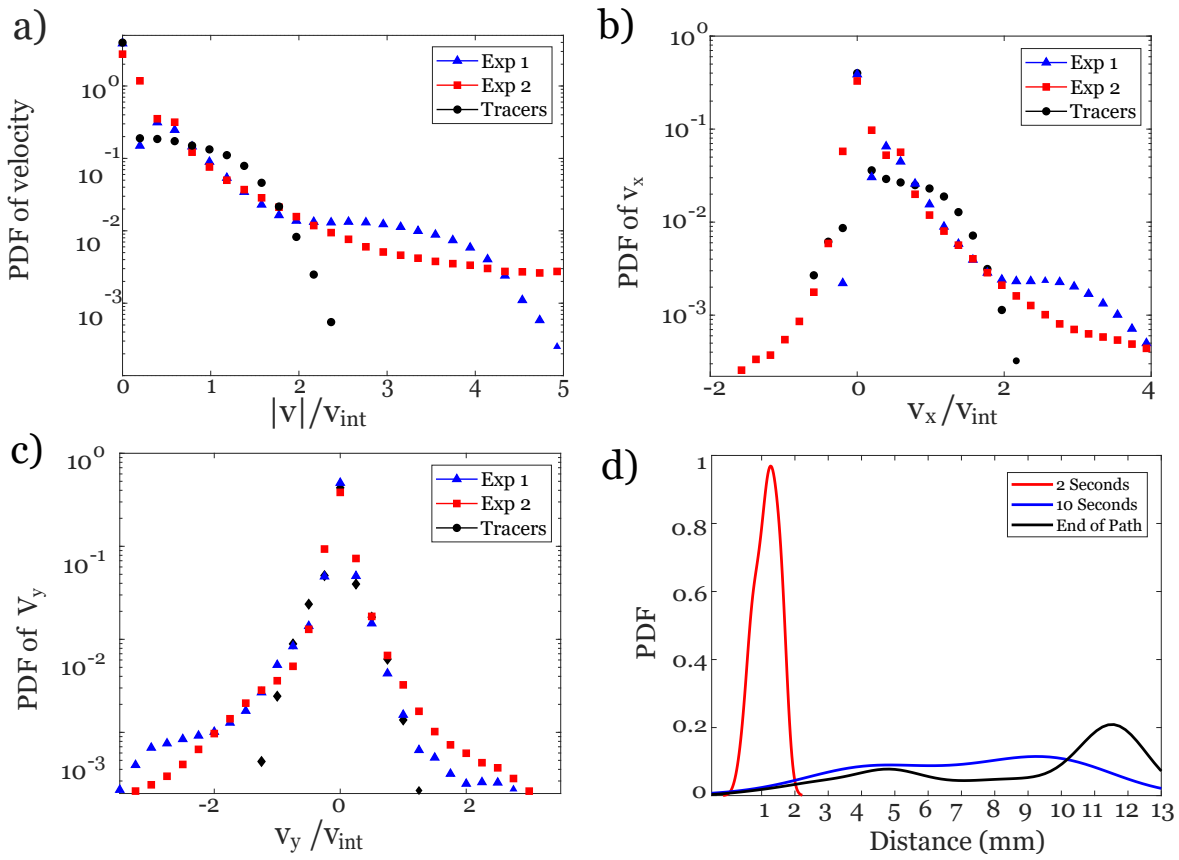

Figure 5.6: (a-c) Probability distribution of velocities of emulsions normalized by the interstitial velocity a) PDf of the magnitude of velocity b) PDF of the longitudinal component of velocity (v_x) c) PDF of the transverse velocity, v_y. Blue triangles represent the monodisperse emulsions, red squares represent the polydisperse emulsions, and black diamonds represent the tracer particles velocities. d) Distribution of the deviation of location of first 100 monodisperse droplets from fluid elements for 3 time-stamps, 2 seconds after entering the medium (red), 10 seconds (blue), and by the time either object reaches the end of their path in view (black).

The PDF of velocities of emulsions in the direction of the imposed flow, Fig.5.6b, has a positive average, $\langle v_x \rangle = 270$ μm/s, consistent with the direction of flow. The significant negative tail in the polydisperse experiments (Exp2) is due to the tortuous path taken by droplets in this experiment. The PDF of v_y of emulsions has a slightly higher probability in the downward ($v_y < 0$) than the upward direction, aligning with the most common paths observed in Fig.5.5. The average dynamics of droplets in these experiments (Exp1: monodisperse and Exp2: polydisperse) are independent of the distribution of droplet sizes. The average velocity is dominated by the large number of droplets experiencing slow dynamics. However, the rare events with large velocities and bursts of motion are more probable in the experiments with more variable sizes of emulsions.

Additional insights into the preferential paths of the droplets can be drawn by comparing the trajectory of a droplet with a fluid element as it enters the medium. The path of a droplet is determined by the local stress (proportional to the velocity gradient) on the surface of the droplet, while the path of a fluid element is dictated by the fluid velocities. Hence, the trajectory of an emulsion droplet deviates from a fluid element due to the finite size of a droplet. The departure of the trajectory of a droplet from fluid elements increases with time as shown in Fig.5.6d. We quantify the distribution of the deviation between the location of the tracers and the emulsions entering the medium at the same initial position. The locations of the tracers are determined by integrating their trajectory using the flow velocity field (from PIV) and a fourth order Runge-Kutta integration scheme. [57] The emulsions closely follow the path taken by a tracer for the first few seconds but the location of the center of the droplet quickly departs from the fluid element. After only 10 seconds the distance between the location of the droplets and fluid elements is distributed evenly across the medium. The distribution of the distances shifts towards larger values and closer to the length of the medium by the time either the emulsion or the fluid element reaches the end of their paths. The distribution is converted into a smooth function using MATLAB Kernel smoothing function estimate for univariate and bivariate data.

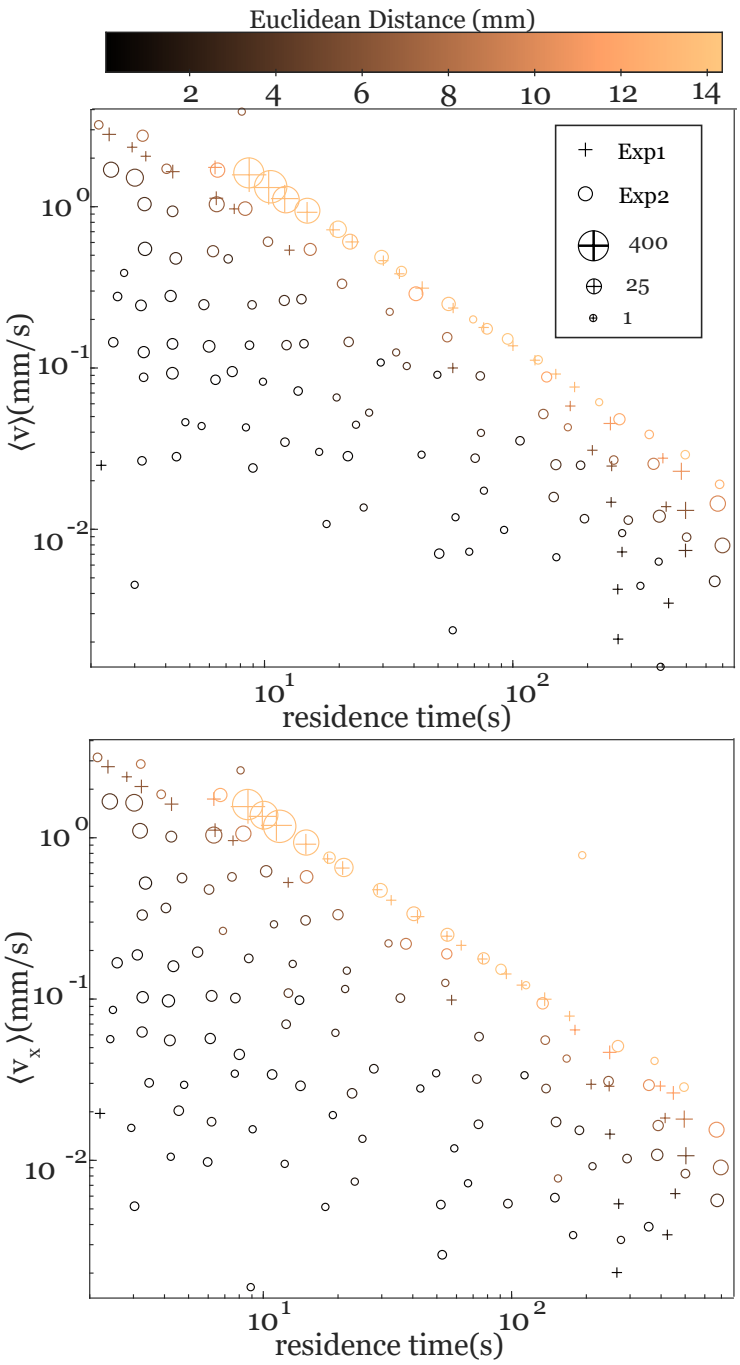

Figure 5.7: Average velocity vs. residence time of emulsions, a) Magnitude of velocity and b) longitudinal component of velocity. Crosses represent the monodisperse (Exp1) data and circles correspond to polydisperse (Exp2) data. Marker sizes represent the number of emulsions within each velocity-residence time bin. The colormap corresponds to the Euclidean distance along the trajectory of the emulsions.

Our understanding of emulsion transport in porous media can be further enhanced by quantify-

ing the dependence of the average velocity of the emulsions on the time of travel through the medium, which we refer to as residence time. As shown in Fig.5.7, the average velocities of all emulsions that pass through the medium scale with the inverse residence time of the emulsions, $\langle v \rangle \sim 1/(resident\ time)$. We measure the residence time of each individual emulsion as it traverses the medium. Emulsions that pass through the medium quickly have a short residence time, while those that become trapped have a much longer residence time. The longest residence time recorded in our experiments is 800 seconds, comparable to the duration of the experiment, and belongs to an emulsion droplet trapped in the medium. The scaling of $\langle v \rangle$ with inverse resident time holds for all emulsions that exit the medium, represented by the light color of the symbols in Fig. 5.7a. The color of the symbols represents the value of the Euclidean distance along the trajectory of the emulsions, defined based on the initial and final locations of each emulsion droplet along its path. The longest Euclidean distance within the 2D porous medium corresponds to the diagonal of the medium (13.2 mm). Interestingly, the scaling of the average velocity is independent of the distribution of the sizes of the emulsions (Exp1, Exp2). Moreover, the longitudinal component of the velocity scales with the residence time similar to those with the average velocity, $\langle v_x \rangle \sim 1/(resident\ time)$. We attribute the $\langle v_x \rangle$ scaling to the dominance of the longitudinal direction in the transport of emulsions within the medium. The transverse velocity, $\langle v_y \rangle$, is an order of magnitude smaller than the longitudinal component in these experiments. The average velocities of the emulsions that are permanently trapped in the medium, or those that do not leave the medium for the duration of the experiment, are smaller than the velocities of emulsions of similar residence time that pass through the medium. Therefore, as illustrated in Fig.5.7, the average velocities of the emulsions that remain within the medium consistently fall below the reference line that encompasses those that pass through it. We observe that droplets with longer Euclidean paths, or equivalently those closer to passing through the medium, are more likely to have an average velocity that approaches the population following the scaling with inverse residence time. Throughout the experiments, we extracted over 6 million positional updates and their corresponding velocities. Therefore, in Figure 5.7, we aggregate numerous data points into a single symbol for better visualization. The symbol's size corresponds to the logarithmic scale of the data point count.

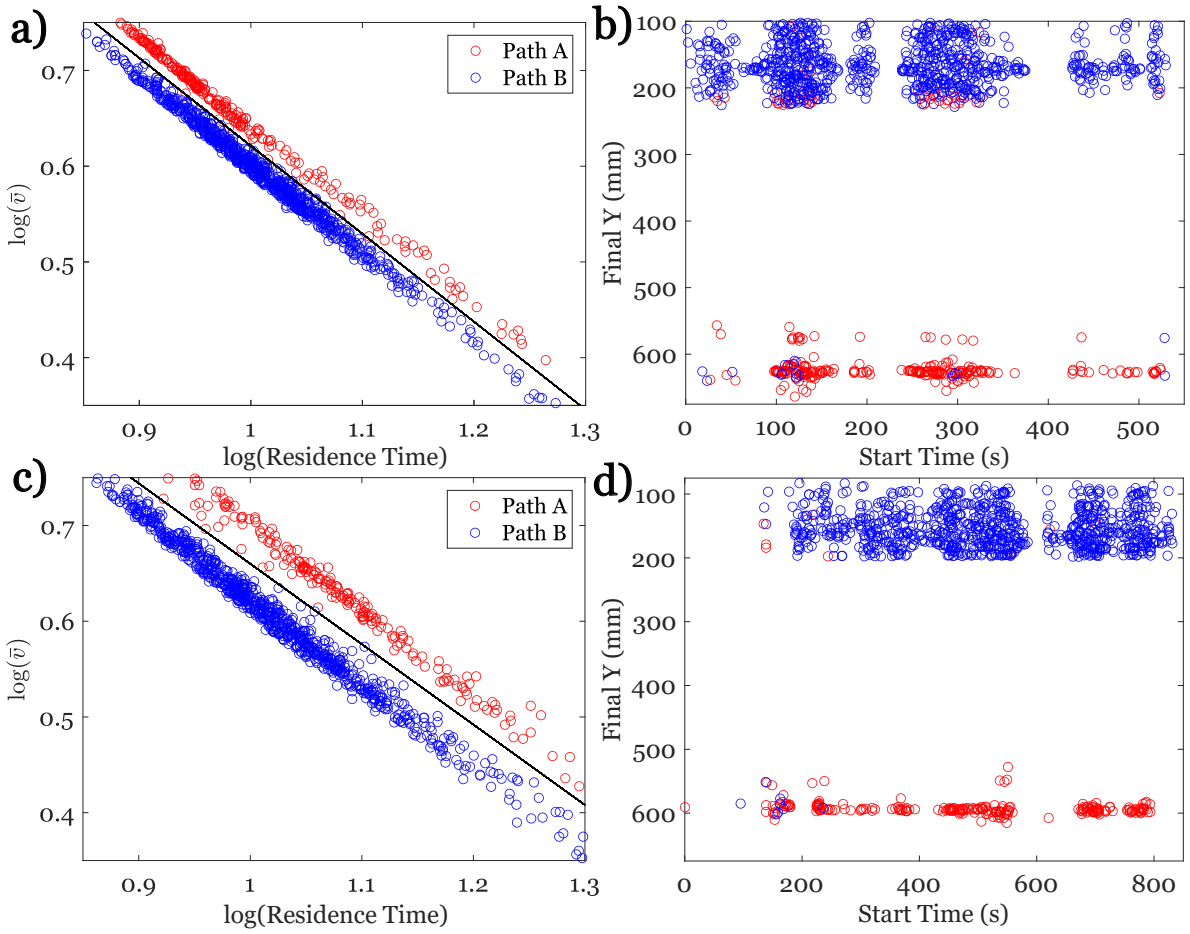

Figure 5.8: Dependence of the average velocity of a) monodisperse and c) polydisperse emulsions on residence time for emulsions that exit the medium. Final exit location of b) monodisperse and d) polydisperse emulsions along the cross sectional direction. Blue symbols represent the path leading to the exit point on top of the medium, red corresponds to the path leading to the bottom of the medium, dashed gray line separates the two populations.

The scaling of average velocity with inverse residence time of emulsions is described with a simple dimensional argument $\langle v \rangle [\frac{m}{s}] = \frac{Length(m)}{res.time(s)}$. We find that the corresponding length scale is the path length of the trajectory of the emulsions. Here, the emulsions are more likely to take either preferential paths identified in Fig.5.5. We identify the emulsions with the paths they take and show that in the monodisperse experiments where emulsions continuously follow two distinct paths, the emulsions on the longer path have a slightly smaller average velocity. Nevertheless, the average velocities of all emulsions are distinctly split into two groups as shown in Fig.5.8a. This observation is further confirmed by the location of the exit point of the emulsions as shown in Fig.5.8b. Moreover, similar separation of path lengths and exit points are observed for the polydisperse emulsions as seen in Fig.5.8c, d. Observation of the distinct paths and exit points in this medium provides clear

evidence of the emergence of preferential paths independent of the emulsion sizes. These paths emerge as a consequence of the solid pore structure modified by the trapping of emulsions.

5.4 Conclusions

In the present study, we successfully investigate the pore-level dynamics of monodisperse emulsions navigating a two-dimensional porous medium. By leveraging the versatility of microfluidic techniques, we control the concentration and sizes of emulsions, in addition to the injection rate of emulsions, by integrating an on-chip drop-maker driven by an external pneumatic pulse. We find that at low concentrations, emulsions flow through pores with higher local velocities and independent of the pore sizes, leading to trapping of emulsions in pores smaller than the emulsion sizes. This leads to a 35% reduction in the porosity of the medium. Few preferential and highly tortuous flow paths emerge within the medium after this reduction in porosity, along which low-concentrations emulsions continue to flow. Our measurements of the pore-level velocities of the emulsions show a highly intermittent dynamic consisting of trapping and subsequent mobilization of emulsions within the porous structure. Nevertheless, we find that the average velocities of all emulsions that flow through the medium scale with the inverse residence time of the emulsions and is distinguished by the flow paths emulsions take within the medium. This emergent scaling holds for slightly polydisperse emulsions.

The introduction of a slight polydispersity in the emulsions enhances the transport of emulsions despite the larger sizes of the droplets revealing more fluctuations in transport paths. Independent of the distribution of droplet sizes, trapped emulsions within the porous structure play a pivotal role in defining preferential transport paths, showcasing the interaction intricacies between the droplets and the porous network. Although the current experiments are focused on the dynamics of low concentrations of emulsions in porous media at a moderately slow flow rate, corresponding to a small Reynolds number, in the laminar regime, the approach serves as a foundational method for characterizing emulsion dynamics in a variety of flow regimes. The formation and persistence of preferential flow paths and droplet-droplet interactions at higher flow rates where the local flow can be highly unstable remains to be explored. These findings and the associated experimental methodology have the potential to drive advancements in areas such as soil remediation, drug delivery, and oil spill cleanup.

Chapter 6

Transport Properties of Emulsions in Porous Media

In this chapter, we investigate the transport properties of emulsions within various 2D porous networks by systematically altering network configurations and assessing their impact on emulsion dynamics. We focus on the role of pore heterogeneity, pore size distribution, and pore connectivity. Specifically, we fabricate these networks through simulations of bead packing, employing both bimodal distributions to mimic physical environments and Gaussian distributions to represent engineered environments, as detailed in the methodology chapter.

Our study examines several key parameters, including the length (ranging from 15 mm to 30 mm) and width (ranging from 7.4 mm to 15 mm) of the device, the porosity of the medium (varying from 52% to 67.9%), and the average pore throat size (ranging from 443 microns to 730 microns). These variations provide quantitative insights into how structural and physical changes influence emulsion behavior within porous media.

Unlike the initial experiments that utilized bimodal bead packs sintered together and scanned using confocal microscopy, the diverse porous networks examined here are created using simulations and packing algorithms developed within this work. This methodological evolution allows for precise control over the network configurations, enabling a comprehensive investigation of their effects on emulsion transport.

Furthermore, we analyze how variations in interfacial tension and droplet deformability influence emulsion dynamics. These factors significantly affect the behavior of emulsions within the porous

networks, providing additional layers of complexity and insight into the transport processes.

The subsequent sections offer a detailed overview of the creation of these porous networks, present the results and analysis, and culminate in a discussion of the findings and their implications. This structured approach enhances our understanding of the interplay between network properties, interfacial tension, and emulsion transport dynamics.

6.1 Creation of Porous Networks

The porous networks were generated using custom simulations and packing codes designed to mimic realistic porous structures. These simulations allowed for the manipulation of network properties such as pore size distribution, connectivity, and overall porosity. The networks were designed to explore the effects of both Gaussian and bimodal distributions of pore sizes, providing a comprehensive range of structural configurations.

To create these networks, spheres were randomly packed within a defined 3D volume. A 2D slice of this 3D arrangement was then selected to represent the porous medium for the microfluidic devices. This method ensured a high degree of control over the structural parameters of the networks, facilitating detailed studies of emulsion dynamics.

Two distributions were used in this study:

- **Gaussian Distribution:** Spheres were packed until a predetermined porosity measurement was achieved, specifically 40% and 60% porosity for both short and long devices.
- **Bimodal Distribution:** An even volumetric distribution was used, meaning the number of beads fit perfectly packed in the same volume were randomly packed. This process continued until packing was complete, after which a slice was taken and scaled to have similar distributions as the initial experiments using scans from physical environments. For this distribution, both narrow and wide devices were created to study the effects of varying width on emulsion transport.

6.2 Network Properties

The generated networks exhibit a range of properties tailored to investigate specific aspects of emulsion transport. Key properties include:

- **Pore Size Distribution:** Networks were created with both Gaussian and bimodal distributions of pore sizes to analyze a range of distributions.
- **Porosity:** The porosity of the networks was varied to examine its influence on emulsion flow and trapping mechanisms.
- **Connectivity:** The connectivity between pores was adjusted to study its impact on the formation of preferential pathways and overall transport efficiency.
- **Length/Width:** The boundary dimensions of the porous networks were altered to see how changes in interstitial velocity and path length may change transport.

Table 6.1 displays these network properties determined via the pore network characterization code developed in the methods section. Although the designs targeted specific porosities (40% and 60%), the final printed devices exhibited slightly higher porosities. This discrepancy is likely due to minor swelling during the 3D printing process. The initial designs were within a few percentage points of the desired values, but final characterization showed slight deviations. The design of 40% porosity will still be referred to as such with the correct porosity listed in table 6.1.

Table 6.1: Network properties of different porous media configurations.

Configuration	Length (mm)	Width (mm)
40 Short	15.5	7.4
40 Long	30.5	7.4
60 Short	15.5	7.4
60 Long	30.5	7.4
Narrow	30	7.4
Wide	30	15

Configuration	Porosity	Avg. Pore Throat (mm)	STD of Pore Throat (mm)
40 Short	0.546	0.537	0.25
40 Long	0.52	0.562	0.253
60 Short	0.679	0.73	0.335
60 Long	0.607	0.69	0.34
Narrow	0.559	0.443	0.26
Wide	0.597	0.466	0.297

Additionally, changes in residency maps, clustering of droplets, probability density functions (PDFs) of velocities, and the transport regime of the emulsions were all analyzed. The mean square displacement (MSD) of the emulsions and their respective anomalous diffusive alphas were also evaluated to categorize transport behaviors. These assist to identify key trends and correlations between network properties and emulsion transport regimes.

6.3 Device Scaling and Dye Contrast Adjustment

The porous media boundaries were increase in size making them twice as wide and long as the original designs. This increase in size necessitated a shift in the dyes used, as fluorescein sodium salt no longer provided sufficient contrast in the larger field of view (FOV) images. Initially, experiments were transitioned to using food dye, which introduced new challenges. The propylene glycol in the food dye affected the interfacial tension between the water and HFE+surfactant, leading to increased deformation of emulsions compared to previous experiments. Along with these increased deformation, it increased the droplets ability to coalescence.

6.4 Detection and Tracking Algorithm Enhancement

The deformation and coalescence of droplets required significant updates to the detection and tracking algorithms. The previous version, which relied on a generalized Hough transform for circular objects, was inadequate for detecting deformed emulsions. To address this, we developed a more complex algorithm incorporating watershed segmentation, morphological operations, and blob analysis. These enhancements improved detection accuracy and tracking efficiency for the new experimental conditions which were not applicable in previous experiments due to the contrast being low.

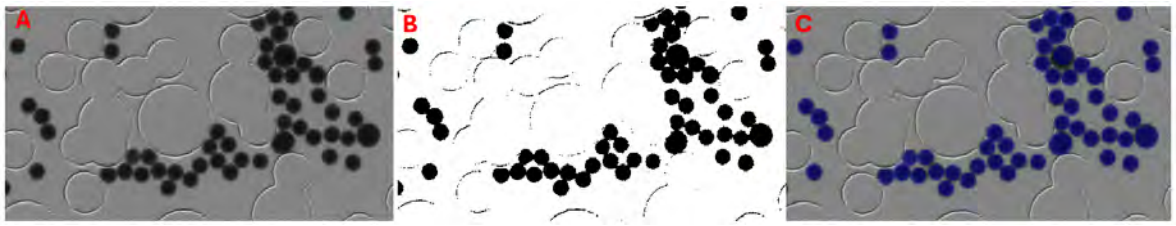

Figure 6.1: Circle Hough Transform Detection Method A) Background Subtraction and stabilization B) Adaptive Binarization C) Circle Hough Transform Detection

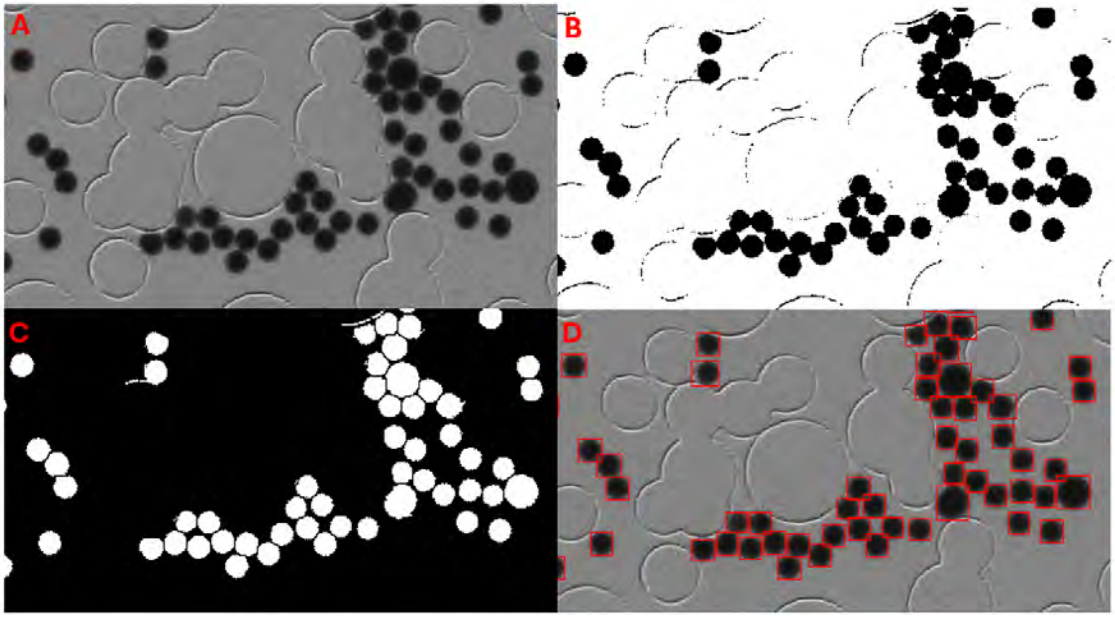

Figure 6.2: Updated Detection Method A) Background Subtraction and stabilization B) Adaptive Binarization C) Morphological and watershed processing D) Detection using Blog Analysis

Despite the updated detection and tracking capabilities, the deformed droplets did not exhibit the preferential pathways observed in earlier experiments. This prompted further adjustments to the experimental design. The porous media and microfluidic devices were initially designed based on a Gaussian distribution of spherical particles. In this design process, spheres were randomly placed in a 3D volume without overlapping, and a 2D slice of this arrangement was used to create the porous structure.

Recognizing that real-world environments often exhibit bimodal distributions, we ran additional simulations using a bimodal distribution to better mimic realistic conditions. This led to the creation of a new porous device. The new experiment featured two configurations: one with the enlarged design printed in its entirety, and another with only the central section of the width printed, maintaining the same length. These configurations aimed to test the impact of increased width and network complexity on preferential path formation as well as have a similar comparison to the initial experiments created from glass beads.

Additionally, food coloring was also altered to remove the propylene glycol from the food dye prior to preparing the emulsions fluid. This resulted in highly contrasted fluid with close interfacial tension to the original experiments. This resulted to less coalescence and a more uniform distribution of droplets and decrease in the emulsions ability to deform easily.

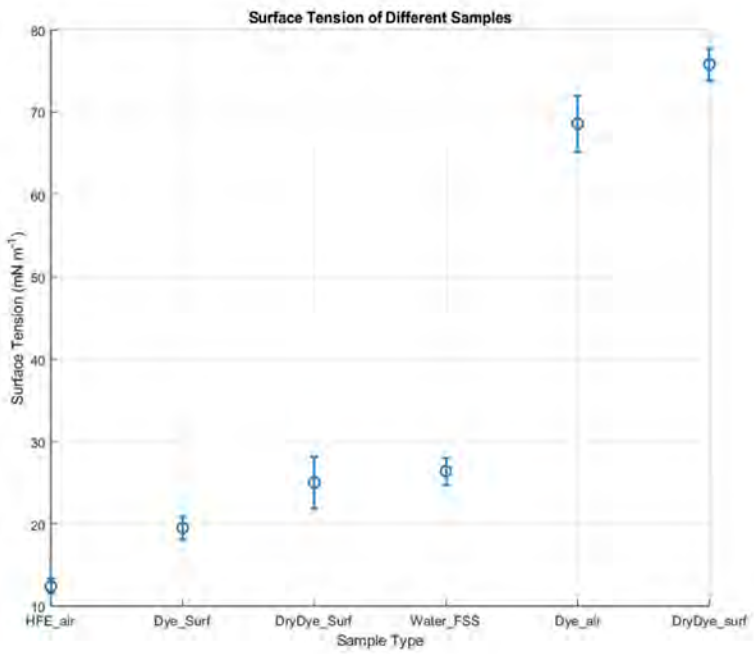

Figure 6.3: Interfacial Tension Samples: HFE & Air, Food Coloring & HFE+Surfactant, Dye (PEG removed) & HFE+Surfactant, Water (FSS) & HFE+Surfactant, Food Coloring & Air, Dye (PEG removed) & Air

Removing PEG from the food coloring results in an interfacial tension much closer to that seen with the previous experiments using FSS as the contrast agent.

6.5 Physical Network and Residency Maps

Residency maps illustrating the physical network and emulsion traversal through various porous media are presented in this section. Analysis of how structural variations affect residency and distribution is performed.

The probability normalization of the data makes it more comparable across the different porous media configurations. Variations in length, width, and porosity affect the traversal time of individual droplets through the medium. Hence, the following residence density maps are normalize by the total time of each experiment to facilitate comparison.

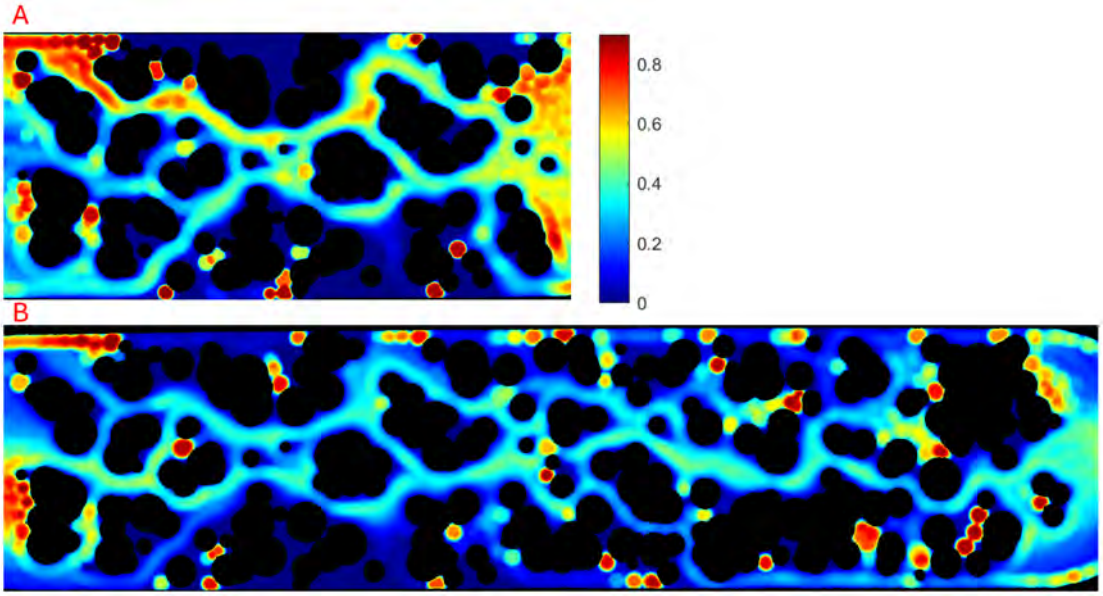

Figure 6.4: Normalized occupancy maps for devices with 40% porosity. (A) Short device. FOV 15.5 x 7.4 mm (B) Long device. FOV 30.5 x 7.4 mm

In the 40% porosity configuration, droplets in the shorter device explore different sections at the bottom of the device, whereas in the longer device, droplets are more evenly distributed. Dominant paths are affected, with the top versus center paths showing variance. In the longer device, most droplets seem to travel towards the center while the short device has a dominant path towards the top, a secondary path at the bottom and third less used path in the center. The edge on the top fills with larger droplets, making the area inaccessible to new emulsions. Notably, for all experiments objects enter the medium uniformly, as designed to avoid bias.

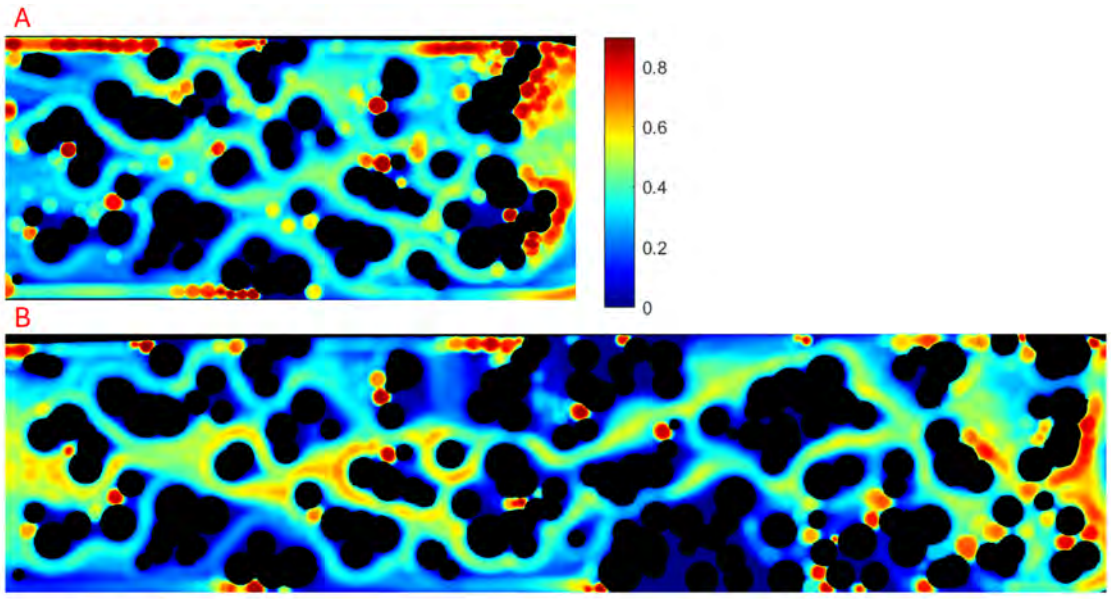

Figure 6.5: Normalized occupancy maps for devices with 60% porosity. (A) Short device. FOV 15.5 x 7.4 mm (B) Long device. FOV 30.5 x 7.4 mm

For the 60% porosity configuration, some droplets hang in the middle for extended periods. Comparing long and short devices, droplets focus more on the center in the long device. This behavior is attributed to the higher porosity, where the fluid separates from the emulsions, which follow the high-velocity stream in the middle. At the outlet, the velocity drops, causing more piling and clustering, with droplets at the cluster edge moving around and being pushed back by passing droplets. Additionally, more intermittent behavior is observed in the short device.

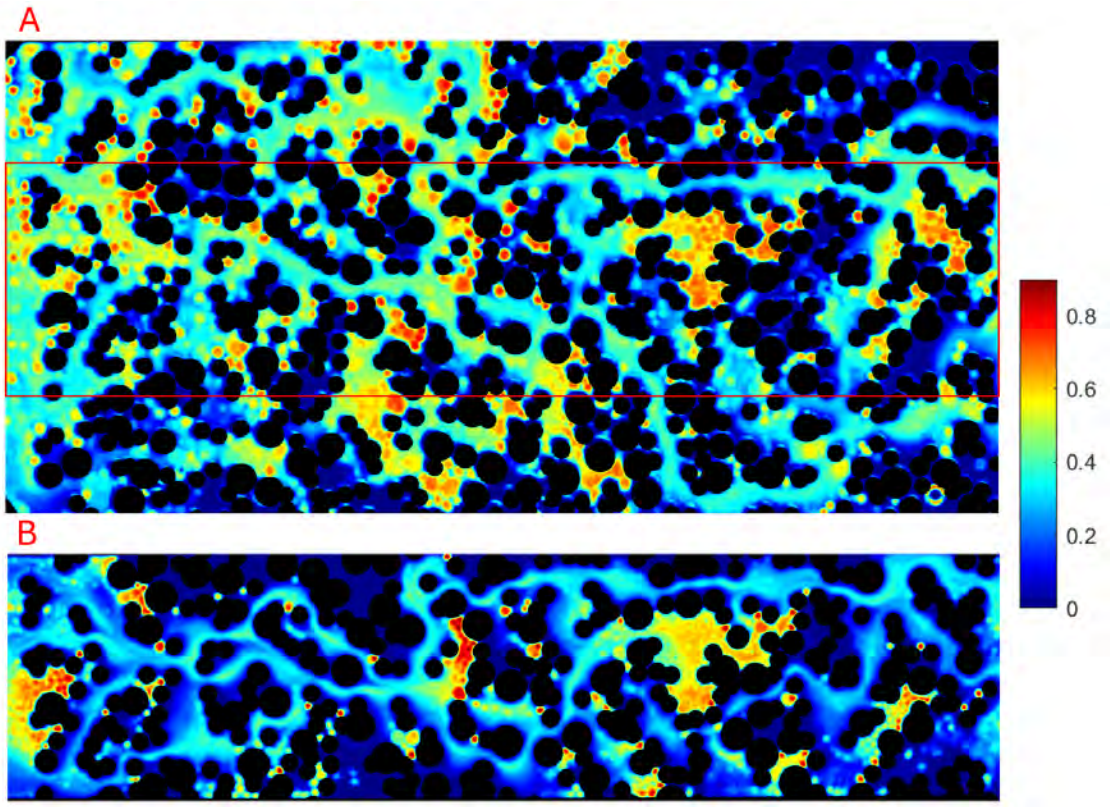

Figure 6.6: Normalized occupancy maps for devices with bimodal packing. (A) Wide device with the red rectangle indicating the narrow device region. FOV 30 x 15mm (B) Narrow device. FOV 30 x 7.4 mm

When examining the width effect, the central pattern remains similar, but with a wider device, droplets form clusters across the entire cross-section. The role of the wall is reduced, allowing droplets to spread more. Pressure measurements show a significant increase in pressure with wider devices, indicating more clustering and reduced permeability. The probability density function (PDF) of average droplet velocities reveals more intermittency in the narrow device, while the wide device exhibits a more uniform velocity distribution.

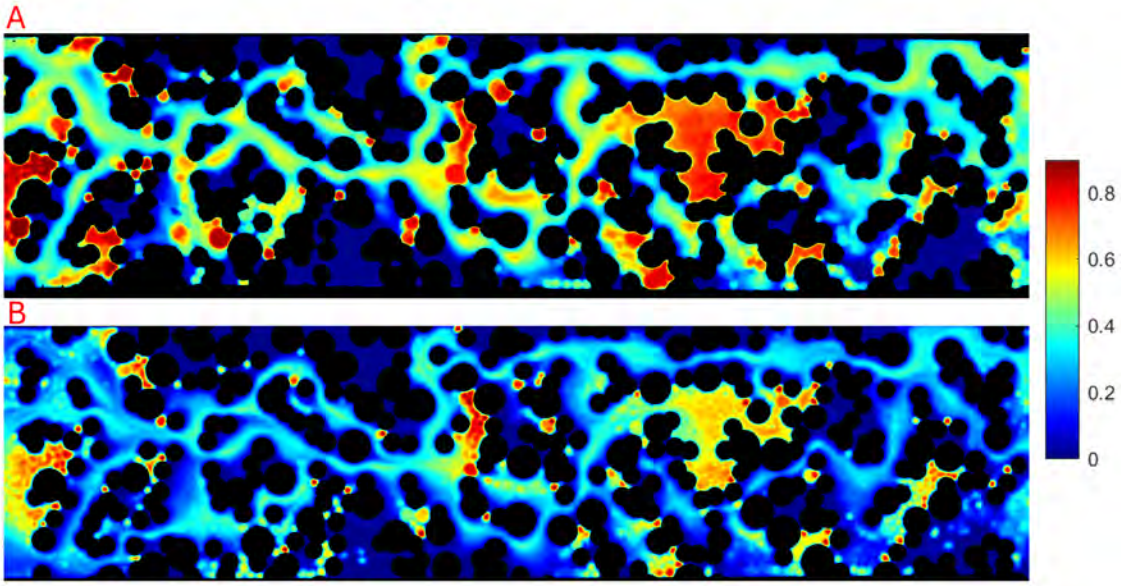

Figure 6.7: Normalized occupancy maps showing the effect of interfacial tension differences. (A) Using dye with propylene glycol. (B) Using dried dye. FOV 30 x 7.4 mm

Regarding the effect of interfacial tension, size and elasticity of the droplets significantly impact stability. Using propylene glycol, lower surface tension leads to merging and polydispersity, as seen in the top map. This merging results in exploring more paths, compared to the dried dye map, where a single path is often explored due to clogging with large droplets. This also leads to slower motion and longer residency times. Clusters form and single paths emerge, consistent with observations across different experiments.

6.6 Pressure Measurements and Experimental Images

The pressure measurements recorded during each experiment are displayed, along with example images captured at select times. These images illustrate the emulsion behavior and the impact of varying physical network configurations on pressure dynamics. By connecting the pressure measurements to the observed emulsion behavior, additional insight of the interplay between emulsion transport and pressure changes within the porous media is gained.

During each experiment, pressure measurements were continuously recorded using a high-precision pressure transducer connected to the microfluidic device. These measurements allowed us to monitor the pressure fluctuations and identify correlations between pressure changes and emulsion dynamics.

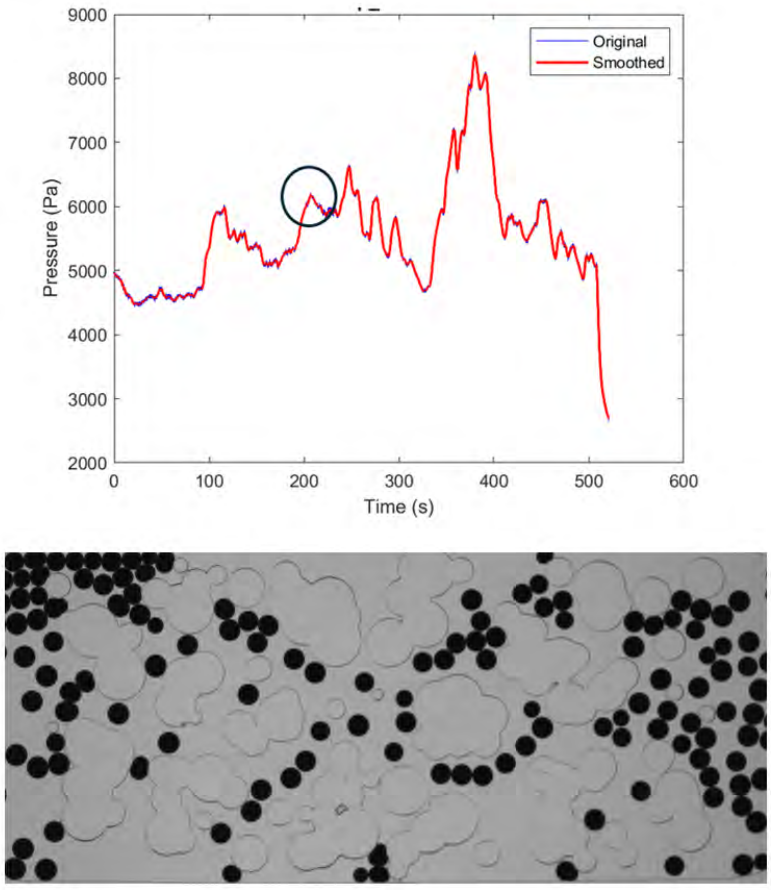

Figure 6.8: Pressure measurements and experimental images for 40% porosity short device. FOV 15.5 x 7.4 mm

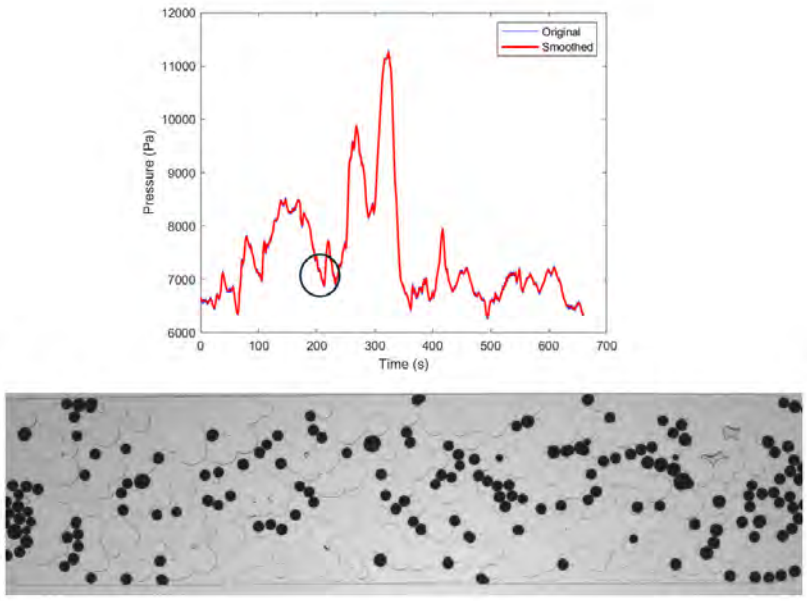

Figure 6.9: Pressure measurements and experimental images for 40% porosity long device. FOV 30.5 x 7.4 mm

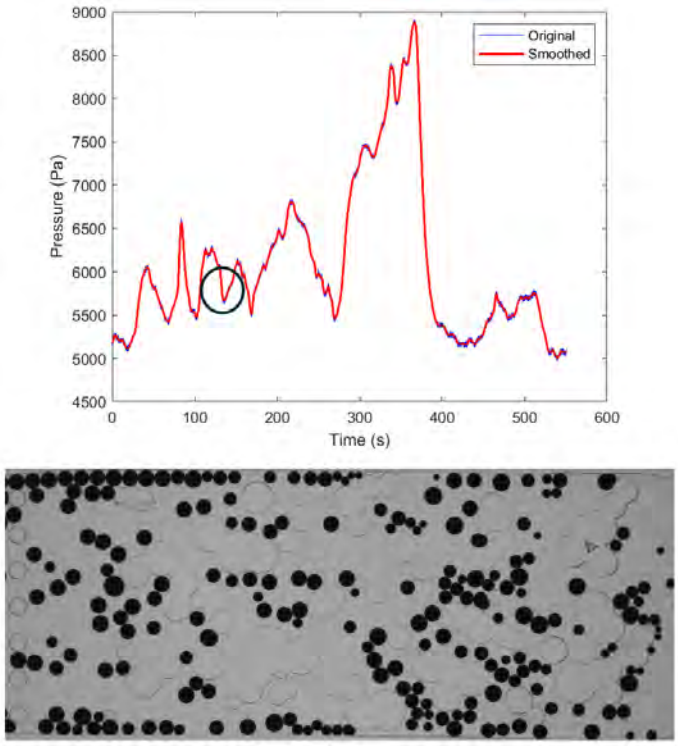

Figure 6.10: Pressure measurements and experimental images for 60% porosity short device.FOV 15.5 x 7.4 mm

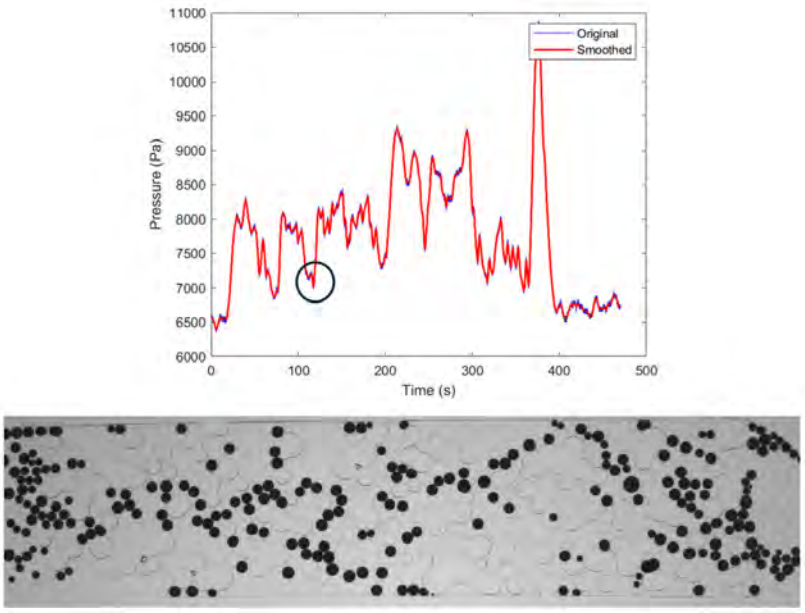

Figure 6.11: Pressure measurements and experimental images for 60% porosity long device. FOV 30 x 7.4 mm

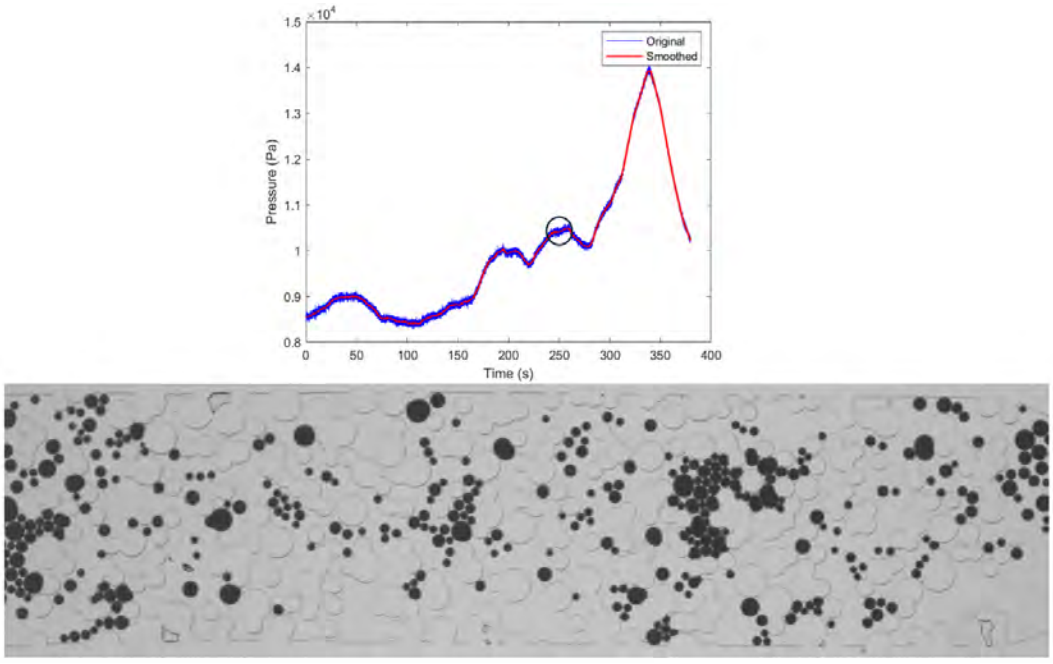

Figure 6.12: Pressure measurements and experimental images for interfacial tension differences using propylene glycol.FOV 30 x 7.4 mm

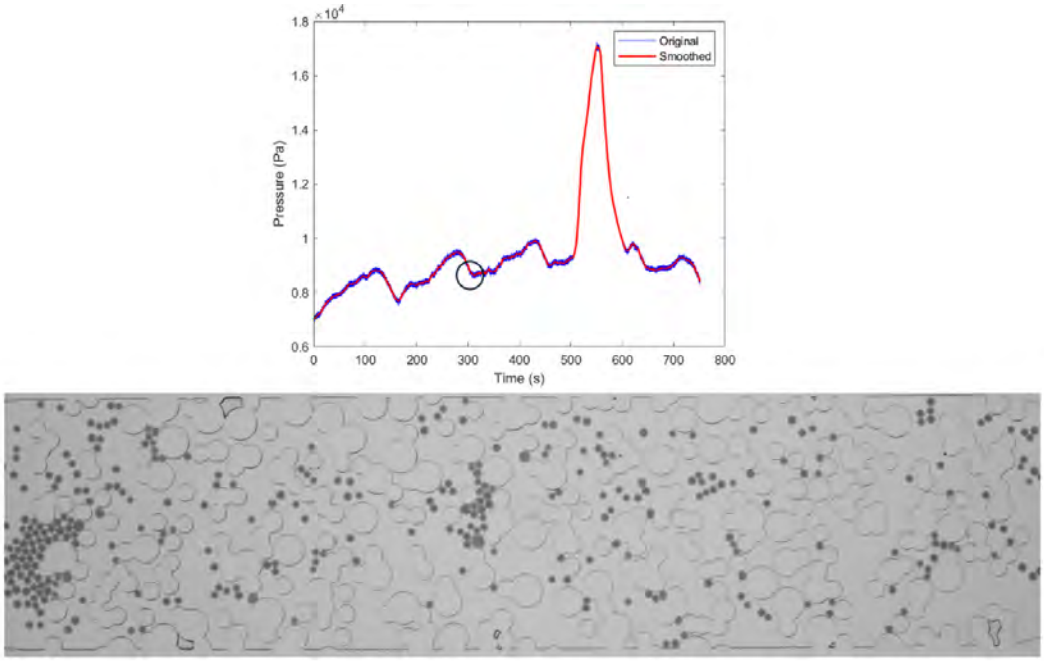

Figure 6.13: Pressure measurements and experimental images for interfacial tension differences using dried dye. FOV 30 x 7.4 mm

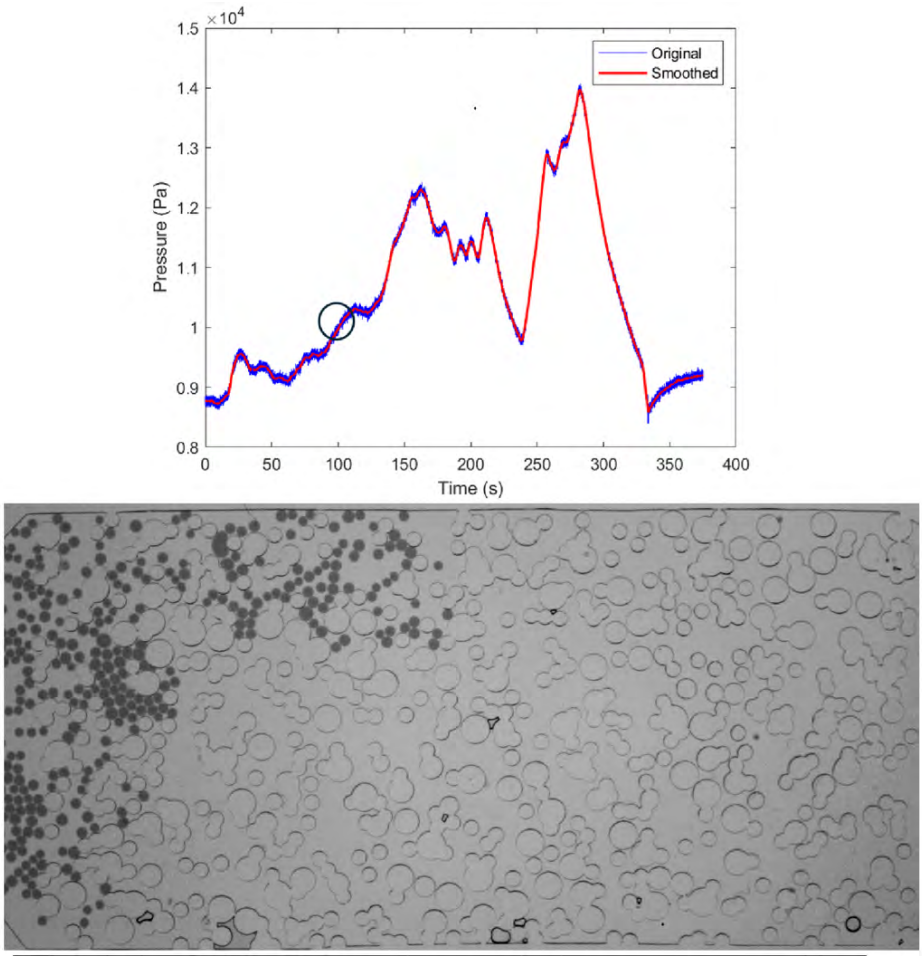

Figure 6.14: Pressure measurements and experimental images for the wide device. FOV 30 x 15 mm

6.7 Results and Analysis

6.7.1 Velocity Distributions

To facilitate a comprehensive comparison of the experiments, the probability density function (PDF) of all velocities for all emulsions across all experiments is plotted. As anticipated, the majority of droplets exhibit small velocities near the injection rate, with some zero values indicating droplets that remain trapped for extended periods. Nevertheless, all experiments also show instances of small populations with exceptionally high velocities.

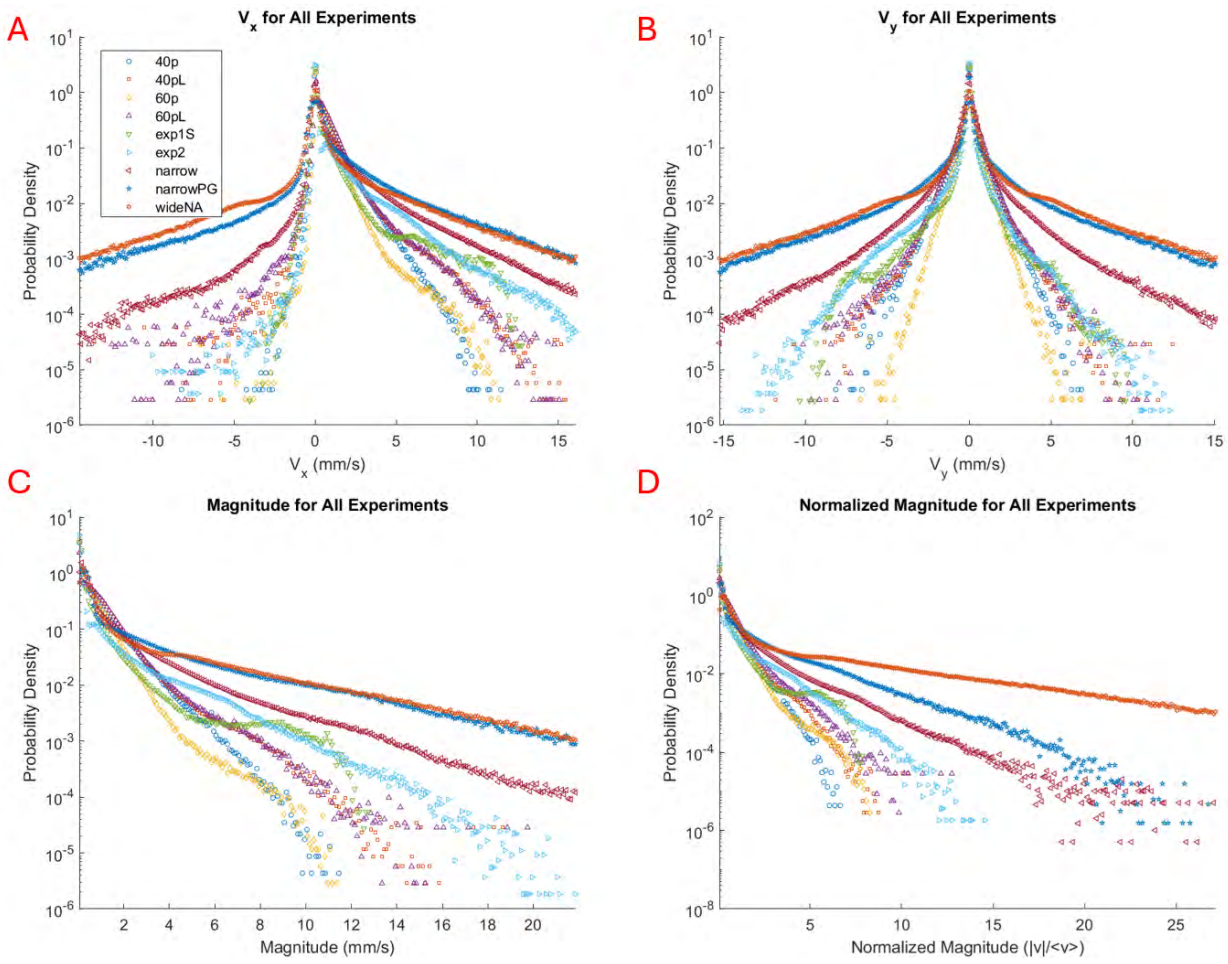

Figure 6.15: Velocity distributions for all experiments: (A) Velocity in the x-direction (V_x), (B) Velocity in the y-direction (V_y), (C) Magnitude of velocity ($|V|$), and (D) Normalized magnitude of velocity ($|V|$), normalized by $\langle V \rangle = Q/(A \cdot \phi)$. Velocities are shown in units of mm/s. The plot highlights the differences in velocity profiles across various porous media configurations.

In the normalized velocity distributions (Figure 6.15D), it is observed that:

1. For the 40% porosity (short and long), the velocities drop fastest, indicating less clustering and more straightforward passage of emulsions through the medium.

2. The longer versions of these configurations shift slightly to higher normalized magnitudes compared to their shorter counterparts.

3. Comparing monodisperse to polydisperse emulsions, as discussed in previous studies, similar patterns emerge with a slight increase in velocities for polydisperse emulsions due to increased deformability and bursts through smaller pores.

4. In the narrow versus narrow with propylene glycol (PG), the higher deformability of droplets leads to increased velocities as they navigate and burst through smaller pores.

5. Comparing wide versus narrow configurations, the wide device shows a small divot in the initial distribution, indicating more diffusive emulsions at lower velocities and increased clustering. The higher velocities in the wide device suggest more frequent bursts through additional pores.

Interestingly, the PG and wide configurations show similar profiles in V_x (Figure 6.15A), V_y (Figure 6.15B), and $|V|$ (Figure 6.15C), but diverge when normalized. This indicates that despite the geometric similarities, the deformability induced by PG significantly impacts the emulsion dynamics. More similarities are observed between the PG and wide configurations than between the narrow and narrow PG setups. Baseline pressures for the wide and PG configurations are larger than the narrow configuration which may lead to a higher number of bursting events.

The analysis indicates that while most droplets exhibit low velocities, a significant number of high-velocity events highlight the complex interplay between emulsion size, deformability, and porous media structure.

Average Velocity of Emulsions

This section discusses the distribution of average velocity for each emulsion droplet across different experiments and porous media configurations. By examining the Probability Density Function (PDF) tails and central peaks, we can draw comparisons and understand the effects of varying porosity, device length, and device width on emulsion transport.

Porosity Changes: When comparing devices with different porosities (Figure 6.16), the lower porosity device exhibits a longer tail towards higher velocities. This is due to more burst events through smaller pore throats and higher pore velocities resulting from the reduced overall volume, which increases flow rates through the existing pores. In the longer devices, the tails of the velocity distributions converge, with the bulk of velocities shifting slightly to the right in the lower porosity device. This indicates that emulsions in lower porosity media travel at higher velocities overall. Additionally, an extra peak at low velocities is observed in the lower porosity device, attributed to clustering, which is less prevalent in the higher porosity (60%) device.

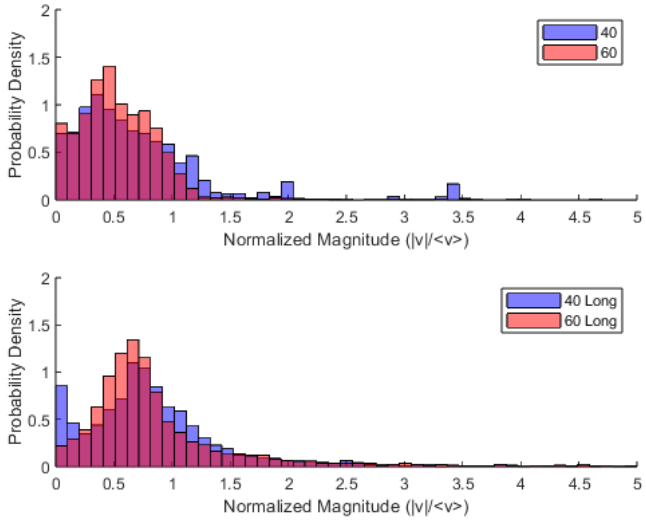

Figure 6.16: Distribution of average velocity for emulsions in devices with varying porosity. (A) 40% vs. 60% porosity. (B) 40% long vs. 60% long.

Changes in Length: Comparing the average velocity distribution of emulsions in devices of varying lengths but similar porosity (Figure 6.17), we observe a shift towards higher velocities in the longer devices. In the 60% porosity devices, this shift is more pronounced, but there is no secondary peak near zero velocity, indicating the absence of large clusters. For the 40% porosity devices, the shift is smaller but noticeable, with the secondary peak due to emulsion clustering with near-zero velocities.

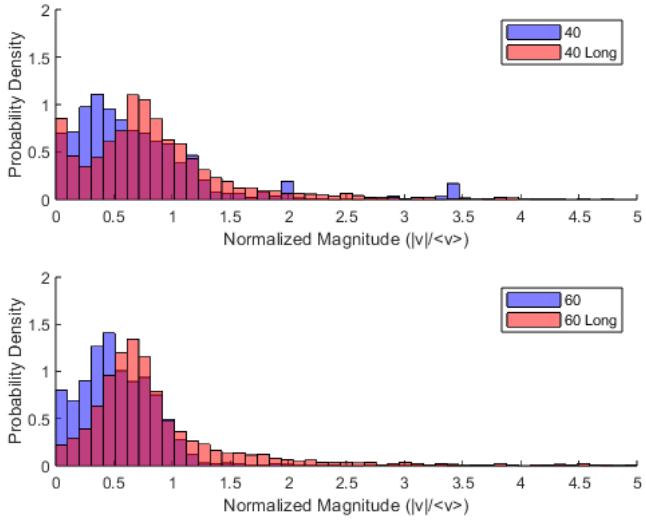

Figure 6.17: Distribution of average velocity for emulsions in devices with varying lengths. (A) 40% porosity short vs. long. (B) 60% porosity short vs. long.

Narrow vs. Wide: When comparing narrow and wide devices (Figure 6.18), the narrow device exhibits a longer tail towards higher velocities, with a subtle peak at low velocities and another around 1, similar to the 40% long device with comparable porosity. The wide device, however, shows a shorter tail and a single peak at a much lower velocity (0.25). This difference is likely due to the emulsions acting in a more diffusive regime in the wider device, with more space for exploration and less time spent in clusters. Interestingly, despite some clustering, there are no significant peaks near zero, possibly due to the continuous reshuffling of droplets within clusters.

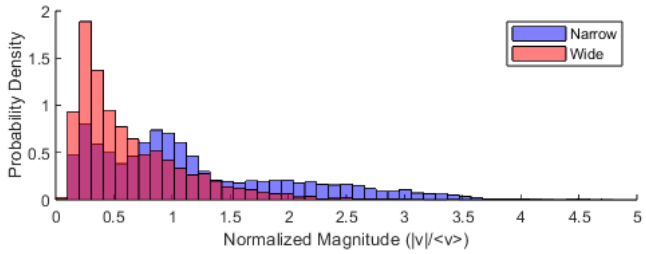

Figure 6.18: Distribution of average velocity for emulsions in narrow vs. wide devices.

6.7.2 Mean Square Displacement (MSD) and Regime Analysis

Introduction

In this section, we aim to quantify the transport regimes within porous media by analyzing the Mean Square Displacement (MSD) of emulsion droplets. This analysis enables us to distinguish between diffusive, advective, and anomalous transport behaviors.

Mean Square Displacement (MSD) Analysis

The MSD is defined as:

$$\mathrm{MSD}(t) = \langle [x(t) - x_0]^2 \rangle \tag{6.1}$$

where $x(t)$ denotes the position of the emulsion droplet at time t, and the brackets indicate an average over the entire path.

To determine the transport nature, we examine the log-log plots of MSD as a function of time. The slope of these plots, denoted as α, characterizes different transport regimes:

- $\alpha \approx 1$: Diffusive transport, indicative of random motion following Fick's law.
- $\alpha > 1$: Superdiffusive transport, suggesting directed or advective motion often due to external forces.
- $\alpha < 1$: Subdiffusive transport, where motion is hindered, possibly by obstacles or binding interactions.
- $\alpha = 2$: Ballistic transport, indicating constant velocity motion.

Alpha Distribution and Its Significance

Before discussing the distribution of α values, it is crucial to understand their derivation from the MSD analysis. By fitting the MSD data to a power-law function $\text{MSD}(t) \propto t^{\alpha}$, we obtain the α values for different experimental conditions.

The distribution of α values provides insights into the heterogeneity of transport regimes within the porous media. This analysis helps identify the prevalence of different transport behaviors under varying network configurations, such as changes in network width, porosity, and pore throat size.

Equations and Theoretical Background

The MSD can be described by the equation:

$$\text{MSD}(t) = Kt^{\alpha} \tag{6.2}$$

where K is a proportionality constant and α is the exponent characterizing the transport regime.

We will explore the distribution of α values to understand how different structural parameters of the porous network influence emulsion transport. Analyzing the α distribution reveals the diversity in transport behaviors and highlights regions with predominant subdiffusive, diffusive, or superdiffusive dynamics.

Visualizing Transport Regimes

To visually illustrate the different transport regimes, consider the following diagram from Wikipedia, which depicts anomalous diffusion and the corresponding α values:

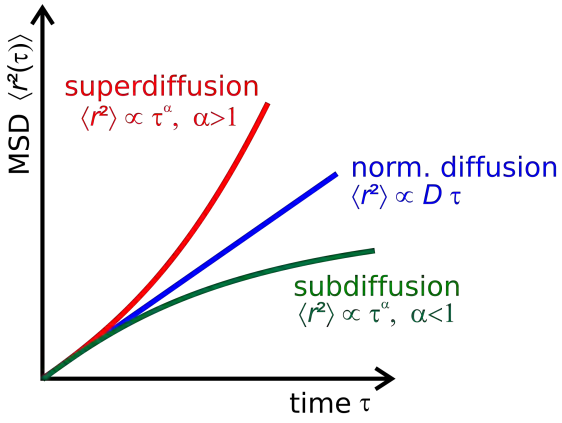

Figure 6.19: Illustration of transport regimes for anomalous diffusion.

Rationale for Analyzing Alpha Distributions

By examining the distribution of α values, we gain a comprehensive understanding of the transport dynamics within the porous media. This analysis reveals how different physical properties of the network, such as pore size and connectivity, influence the movement of emulsion droplets. Understanding these dynamics is crucial for applications in enhanced oil recovery, drug delivery, and other fields where transport through porous media is relevant.

6.7.3 Results and Discussion

The following section will present the distribution of α values obtained from our experiments, providing a detailed analysis of how network properties affect transport regimes. This discussion will highlight the implications of our findings for the design and optimization of porous media in various applications.

Alpha Distribution and Analysis

Building on our analysis of the Mean Square Displacement (MSD), we now delve into the distribution of α values to further elucidate the transport regimes within the porous media. By fitting the MSD data to a power-law function $\text{MSD}(t) \propto t^{\alpha}$, we derive the α values for various experimental conditions.

Analyzing the distribution of α values enables us to evaluate the heterogeneity in transport behaviors and identify the prevalence of specific regimes under various network configurations. This

analysis involves examining the influence of parameters such as network width, porosity, and average pore throat size on the transport dynamics.

Additionally, we note that some large α values (greater than 2) can be attributed to complex interactions such as complex flow patterns, particle-particle interactions, particle-pore interactions, and burst events where emulsion droplets accelerate through narrow pores. These factors introduce complexities that can impact our measurements and interpretations.

Understanding these complexities is essential for accurately interpreting the results and their implications for practical applications. Insights gained from the α distribution analysis are crucial for comprehending how different physical properties of the network influence the movement of emulsion droplets. This knowledge is vital for optimizing the design of porous media for various industrial and scientific applications, such as enhanced oil recovery and targeted drug delivery systems.

In the subsequent section, we present the detailed results of the α distribution analysis. We highlight how network properties affect transport regimes and discuss the broader implications of our findings.

For the 40% porosity device (Figure 6.20A), the alpha distribution shows that the majority of emulsions fall within the superdiffusive regime (86.89%), with a smaller percentage in the subdiffusive (9.37%) and ballistic (3.75%) regimes. This indicates that most emulsions in this network experience higher velocities, likely due to burst events through smaller pore throats. The long version of the 40% porosity device (Figure 6.20B) exhibits a similar trend with slightly higher subdiffusion (10.84%) and lower ballistic motion (1.7%), suggesting more consistent high-velocity transport over longer distances and a tendency for some emulsions to be trapped longer, forming clusters.

The 60% porosity device (Figure 6.20C) displays an even higher proportion of emulsions in the superdiffusive regime (90.49%) and fewer in the subdiffusive (5.68%) and ballistic (3.88%) regimes. This reflects the simpler network structure with fewer obstacles, allowing more straightforward flow paths. The long version of the 60% porosity device (Figure 6.20D) maintains this pattern with slightly increased subdiffusion (6.65%) and ballistic motion (4.55%), indicating a stable and efficient emulsion transport through a less complex network.

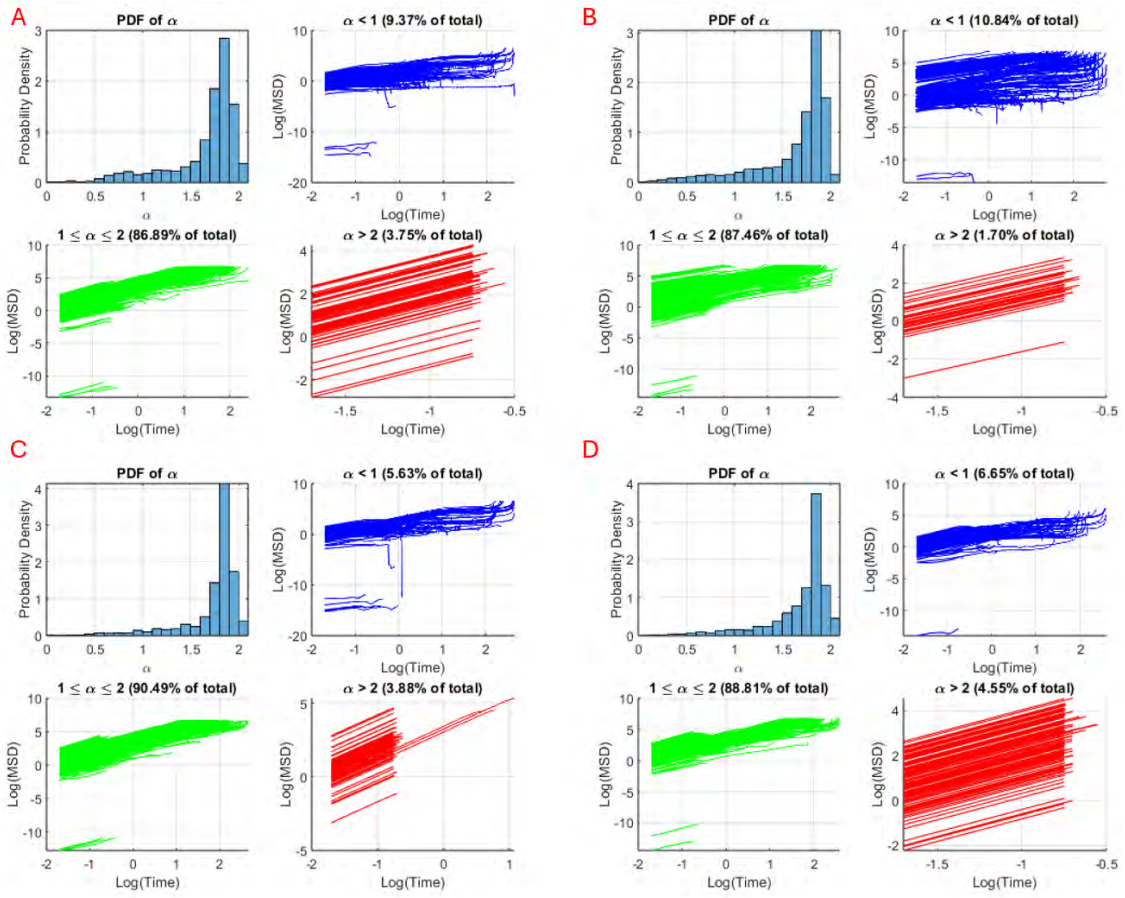

Figure 6.20: Alpha distributions and MSD vs time plots for varying porosity devices. (A) 40% porosity, (B) 40% porosity long, (C) 60% porosity, (D) 60% porosity long.

When comparing monodisperse (EXP1) and polydisperse (EXP2) emulsions (Figure 6.21 A and B respectively), the monodisperse emulsions show a larger proportion in the subdiffusive regime (19.81%), indicating more trapping and slower transport. The polydisperse emulsions (EXP2) exhibit increased superdiffusive behavior (88.86%), suggesting that size variability aids in navigating the porous media, reducing clogging, and enhancing overall transport efficiency.

In the comparison of narrow versus wide devices (Figure 6.21 C and D respectively), the narrow device displays a significant portion in the superdiffusive regime (81.47%) and a smaller subdiffusive component (18.53%). The wide device, however, shows a substantial increase in subdiffusive behavior (48.01%), indicative of more space allowing emulsions to diffuse slowly and form clusters less frequently. This supports the earlier observation that wider devices enable more diffusive regimes due to the larger exploration area and reduced clustering, resulting in lower overall velocities.

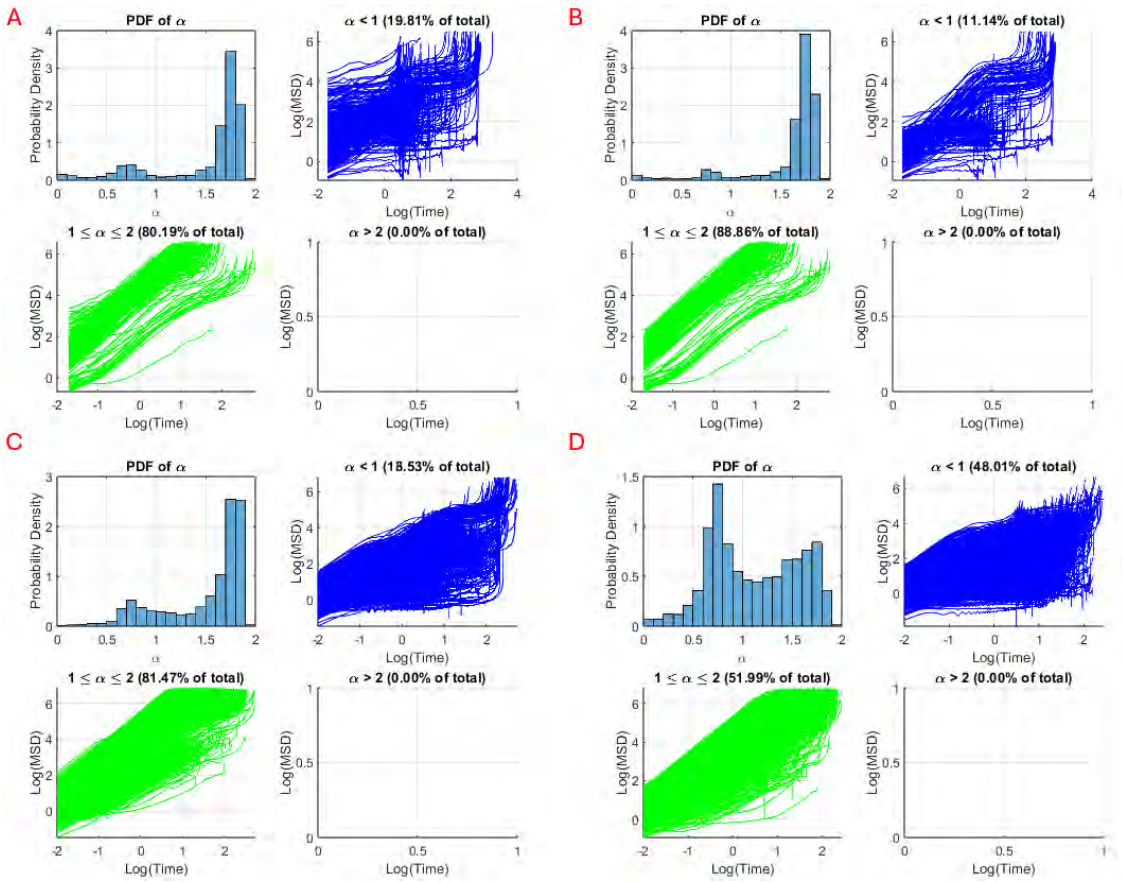

Figure 6.21: Alpha distributions and MSD log-log plots for varying emulsion types and device widths. (A) Monodisperse (EXP1), (B) Polydisperse (EXP2), (C) Narrow, (D) Wide.

The systematic analysis of alpha distributions and MSD versus time log plots reveals that the transport properties of emulsions are significantly influenced by the porosity, length, and width of the porous media. Lower porosity devices enhance the velocity of emulsions due to increased pore velocities and more frequent burst events as emulsions navigate smaller pore throats. Polydisperse emulsions exhibit more burst events as well as unclogging and clogging events, while monodispersed emulsions quickly reach a stable regime without significant changes. The variation in polydisperse emulsions allows for the shuffling of clustered or trapped emulsions and enables them to pass through pores that monodisperse emulsions would typically not traverse. Longer devices are inherently more complex, which can lead to increased clustering and higher pore velocities as certain paths become blocked. Narrow devices promote superdiffusive transport, whereas wider devices allow for more diffusive behavior, reducing overall emulsion velocities and clustering.

These findings enhance our understanding of emulsion transport in porous media, emphasizing the critical role of network structure and emulsion properties in determining transport regimes. Future research can build upon this to explore more complex configurations and their implications for

various applications, such as enhanced oil recovery, soil remediation, and drug delivery systems.

6.8 Conclusion

This chapter has examined the transport properties of emulsions in diverse porous media, elucidating how the structural characteristics of the porous networks and the properties of the emulsions influence their movement and transport regimes. By varying the porosity, length, and width of the devices and analyzing the impacts on emulsion transport, the study reveals several key insights into emulsion dynamics within porous structures.

The creation of different porous networks through random packing simulations allowed for precise control over structural parameters, facilitating detailed studies. The analysis of normalized residency maps showed how structural variations impact emulsion distribution and residency time. Shorter devices exhibited distinct sections of emulsion exploration, while longer devices displayed more evenly distributed paths, influenced by higher velocities and less clustering in higher porosity media.

The examination of pressure measurements and example images highlighted the effects of interfacial tension on emulsion stability and transport. Lower interfacial tension, achieved by removing propylene glycol, reduced droplet deformability and polydispersity. Wider devices allowed emulsions to diffuse more freely, reducing clustering and maintaining lower velocities compared to narrower devices.

The velocity distribution analysis further emphasized the differences across experiments. Lower porosity devices showed longer tails towards higher velocities due to increased burst events, while higher porosity devices displayed slower average velocities. Longer devices shifted the velocity distribution towards higher values, especially in lower porosity setups, where clustering significantly influenced transport dynamics.

The analysis of α distributions and Mean Square Displacement (MSD) log-log plots reveals distinct differences between natural and artificial porous media. Artificial porous media exhibit a wider range of transport regimes, including instances of $\alpha > 2$, signifying ballistic or hyper-ballistic transport. This behavior is not observed in natural porous media, which tend to pack more closely, as demonstrated in Figure 21. The closer packing in natural porous media restricts the occurrence of ballistic transport, resulting in more stable and predictable emulsion movement.

Natural porous media, with their inherent structural complexity and closer packing, facilitate more stable and predictable emulsion transport, reducing instances of high-velocity, ballistic behavior. In contrast, artificial porous media, which can be engineered with varying porosity and structure, allow for more diverse transport regimes, including enhanced ballistic transport due to less constrained pore pathways.

The MSD and alpha distribution analysis elucidates the transport regimes observed. Most emulsions exhibited superdiffusive behavior, with polydisperse emulsions showing more dynamic transport through unclogging and clogging events. Narrow devices promoted superdiffusion, while wider devices facilitated more diffusive transport, highlighting the role of spatial dimensions in emulsion dynamics.

In summary, this chapter demonstrates that the transport properties of emulsions in porous media are intricately linked to the structural characteristics of the porous network and the properties of the emulsions. The findings underscore the importance of considering these factors in designing and optimizing processes that rely on emulsion transport, such as enhanced oil recovery, soil remediation, and drug delivery systems. Future research should continue to explore these relationships in more complex configurations to further advance the understanding of emulsion dynamics in porous media.

Chapter 7

Machine Learning in Emulsion Transport

7.1 Introduction

The study of emulsion dynamics necessitates a refined approach to predict the movement of droplets through a medium. Droplets in the previously mentioned experiments typically follow one of two preferred paths, become stuck in the media, or are still traveling through the media. Employing machine learning techniques enhances our understanding and classification of these droplet tracks. This chapter discusses the methodology used for predicting droplet tracks through data preprocessing, feature extraction, and machine learning.

7.2 Data Preprocessing and Map Creation

Initially, we begin with the track map containing droplet data that was created from the tracking frame data. Each key in the map represents an emulsion that was tracked comprising it's positional and velocity information over time. The first step involves filtering this map to create a new map which contains only droplets with at least 350 data points. This ensures the maps that are being used in the machine learning algorithm has sufficient data points for meaningful predictions. The data used here is introduced in my latest paper. [**?**] Fig. 7.1 displays the trajectory information taken from similar experiments.

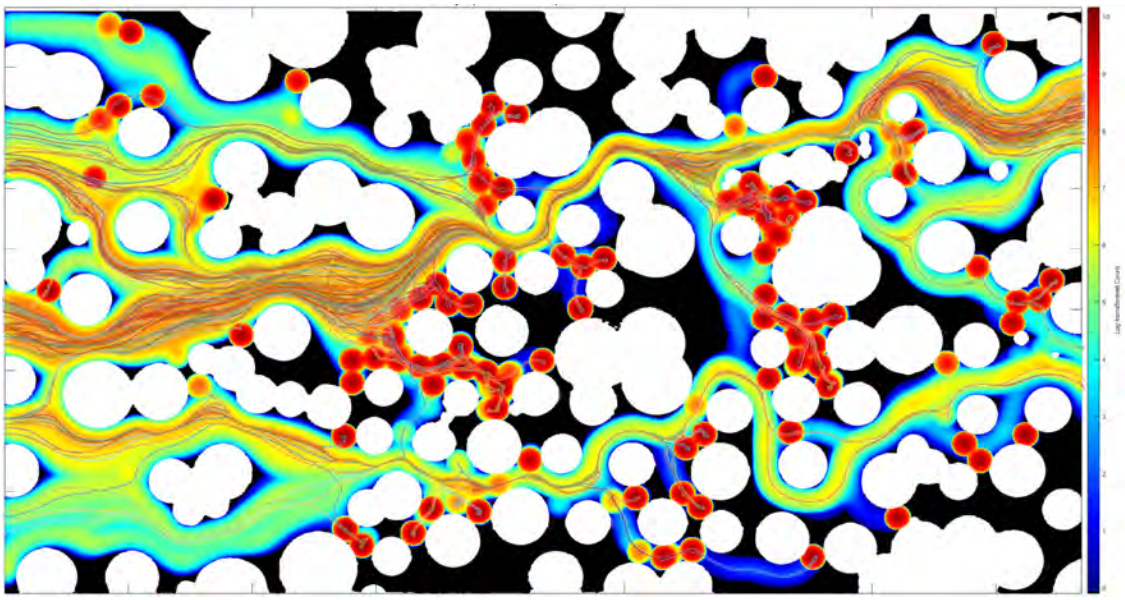

Figure 7.1: Trajectories of Emulsions being transported through a porous medium with Residency Map Overlayed. FOV 13.5 x 7.4 mm

```
% Create a new Map
newMap = containers.Map('KeyType', 'double', 'ValueType', 'any');
newKeyIndex = 1;
% Iterate through the original Map
for k = 1:numKeys
    objectData = Map1(keys{k});
    if length(objectData) >= 350
        newMap(newKeyIndex) = objectData;
        newKeyIndex = newKeyIndex + 1;
    end
end
```

7.3 Label Assignment

Each droplet is assigned a label based on its final position. The labels represent one of the two paths, being stuck, or still traveling. The final x and y coordinates of the droplet determine the label. If the droplet's final x position exceeds 1700, it is classified as following Path 1 or Path 2 based on the y position. If the droplet does not fit these criteria and has more than 8000 data points, it is classified as being stuck. All other droplets are labeled as still traveling through the medium.

```
for i = 1:numKeys
    objectData = Map1(keys{i});
    finalX = objectData(end).position_from_states(1);
    finalY = objectData(end).position_from_states(2);
    label = 0;

    % Check for Path 1 and Path 2 first
    if finalX > 1700
        if finalY >= 540 && finalY <= 670
            label = 1; % Path 1
        elseif finalY >= 90 && finalY <= 240
            label = 2; % Path 2
        end
    end
    % If still unlabeled, check for stuck or still traveling
    if label == 0
        if length(objectData) > 8000
            lastXPositions = arrayfun(@(x) x.position_from_states(1),
                    objectData(end-movingWindow+1:end));
            lastYPositions = arrayfun(@(x) x.position_from_states(2),
                    objectData(end-movingWindow+1:end));
            movingAvgX = movmean(lastXPositions, [10, 0]);
            movingAvgY = movmean(lastYPositions, [10, 0]);

            if (max(movingAvgX) - min(movingAvgX) <= pixelThreshold) &&
                    (max(movingAvgY) - min(movingAvgY) <= pixelThreshold)
                label = 3; % Stuck
            else
                label = 4; % Still traveling
            end
        else
            label = 4; % Still traveling
        end
    end

    labels = [labels; label];
```

7.4 Feature Extraction

For each droplet, a set of features indicative of its behavior is extracted. These features include mean velocities, positional data at specific time steps, and metrics such as tortuosity and velocity direction. Features are selected based on their relevance in emulsion transport and what can be calculated from the positional data from tracking.

```
meanVelocityX = mean(arrayfun(@(x) x.velocity(1),
        objectData(initialTimeSteps:initialTimeSteps)));
meanVelocityY = mean(arrayfun(@(x) x.velocity(2),
        objectData(initialTimeSteps:initialTimeSteps)));
stdVelocity = std(arrayfun(@(x) norm(x.velocity),
        objectData(initialTimeSteps:initialTimeSteps)));

initialPosX = objectData(1).position_from_states(1);
initialPosY = objectData(1).position_from_states(2);
posX_initialTimeStep = objectData(min(initialTimeSteps,
        length(objectData))).position_from_states(1);
posY_initialTimeStep = objectData(min(initialTimeSteps,
        length(objectData))).position_from_states(2);
```

7.5 Initial Time Steps for Prediction

An important aspect of our methodology is the consideration of only the initial time steps of an object's position data for prediction purposes. Specifically, we focus on the first 100 time steps, corresponding to the initial 2 seconds of movement. This approach is crucial as it allows us to capture the early movement characteristics of the droplets, which are often indicative of their overall behavior and final classification.

By using only the initial time steps, we aim to use this data as a predictive event. If we were to use all available data for classification, we would inherently know the droplet's final position or path, thus negating the need for prediction. The ability to accurately classify droplets based on these early time steps demonstrates the usefulness of modeling in this way.

For each droplet, features are extracted from these initial 100 time steps. This includes calculating mean velocities, positional data, and other derived metrics such as tortuosity and velocity direction.

Focusing on this initial segment enables effective differentiation between droplets that follow Path 1, Path 2, become stuck, or continue traveling.

```
% Ensure enough time steps
if length(objectData) < initialTimeSteps
    padSize = initialTimeSteps - length(objectData);
    objectData = [objectData; repmat(objectData(end), padSize, 1)];
end

% Extract the initial frame
initialFrame = objectData(1).frame;
straightLineDist = sqrt((objectData(1).position_from_states(1) -
        objectData(initialTimeSteps).position_from_states(1))^2
        + (objectData(1).position_from_states(2)
        - objectData(initialTimeSteps).position_from_states(2))^2);
accumulatedDist = 0;
for j = 2:initialTimeSteps
    accumulatedDist = accumulatedDist + sqrt((objectData(j).position_from_states(1)
        - objectData(j-1).position_from_states(1))^2
        + (objectData(j).position_from_states(2)
        - objectData(j-1).position_from_states(2))^2);
end
tortuosity = accumulatedDist / straightLineDist;
```

7.6 Random Forest for Classification

Random Forests, a powerful ensemble learning method introduced by Breiman [10], construct multiple decision trees during training and output the mode of the classes for classification or mean prediction for regression tasks. Each tree is trained on a random subset of the data through bootstrapping, with random subsets of features considered for splitting at each node. This randomness helps to ensure that the ensemble of trees has low correlation, leading to improved model generalization. The aggregation of the trees' predictions reduces the variance and prevents overfitting, making Random Forests robust and accurate in various applications.

MATLAB's TreeBagger function closely follows the principles outlined in Breiman's paper, implementing Random Forests by training multiple decision trees on bootstrapped samples of the data and aggregating their predictions. TreeBagger supports both classification and regression, and in-

cludes additional functionalities such as out-of-bag error estimation and quantile regression. These features provide enhanced flexibility and robustness, ensuring reliable model performance across various datasets.

7.7 Training and Testing the Model

The extracted features are utilized to train a Random Forest model. The data is split into training and testing sets, with 40% reserved for testing. The model is trained using the training set, and its performance is evaluated on the testing set. Accuracy and confusion matrices are calculated to assess the model's predictive power.

```
cv = cvpartition(size(enhancedFeatures, 1), 'HoldOut', 0.4);
idx = cv.test;
XTrain = enhancedFeatures(~idx,:);
YTrain = labels(~idx);
XTest = enhancedFeatures(idx,:);
YTest = labels(idx);

% Creating the Random Forest model
RFModel = TreeBagger(numTrees, XTrain, YTrain, 'Method',
        'classification', 'OOBPrediction', 'On', 'MinLeafSize', 1);

% Predicting using the Random Forest model
[YPred, ~] = predict(RFModel, XTest);
YPred = str2double(YPred);

% Calculate Accuracy and Confusion Matrix
acc = sum(YTest == YPred) / length(YTest);
C = confusionmat(YTest, YPred);
```

7.8 Evaluating Feature Combinations

The model's performance is refined by evaluating different combinations of features. The best combination is selected based on the highest true positive rate for a particular label, in this case, label 3 (stuck). This is due to the fact that label 3 has the least amount of data points.

```
% Iterate through the confusion matrices
for i = 1:size(avgConfMatrices, 3)
    truePositivesLabel3 = avgConfMatrices(3, 3, i);
    if truePositivesLabel3 > maxTruePositives
        maxTruePositives = truePositivesLabel3;
        bestComboIndex = i;
    end
end
```

7.9 Results and Discussion

The best feature combination for predicting droplets that are stuck includes ‘meanVelocityX‘, ‘posXinitialTimeStep‘, ‘posYinitialTimeStep‘, and ‘initialFrame‘. The results indicate that even with just 100 positional updates, our model can predict droplet tracks with an accuracy of up to 92%. This demonstrates the effectiveness of our feature extraction and machine learning approach in making early and accurate predictions about droplet behavior. By leveraging the initial time steps, we ensure that our model is trained to make predictions based on early motion data, significantly enhancing its accuracy and reliability in classifying droplet tracks.

The average, minimum, and maximum values for each feature across different combinations are summarized in Table 7.1. These values represent the number of emulsions predicted to become trapped, which constituted our smallest data class. It is evident that the initial frame plays a critical role in predicting whether an emulsion will get trapped in the media. This indicates that emulsions present early in the process are more likely to be transported to smaller pores with high local velocities, where they quickly become trapped and pinned.

The application of machine learning, specifically Random Forest models, in predicting droplet tracks in emulsions is highly effective. By carefully selecting and evaluating feature combinations, we achieve high accuracy in classifying droplets’ paths, their likelihood of being stuck, or continuing to travel.

7.10 Conclusion and Future Work

This study represents a minimal yet promising application of machine learning in predicting droplet tracks in emulsions. Despite its simplicity, the approach demonstrates that even with limited data,

Table 7.1: Feature Summary Statistics

Feature	AverageValue	MinValue	MaxValue
meanVelocityX	4.84	0	14
posX$_i$*initialTimeStep*	5.09	0	14
posY$_i$*initialTimeStep*	4.83	0	14
initialPosY	4.85	0	13
initialFrame	10.8	8	14
tortuosity	4.89	0	12.6
avgVelocityDirection	4.85	0	13
meanVelocityY	4.83	0	13

machine learning techniques can achieve significant predictive accuracy. By leveraging the initial 100 time steps of droplet movement, our model successfully classified the droplet tracks with up to 92% accuracy. This indicates a strong potential for machine learning in this field.

However, it is important to acknowledge that this work is based on a single experiment and one specific porous media design. As more experiments are conducted and larger databases of emulsion transport in porous media become available, there will be an opportunity to apply more advanced machine learning techniques. These advanced methods can address the complex problem of emulsions in porous media more comprehensively.

Future research can benefit greatly from these expanded datasets. With more extensive data, it will be possible to uncover foundational characteristics and underlying patterns in emulsion dynamics. Advanced machine learning algorithms, such as deep learning and ensemble methods, could then be employed to enhance the predictive models further.

In conclusion, while this study serves as a preliminary investigation, it highlights the promise of machine learning in this domain. The continued development of experimental databases and the application of sophisticated machine learning techniques will likely lead to significant advancements in understanding and predicting the behavior of emulsions in porous media.

Chapter 8

Final Conclusion

8.1 Summary of Findings

This dissertation presents significant advancements in understanding the pore-level dynamics of emulsions in porous media. We report the first multi-scale measurements of the dynamics of individual droplets, droplet-droplet interactions, porous medium dynamic changes, and the bulk level transport properties of the medium. The results of our research presents the formation of preferential flow paths due to permeability reduction which entails a decrease in medium permeability from a bulk measurement perspective. The known anomalous transport and enhanced shear thickening of emulsion reported in industrial processes can be truly explained by our pore-level measurements, resolving a long-standing paradox in flow of emulsions in porous media.

By integrating cutting-edge microfluidic techniques, high-resolution 3D printing, and advanced image processing methods, we have developed a robust framework for studying and characterizing emulsion behavior in complex environments. Our innovative approach allowed precise control over emulsion size, concentration, and injection rates, leading to detailed insights into the transport mechanisms and interactions within porous structures.

Specifically, we found that by using high-resolution 3D printing to fabricate microfluidic devices, we could consistently generate uniform droplets, crucial for studying the intricate dynamics of multiphase flows. The control over emulsion size and concentration was achieved through precise manipulation of flow rates and device geometries, allowing us to systematically investigate how these factors influence emulsion transport.

8.2 Broader Implications and Impact

The insights gained from this research have far-reaching implications across multiple disciplines, including environmental science, biomedical engineering, and industrial processes. The ability to manipulate and analyze emulsions at such a granular level opens up new avenues for practical applications such as soil remediation, targeted drug delivery, and enhanced oil recovery. The methods developed here provide a foundation for optimizing fluid dynamics in various porous media, potentially leading to more efficient and sustainable practices in these fields.

8.2.1 Advancements in Microfluidic Technology

This research introduces a state-of-the-art integrated microfluidic and imaging system that facilitates real-time analysis and high-precision control of emulsion formation and transport. Using high-resolution 3D printing, we fabricated microfluidic devices with precise geometries, allowing us to consistently generate uniform droplets and systematically vary parameters such as porosity, length, and width of the devices. These advancements set a new standard for precision and reproducibility in experimental setups.

8.2.2 Enhanced Understanding of Emulsion Dynamics

Our study revealed the critical role of droplet size and distribution in defining preferential transport paths within porous media. For example, we discovered that lower concentrations of emulsions flow through pores with higher local velocities, leading to a 35% reduction in the porosity of the medium due to trapping in smaller pores. This leads to the formation of preferential and highly tortuous flow paths.

Furthermore, the discovery of the velocity-age power-law relationship, which is independent of droplet size, suggests a potentially universal characteristic of porous media dynamics. This relationship indicates that the average velocity of the emulsions scales inversely with their residence time within the porous structure, providing a fundamental insight into emulsion transport in complex environments.

Additionally, the variational mode decomposition (VMD) method proved effective in analyzing the velocity signals within the microfluidic channels. IMF 5, an intrinsic mode function obtained through VMD, was particularly robust in separating physical flow components from oscillatory and

noisy parts, predicting droplet sizes and formations accurately.

8.2.3 Opportunities for Machine Learning in Emulsion Dynamics

The methodologies developed in this dissertation lay a solid foundation for future experiments and the creation of extensive databases on emulsion transport in porous media. These datasets will be invaluable for leveraging machine learning techniques to further understand the complex nature of emulsion transport, which is challenging to simulate accurately due to the intricate physics involved.

By conducting experiments and generating comprehensive datasets, future research can employ advanced machine learning algorithms to identify patterns and predict emulsion behavior under various conditions. This approach opens up new avenues for exploration, enabling the development of predictive models that can handle the intricate dynamics of multiphase flows in porous structures. This includes accounting for lubrication between particles, particle-particle interactions, fluid dynamics, and correlations between the flow in different pores due to complex physical interactions.

Machine learning can thus help unravel the complexities of deformable particles moving through filters, which has significant implications for fields such as targeted medicine delivery in porous tissues and other natural porous media that are difficult to experiment on and too complex for traditional simulations.

The preliminary success in using machine learning to classify droplet tracks with up to 92% accuracy demonstrates the potential of these techniques. As more data becomes available, the application of deep learning and other sophisticated algorithms could significantly enhance our understanding and control of emulsion transport processes. These advancements could lead to improved strategies for managing and optimizing the flow of emulsions in various industrial and biomedical applications.

The ability to simulate and predict the behavior of emulsions in complex porous media using machine learning not only enhances our fundamental understanding but also offers practical solutions for real-world challenges. This interdisciplinary approach can bridge the gap between experimental observations and theoretical models, providing a comprehensive toolset for future research and applications in the field of emulsion dynamics.

8.3 Conclusion

This dissertation has systematically examined the transport properties of emulsions in diverse porous media, elucidating how the structural characteristics of the porous networks and the properties of the emulsions influence their movement. The integration of precise fabrication techniques, advanced imaging, and sophisticated data analysis tools provides a comprehensive approach to studying complex fluid systems.

The non-linear nature of emulsion transport was investigated through variational mode decomposition (VMD), revealing that certain intrinsic modes carry significant physical information about the flow dynamics. Specifically, IMF 5 was found to have distinct spikes when the flow is initiated and transitions into a plateau as uniform droplets form, indicating its robustness in predicting droplet sizes and formations.

Our experimental findings demonstrated that natural porous media, with closer packing and inherent structural complexity, facilitate more stable and predictable emulsion movement, reducing instances of ballistic transport. In contrast, artificial porous media, engineered with varying porosity and structure, allow for more diverse transport regimes, including enhanced ballistic transport due to less constrained pore pathways.

Furthermore, the development of a robust experimental framework and the creation of high-quality datasets pave the way for future applications of machine learning in this field. The initial success in predicting droplet tracks highlights the potential of machine learning to provide deeper insights and improve control over emulsion transport processes. As larger databases are built and more sophisticated algorithms are applied, significant advancements in understanding and predicting the behavior of emulsions in porous media are expected.

By conducting experiments and generating comprehensive datasets, future research can employ advanced machine learning algorithms to identify patterns and predict emulsion behavior under various conditions. This approach opens up new avenues for exploration, enabling the development of predictive models that can handle the intricate dynamics of multiphase flows in porous structures. This includes accounting for lubrication between particles, particle-particle interactions, fluid dynamics, and correlations between the flow in different pores due to complex physical interactions.

In summary, this research advances our understanding of emulsion dynamics in porous media and sets the stage for future innovations in microfluidic technology and fluid dynamics research. The findings demonstrate the importance of considering structural characteristics and emulsion

properties in designing and optimizing processes that rely on emulsion transport, such as enhanced oil recovery, soil remediation, and drug delivery systems.

By addressing fundamental challenges and providing robust solutions, this dissertation propels the field forward, offering new tools and insights that will benefit future studies and industrial applications alike. The potential for cross-disciplinary impact underscores the importance of continued exploration and innovation in this vital area of study.

Bibliography

[1] Karen Alim, Shima Parsa, David A. Weitz, and Michael P. Brenner. Local pore size correlations determine flow distributions in porous media. *Phys. Rev. Lett.*, 119:144501, Oct 2017.

[2] Phillip J. Ansell and Maciej J. Balajewicz. Separation of unsteady scales in a mixing layer using empirical mode decomposition. *AIAA Journal*, 55, 2017.

[3] R. T. Armstrong, A. Georgiadis, H. Ott, D. Klemin, and S. Berg. Critical capillary number: Desaturation studied with fast x-ray computed microtomography. *Geophysical Research Letters*, 41:55–60, 2014.

[4] Solomon Barkley, Samantha J. Scarfe, Eric R. Weeks, and Kari Dalnoki-Veress. Predicting the size of droplets produced through laplace pressure induced snap-off. *Soft Matter*, 12:7398–7404, 2016.

[5] Solomon Barkley, Eric R. Weeks, and Kari Dalnoki-Veress. Snap-off production of monodisperse droplets. *Eur. Phys. J. E*, 38:138, 2015.

[6] W.-B. Bartels, H. Mahani, S. Berg, and S.M. Hassanizadeh. Literature review of low salinity waterflooding from a length and time scale perspective. *Fuel*, 236:338–353, 2019.

[7] Sarah Battat, David A. Weitz, and George M Whitesides. An outlook on microfluidics: the promise and the challenge. *Lab Chip*, 22:530–536, 2022.

[8] Jacob Bear. *Dynamics of Fluids in Porous Media*. Courier Corporation, 1975.

[9] Heather A.E. Benson and Adam C. Watkinson. *Transdermal and Topical Drug Delivery: Principles and Practice*. 2012.

[10] Leo Breiman. Random forests. *Machine Learning*, 45(1):5–32, 2001.

[11] F. P. Bretherton. The motion of long bubbles in tubes. *Journal of Fluid Mechanics*, 10(2):166–188, 1961.

[12] Ouriel Caen, Simon Schütz, M. S.Suryateja Jammalamadaka, Jérémy Vrignon, Philippe Nizard, Tobias M. Schneider, Jean Christophe Baret, and Valérie Taly. High-throughput multiplexed fluorescence-activated droplet sorting. *Microsystems and Nanoengineering*, 4, 2018.

[13] Nick J. Carroll, Kaare H. Jensen, Shima Parsa, N. Michele Holbrook, and David A. Weitz. Measurement of flow velocity and inference of liquid viscosity in a microfluidic channel by fluorescence photobleaching. *Langmuir*, 30, 2014.

[14] R. D.M. Carvalho, O. J. Venturini, E. I. Tanahashi, F. Neves, and F. A. França. Application of the ultrasonic technique and high-speed filming for the study of the structure of air–water bubbly flows. *Experimental Thermal and Fluid Science*, 33(7):1065–1086, 2009.

[15] Connie B. Chang, James N. Wilking, Shin Hyun Kim, Ho Cheung Shum, and David A. Weitz. Monodisperse emulsion drop microenvironments for bacterial biofilm growth. *Small*, 11, 2015.

[16] L. Chen, C. Yang, Y. Xiao, X. Yan, L. Hu, M. Eggersdorfer, D. Chen, D. A. Weitz, and F. Ye. Millifluidics, microfluidics, and nanofluidics: manipulating fluids at varying length scales. *Materials Today Nano*, 16, 2021.

[17] Krzysztof Churski, Jacek Michalski, and Piotr Garstecki. Droplet on demand system utilizing a computer controlled microvalve integrated into a stiff polymeric microfluidic device. *Lab Chip*, 10:512–518, 2010.

[18] S. Cobos, M. S. Carvalho, and V. Alvarado. Flow of oil–water emulsions through a constricted capillary. *International Journal of Multiphase Flow*, 35(6):507–515, 2009.

[19] R. Dangla, S.C. Kayi, and C.N. Baroud. Droplet microfluidics driven by gradients of confinement. *Proceedings of the National Academy of Sciences of the United States of America*, 110(3):853–858, 2013.

[20] Rémi Dangla, Etienne Fradet, Yonatan Lopez, and Charles N Baroud. The physical mechanisms of step emulsification. *Journal of Physics D: Applied Physics*, 46(11):114003, 2013.

[21] Sujit S. Datta, Ilenia Battiato, Martin A. Fernø, Ruben Juanes, Shima Parsa, Valentina Prigiobbe, Enric Santanach-Carreras, Wen Song, Sibani Lisa Biswal, and David Sinton. Lab on a chip for a low-carbon future. *Lab Chip*, 23:1358–1375, 2023.

[22] Boris Delaunay. Sur la sphère vide. *Bulletin de l'Académie des Sciences de l'URSS, Classe des Sciences Mathématiques et Naturelles*, 6:793–800, 1934.

[23] Cyrille L. Delley and Adam R. Abate. Microfluidic particle zipper enables controlled loading of droplets with distinct particle types. *Lab on a Chip*, 20, 2020.

[24] Xu Diao, Juncheng Jiang, Guodong Shen, Zhaozhao Chi, Zhirong Wang, Lei Ni, Ahmed Mebarki, Haitao Bian, and Yongmei Hao. An improved variational mode decomposition method based on particle swarm optimization for leak detection of liquid pipelines. *Mechanical Systems and Signal Processing*, 143, 2020.

[25] Konstantin Dragomiretskiy and Dominique Zosso. Variational mode decomposition. *IEEE Transactions on Signal Processing*, 62:531–544, 02 2014.

[26] Michael Eckert. *The Dawn of Fluid Dynamics:A Discipline between Science and Technology.* Wiley-VCH, 2007.

[27] F. Foucher and P. Ravier. Determination of turbulence properties by using empirical mode decomposition on periodic and random perturbed flows. *Experiments in Fluids*, 49, 2010.

[28] Rc Gonzalez and Re Woods. *Digital Image Processing.* Prentice Hall, 2002.

[29] Victor Raul Guillen, Mao Illich Romero, Marcio da Silveira Carvalho, and Vladimir Alvarado. Capillary-driven mobility control in macro emulsion flow in porous media. *International Journal of Multiphase Flow*, 43:62–65, 2012.

[30] Medina Hamidović, Uli Marta, Helen Bridle, Damir Hamidović, Gerold Fink, Robert Wille, Andreas Springer, and Werner Haselmayr. Off-chip-controlled droplet-on-demand method for precise sample handling. *ACS Omega*, 5(17):9684–9689, 2020. PMID: 32391454.

[31] Marie Hébert, Jan Huissoon, and Carolyn L Ren. A perspective of active microfluidic platforms as an enabling tool for applications in other fields. *Journal of Micromechanics and Microengineering*, 32(4):043001, mar 2022.

[32] R. Hilfer and P. E. Øren. Dimensional analysis of pore scale and field scale immiscible displacement. *Transport in Porous Media*, 22:53–72, 1996.

[33] Norden E Huang, Zheng Shen, Steven R Long, Manli C Wu, Hsing H Shih, Nai chyuan Yen, Chi Chao Tung, and Henry H Liu. The empirical mode decomposition and the hilbert spectrum for nonlinear and non-stationary time series analysis. *Proceedings of the Royal Society A*, 454, 1996.

[34] Norden E. Huang and Zhaohua Wu. A review on hilbert-huang transform: Method and its applications to geophysical studies. *Reviews of Geophysics*, 46, 2008.

[35] Michael Izaguirre, Luke Nearhood, and Shima Parsa. Quantifying uniform droplet formation in microfluidics using variational mode decomposition. *Fluids*, 7(5):174, May 2022.

[36] Michael Izaguirre and Shima Parsa. Emergence of preferential flow paths and intermittent dynamics in emulsion transport in porous media. *Soft Matter*, 20:3585–3592, 2024.

[37] Ya juan Xue, Jun xing Cao, Xing jian Wang, and Hao kun Du. Reservoir permeability estimation from seismic amplitudes using variational mode decomposition. *Journal of Petroleum Science and Engineering*, 208, 2022.

[38] Imre M. Jánosi and Rolf Müller. Empirical mode decomposition and correlation properties of long daily ozone records. *Physical Review E - Statistical, Nonlinear, and Soft Matter Physics*, 71, 2005.

[39] Dorothee L. Kurz, Eleonora Secchi, Roman Stocker, and Joaquin Jimenez-Martinez. Morphogenesis of biofilms in porous media and control on hydrodynamics. *Environmental Science & Technology*, 57(14):5666–5677, 2023. PMID: 36976631.

[40] M. Le Blay, M. Adda-Bedia, and D. Bartolo. Emergence of scale-free smectic rivers and critical depinning in emulsions driven through disorder. *Proc Natl Acad Sci U S A*, 117(25):13914–13920, June 2020.

[41] D.T. Lee and B.J. Schachter. Two algorithms for constructing a delaunay triangulation. *International Journal of Computer and Information Sciences*, 9:219–242, 1980.

[42] Ta-Chih Lee, Rangasami L. Kashyap, and Chong-Nam Chu. Building skeleton models via 3-d medial surface/axis thinning algorithms. *Computer Vision, Graphics, and Image Processing*, 56(6):462–478, 1994.

[43] Young S. Lee, Stylianos Tsakirtzis, Alexander F. Vakakis, Lawrence A. Bergman, and D. Michael McFarland. Physics-based foundation for empirical mode decomposition. *AIAA Journal*, 47, 2009.

[44] W. Lei, C. Xie, T. Wu, et al. Transport mechanism of deformable micro-gel particle through micropores with mechanical properties characterized by afm. *Sci Rep*, 9:1453, 2019.

[45] Ying Li and Alireza Abbaspourrad. Phycocyanin-rich water-in-oil-in-water (w1/o/w2) double emulsion with nanosized particles: Improved color stability against light exposure. *Colloids and Surfaces B: Biointerfaces*, 220:112930, 2022.

[46] Victor A. Lifton. Microfluidics: an enabling screening technology for enhanced oil recovery (eor). *Lab Chip*, 16:1777–1796, 2016.

[47] D. R. Link, S. L. Anna, D. A. Weitz, and H. A. Stone. Geometrically mediated breakup of drops in microfluidic devices. *Physical Review Letters*, 92, 2004.

[48] Wei Liu, Siyuan Cao, Zhaoyu Jin, Zhiming Wang, and Yangkang Chen. A novel hydrocarbon detection approach via high-resolution frequency-dependent avo inversion based on variational mode decomposition. *IEEE Transactions on Geoscience and Remote Sensing*, 56, 2017.

[49] Haiwei Lu, Kirk Mutafopulos, John A. Heyman, Pascal Spink, Liang Shen, Chaohui Wang, Thomas Franke, and David A. Weitz. Rapid additive-free bacteria lysis using traveling surface acoustic waves in microfluidic channels. *Lab on a Chip*, 19, 2019.

[50] A. Mandal and A. Bera. Modeling of flow of oil-in-water emulsions through porous media. *Pet. Sci.*, 12:273–281, 2015.

[51] T. G. Mason, J. Bibette, and D. A. Weitz. Yielding and flow of monodisperse emulsions. *Journal of Colloid and Interface Science*, 179(2):439–448, 1996.

[52] Linas Mazutis, John Gilbert, W. Lloyd Ung, David A. Weitz, Andrew D. Griffiths, and John A. Heyman. Single-cell analysis and sorting using droplet-based microfluidics. *Nature Protocols*, 8, 2013.

[53] Jenna A Moore-Ott, Selena Chiu, Daniel B Amchin, Tapomoy Bhattacharjee, and Sujit S Datta. A biophysical threshold for biofilm formation. 11:e76380, jun 2022.

[54] K. Mutafopulos, P. Spink, C. D. Lofstrom, P. J. Lu, H. Lu, J. C. Sharpe, T. Franke, and D. A. Weitz. Traveling surface acoustic wave (tsaw) microfluidic fluorescence activated cell sorter (μfacs). *Lab on a Chip*, 19, 2019.

[55] Saraf Nawar, Joshuah K. Stolaroff, Congwang Ye, Huayin Wu, Du Thai Nguyen, Feng Xin, and David A. Weitz. Parallelizable microfluidic dropmakers with multilayer geometry for the generation of double emulsions. *Lab Chip*, 20:147–154, 2020.

[56] Tannaz Pak, Ian B. Butler, Sebastian Geiger, Marinus I. J. van Dijke, and Ken S. Sorbie. Droplet fragmentation: 3d imaging of a previously unidentified pore-scale process during multiphase flow in porous media. *Proceedings of the National Academy of Sciences*, 112(7):1947–1952, 2015.

[57] Shima Parsa, Jeffrey S. Guasto, Monica Kishore, Nicholas T. Ouellette, J. P. Gollub, and Greg A. Voth. Rotation and alignment of rods in two-dimensional chaotic flow. *Physics of Fluids*, 23(4):043302, 04 2011.

[58] Shima Parsa, Enric Santanach-Carreras, Lizhi Xiao, and David A. Weitz. Origin of anomalous polymer-induced fluid displacement in porous media. *Phys. Rev. Fluids*, 5:022001, Feb 2020.

[59] Shima Parsa, Ahmad Zareei, Enric Santanach-Carreras, Eliza J. Morris, Ariel Amir, Lizhi Xiao, and David A. Weitz. Unexpected scaling of interstitial velocities with permeability due to polymer retention in porous media. *Phys. Rev. Fluids*, 6:L082302, Aug 2021.

[60] Antonio Perazzo, Giovanna Tomaiuolo, Valentina Preziosi, and Stefano Guido. Emulsions in porous media: From single droplet behavior to applications for oil recovery. *Advances in Colloid and Interface Science*, 256:305–325, 2018.

[61] Ingmar Polenz, David A. Weitz, and Jean Christophe Baret. Polyurea microcapsules in microfluidics: Surfactant control of soft membranes. *Langmuir*, 31, 2015.

[62] H. Péter, A. Libál, C. Reichhardt, and C. J.O. Reichhardt. Crossover from jamming to clogging behaviours in heterogeneous environments. *Scientific Reports*, 8:10252, 2018.

[63] Catherine Rivet, Hyewon Lee, Alison Hirsch, Sharon Hamilton, and Hang Lu. Microfluidics for medical diagnostics and biosensors. *Chemical Engineering Science*, 66, 2011.

[64] J.G. Roof. Snap-off of oil droplets in water-wet pores. *Society of Petroleum Engineers Journal*, 10(01):85–90, 03 1970.

[65] Assaf Rotem, Oren Ram, Noam Shoresh, Ralph A. Sperling, Michael Schnall-Levin, Huidan Zhang, Anindita Basu, Bradley E. Bernstein, and David A. Weitz. High-throughput single-cell labeling (hi-scl) for rna-seq using drop-based microfluidics. *PLOS ONE*, 10:1–14, 05 2015.

[66] Mehdi Sadeghi, Fabrice Foucher, Karim Abed-Meraim, and Christine Mounaïm-Rousselle. Bivariate 2d empirical mode decomposition for analyzing instantaneous turbulent velocity field in unsteady flows. *Experiments in Fluids*, 60, 2019.

[67] V.C. Santannaa, F.D.S Curbelob, T.N. Castro Dantasc, A.A. Dantas Netoc, H.A. Albuquerque, and A.I.C Garnicab. Microemulsion flooding for enhanced oil recovery. *Journal of Petroleum Science and Engineering*, 66(3):117–120, 2009.

[68] Peter J. Schmid. Dynamic mode decomposition of numerical and experimental data. *JOURNAL OF FLUID MECHANICS*, 656:5–28, AUG 10 2010.

[69] Youngmin Seo, Sungwon Kim, and Vijay P. Singh. Machine learning models coupled with variational mode decomposition: A new approach for modeling daily rainfall-runoff. *Atmosphere*, 9, 2018.

[70] Joseph D. Seymour and Paul T. Callaghan. Generalized approach to nmr analysis of flow and dispersion in porous media. *AIChE Journal*, 43, 1997.

[71] Luoran Shang, Yao Cheng, and Yuanjin Zhao. Emerging droplet microfluidics. *Chemical Reviews*, 117(12):7964–8040, 2017.

[72] Hamed Shieh, Maryam Saadatmand, Mahnaz Eskandari, and Dariush Bastani. Microfluidic on-chip production of microgels using combined geometries. *Scientific Reports*, 11, 2021.

[73] Angela Stallone, Antonio Cicone, and Massimo Materassi. New insights and best practices for the successful use of empirical mode decomposition, iterative filtering and derived algorithms. *Scientific Reports*, 10, 2020.

[74] H. A Stone. Dynamics of drop deformation and breakup in viscous fluids. *Annual Review of Fluid Mechanics*, 26(1):65–102, 1994.

[75] H.A. Stone, A.D. Stroock, and A. Ajdari. Engineering flows in small devices: Microfluidics toward a lab-on-a-chip. *Annual Review of Fluid Mechanics*, 36(1):381–411, 2004.

[76] H. Takao and M. Ishida. Microfluidic integrated circuits for signal processing using analogous relationship between pneumatic microvalve and mosfet. *Journal of Microelectromechanical Systems*, 12(4):497–505, 2003.

[77] A.Y. Tenorio-Barajas, M. de la Luz Olvera-Amador, V. Altuzar, R. Ruiz-Ramos, M.A. Palomino-Ovando, and C. Mendoza-Barrera. Microdroplet formation in microfluidic channels by multiphase flow simulation. *Conference Proceedings IEEE: 2019 16th International Conference on Electrical Engineering, Computing Science and Automatic Control (CCE)*, 2019.

[78] Adrian J. T. Teo, King-Ho Holden Li, Nam-Trung Nguyen, Wei Guo, Nadine Heere, Heng-Dong Xi, Chia-Wen Tsao, Weihua Li, and Say Hwa Tan. Negative pressure induced droplet generation in a microfluidic flow-focusing device. *Analytical Chemistry*, 89(8):4387–4391, 2017. PMID: 28192966.

[79] William Thielicke and René Sonntag. Particle image velocimetry for matlab: Accuracy and enhanced algorithms in pivlab. *Journal of Open Research Software*, 9, 2021.

[80] Andrew S. Utada, Alberto Fernandez-Nieves, Howard A. Stone, and David A. Weitz. Dripping to jetting transitions in coflowing liquid streams. *Phys. Rev. Lett.*, 99:094502, Aug 2007.

[81] Koen van Dijke, Riëlle de Ruiter, Karin Schroën, and Remko Boom. The mechanism of droplet formation in microfluidic edge systems. *Soft Matter*, 6:321–330, 2010.

[82] Nicolas Waisbord, Norbert Stoop, Derek M. Walkama, Jörn Dunkel, and Jeffrey S. Guasto. Anomalous percolation flow transition of yield stress fluids in porous media. *Phys. Rev. Fluids*, 4:063303, Jun 2019.

[83] G. Whitesides. The origins and the future of microfluidics. *Nature*, 442:368–373, 2006.

[84] Hau Tieng Wu, Han Kuei Wu, Chun Li Wang, Yueh Lung Yang, Wen Hsiang Wu, Tung Hu Tsai, and Hen Hong Chang. Modeling the pulse signal by wave-shape function and analyzing by synchrosqueezing transform. *PLoS ONE*, 11, 2016.

[85] Zhaohua Wu and Norden E. Huang. Ensemble empirical mode decomposition: A noise-assisted data analysis method. *Advances in Adaptive Data Analysis*, 1, 2009.

[86] Dan Xiao and Bruce J. Balcom. echo-planar imaging with concomitant field compensation for porous media mri. *Journal of Magnetic Resonance*, 260, 2015.

[87] Long Yu, Boxin Ding, Mingzhe Dong, and Qi Jiang. Plugging ability of oil-in-water emulsions in porous media: Experimental and modeling study. *Industrial & Engineering Chemistry Research*, 57(43):14795–14808, 2018.

[88] Ahmad Zareei, Deng Pan, and Ariel Amir. Temporal evolution of erosion in pore networks: From homogenization to instability. *Physical Review Letters*, 128:234501, 2022.

[89] A. Zeiler, R. Faltermeier, I. R. Keck, A. M. Tomé, C. G. Puntonet, and E. W. Lang. Empirical mode decomposition - an introduction. In *Proceedings of the International Joint Conference on Neural Networks*, 2010.

[90] Wen Zeng, Ian Jacobi, Songjing Li, and Howard A Stone. Variation in polydispersity in pump- and pressure-driven micro-droplet generators. *J. Micromech. Microeng.*, 25(11):115015, oct 2015.

[91] Liyuan Zhang, Alireza Abbaspourrad, Shima Parsa, Jizhou Tang, Flavia Cassiola, Meng Zhang, Shouceng Tian, Caili Dai, Lizhi Xiao, and David A. Weitz. Core–shell nanohydrogels with programmable swelling for conformance control in porous media. *ACS Applied Materials & Interfaces*, 12(30):34217–34225, 2020. PMID: 32633933.

[92] Alexander Z. Zinchenko and Robert H. Davis. Emulsion flow through a packed bed with multiple drop breakup. *Journal of Fluid Mechanics*, 725:611–663, 2013.